BULK PROPERTIES AND ATMOSPHERIC STRUCTURE OF PLUTO AND CHARON

by

Leslie Ann Young

A. B., Physics, Harvard College (1987)

Submitted in Partial Fulfillment of the Requirements for the Degree of

DOCTOR OF PHILOSOPHY

in

EARTH, ATMOSPHERIC, AND PLANETARY SCIENCES

at the

MASSACHUSETTS INSTITUTE OF TECHNOLOGY

June 1994

Signature of Author .....
Department of Earth, Atmospheric, and Planetary Sciences
June 21, 1994

Certified by .....
Professor James L. Elliot
Thesis Supervisor
Department of Earth, Atmospheric, and Planetary Sciences

Accepted by .....
Professor Thomas Jordan
Chairman, Department Graduate Committee

ABSTRACT

We present three observational programs to investigate Pluto's atmospheric structure and the bulk properties of Pluto and Charon: (i) astrometry of the motions of Pluto and Charon around the system barycenter to determine their individual masses; (ii) analysis of a stellar occultation to find temperatures and pressures in Pluto's middle atmosphere; and (iii) spectroscopy of gaseous CH_4 to find its abundance in Pluto's atmosphere. The astrometric observations, taken from 1992 Feb. 26 to 1992 Mar. 2 at the University of Hawaii 2.2-m telescope on Mauna Kea, indicate Pluto and Charon masses of $(12.38 \pm 0.12) \times 10^{24}$ g and $(1.94 \pm 0.04) \times 10^{24}$ g respectively. We develop an analytic light curve model for a stellar-occultation by a small, spherically symmetric planetary atmosphere that includes thermal gradients and an extinction layer. We fit this model to the Kuiper Airborne Observatory data from the 1988 stellar occultation by Pluto. The light curve indicates a transition in the structure of Pluto's atmosphere at 1215 ± 11 km from Pluto's center. For a predominately N_2 atmosphere, the temperature above this transition radius is 99.2 ± 0.07 K, with a gradient of -0.049 ± 0.066 K km^{-1} and a pressure at the transition radius of 2.268 ± 0.217 μbar. Below this transition radius, the atmosphere has either a haze (optical depth ≥ 0.145) or a steep thermal gradient (≥20 K km^{-1}). High-resolution spectra (R = 13,300) of Pluto from 1661.8 to 1667.0 nm were obtained at NASA's Infrared Telescope Facility on Mauna Kea in May 1992. The spectral range included the R(0) and Q lines of the $2\nu_3$ band of CH_4, and indicate a CH_4 column height of $1.20^{+3.15}_{-0.87}$ cm-A.

Thesis supervisor: Dr. James L. Elliot

Title: Professor of Astronomy and Physics

ACKNOWLEDGMENTS

While I owe thanks to my professors, fellow graduate students, and others for their contributions, discussions, answers, and friendship, this thesis would never have even been started if it hadn't been for the following:

My brother, Eliot Young, for introducing me to the planetary science group at MIT, and for his eagerness to talk about Pluto, anytime, anywhere;

My advisor, Jim Elliot, for taking me along the path from programmer to scientist, with finesse and humor;

My husband, Paul Starkis, for his love and patience, and for always showing interest;

And P8, for being in the right place at the right time.

TABLE OF CONTENTS

LIST OF FIGURES

LIST OF TABLES

CHAPTER 1
INTRODUCTION

It is difficult to study the atmosphere of Pluto without considering the surface and interior as well. For example, the surface is expected to be in vapor-pressure equilibrium with the atmosphere, so the atmospheric composition is mainly determined by the state and composition of the surface. Also, the atmospheric composition may reflect that of Pluto's volatile reservoir, since the interior has to replenish Pluto's escaping atmosphere (Trafton 1990). We present three observational programs to investigate Pluto's atmospheric structure and the bulk properties of Pluto and Charon: (i) astrometry of Pluto and Charon to determine their individual masses; (ii) analysis of a stellar occultation (Pluto passing in front of a star) to find temperatures and pressures in Pluto's middle atmosphere; and (iii) spectroscopy of gaseous CH_4 to find its abundance in Pluto's atmosphere.

In Chapter 2, the orbits of Pluto and Charon around the system barycenter are measured. Since the period is known, this gives the masses of each body. It also gives the semimajor axis of Charon's orbit around Pluto, which sets the linear scale for the radii derived from the mutual events (Buie *et al.* 1992; E. Young* and Binzel 1994). The densities are currently uncertain, since a large range of radii has been reported for each body (Buie *et al.* 1992; Elliot and Young 1991; Elliot and Young 1992; Hubbard *et al.* 1990; E. Young and Binzel 1994). For example, different model assumptions for the structure of Pluto's lower atmosphere change the radius derived from the stellar occultation by more than 20 km (Chapter 3).

---

* Papers by the author are cited as "Young," while those by her brother are cited as "E. Young."

In Chapter 3, we analyze the 1988 stellar occultation by Pluto to find the temperature, pressure, and optical depth as functions of radius. One goal of this work is to detect or place limits on a mild thermal gradient in Pluto's middle atmosphere. Since Pluto is small, many of the approximations commonly used for analyzing stellar occultations are of the same order as the effects of a mild thermal gradient. We first develop equations for analyzing occultations by small planets, and then apply them to the Pluto occultation. Chapter 3 is largely based on Elliot and Young (1992). At the time of that work, there were three major unknowns: the primary constituent of the atmosphere; an accurate value for Pluto's mass; and the structure of the lower atmosphere. Two of these are now known. The major constituent has been determined to be N_2, from reflectance spectra of Pluto's surface (Owen *et al.* 1993). The improved value for Pluto's mass is provided by the measurements of Chapter 2. The structure of the lower atmosphere has not however been resolved. On the contrary, a recently proposed troposphere (Stansberry *et al.* 1994) joins the original pair of hypotheses — an absorbing haze (Elliot *et al.* 1989) or a steep inversion layer (Eshleman 1989; Hubbard *et al.* 1990) — as a third possible model.

In Chapter 4, we derive the temperature and abundance of the methane in Pluto's atmosphere by measuring the strengths and shapes of the R(0) line and Q branch of the 1.67 μm methane feature. Since we used a high spectral resolution, the sharp rotational features of the gaseous methane are clearly distinguishable from the broad absorption of the surface frost.

In Chapter 5, we investigate the structures for the lower atmosphere that are consistent with these and other observations, under the assumptions of hydrostatic and vapor-pressure equilibrium. These structures have implications for the bulk density of Pluto.

CHAPTER 2
MASSES OF PLUTO AND CHARON*

2.1 INTRODUCTION

From the densities of Pluto and Charon, one can derive the rock-ice fractions of these bodies. This reflects the cosmochemical abundances at the time of their formation and their evolution. Also, the relative densities of Pluto and Charon can constrain scenarios for the formation of the Pluto-Charon binary (McKinnon 1989). The masses control the dynamics of the system, including the time scales for tidal lock and the escape rates of volatiles. Furthermore, the relative masses are necessary for predictions of stellar occultations. For example, a change in Charon's assumed density from 1 to 2 g cm^{-3} can move the predicted position of Pluto's shadow by more than half its width.

The computed densities are functions of the radii, the system mass, and the ratio of the two masses. Radii of Pluto and Charon have been measured from the mutual events and from stellar occultations (Fig. 2.1). One stellar occultation has been observed for each body. Elliot and Young (1991) reanalyzed a 1980 occultation by Charon (Walker 1980) and found a 3-σ lower limit on Charon's radius of 601.5 km. Millis *et al.* (1993) performed a joint solution of all observations of the 1988 occultation by Pluto, using the occultation light curve model for small bodies developed by Elliot and Young (1992). They find that Pluto's radius is 1195 ± 5 km if the lower atmosphere is clear, and smaller than 1180 ± 5 km if there is a haze layer. Tholen and Buie (1990, hereafter TB90) found Pluto and Charon radii of 1151 ± 6 km and 593 ± 13 km from their analysis of the mutual-event season. Larger radii (1164 ± 23 km and 621 ± 21 km) were found by

---

* This chapter is based on Young, L. A., C. B. Olkin, J. L. Elliot, D. J. Tholen, and M. W. Buie 1994. The Charon-Pluto mass ratio from MKO astrometry. Icarus (in press), copyright 1994, Academic Press. Minor cosmetic changes include changing "paper" to "chapter," changing the numbering of the equations, figures, and tables, and the incorporation of the discussion and conclusions sections into other sections of the thesis.

E. Young and Binzel (1994), from an independent mutual-event dataset. The scale of the system for the mutual events is set by a, the semimajor axis of Charon's orbit around Pluto. TB90 used a = 19640 km (Beletic *et al.* 1989). More recent observations suggest a smaller semimajor axis (Null *et al.* 1993, hereafter NOS93), which decreases the mutual-event values for Pluto's radius by 14 km, and Charon's radius by 7 km.

Pluto and Charon orbit around the system barycenter with semimajor axes a_p and a_c. The ratio of their masses ($q = M_c / M_p$) equals the ratio of these semimajor axes, and the sum of their masses is proportional to a^3. Thus, the individual masses can be found by measuring $a = a_p + a_c$ and $q = a_p/a_c$. NOS93 measured a and q by observing the motion of Pluto and Charon on CCD images obtained with the Hubble Space Telescope (HST) in August 1991. The results of HST observations from August 1993 have not yet been reported. These observations of NOS93 suffered from 3 major limitations: (i) the reimaging optics introduced large field distortions; (ii) only one star was present in the same field as Pluto, so Pluto itself had to provide the relative orientations of the observations; and (iii) only half of the Charon orbital period was observed.

Our approach avoids these limitations and provides an independent measurement of the masses. The large field of view available on ground-based telescopes afforded us the following advantages: (i) the telescope could be used in direct imaging mode, where the optics introduce negligible field distortion; (ii) ten field stars were observed in our field, allowing for precise registration of exposures; and (iii) Pluto and Charon remained within this set of ten field stars on 6 successive nights of observation, or 78% of the orbit. Although the images of Pluto and Charon are usually blended in ground-based observations, the image can be successfully modeled as the sum of two point sources. For example, Jones *et al.* (1988) measured the separation of Pluto and Charon with a standard deviation of 0.004 arcsec. The data on our best night reach a similar precision.

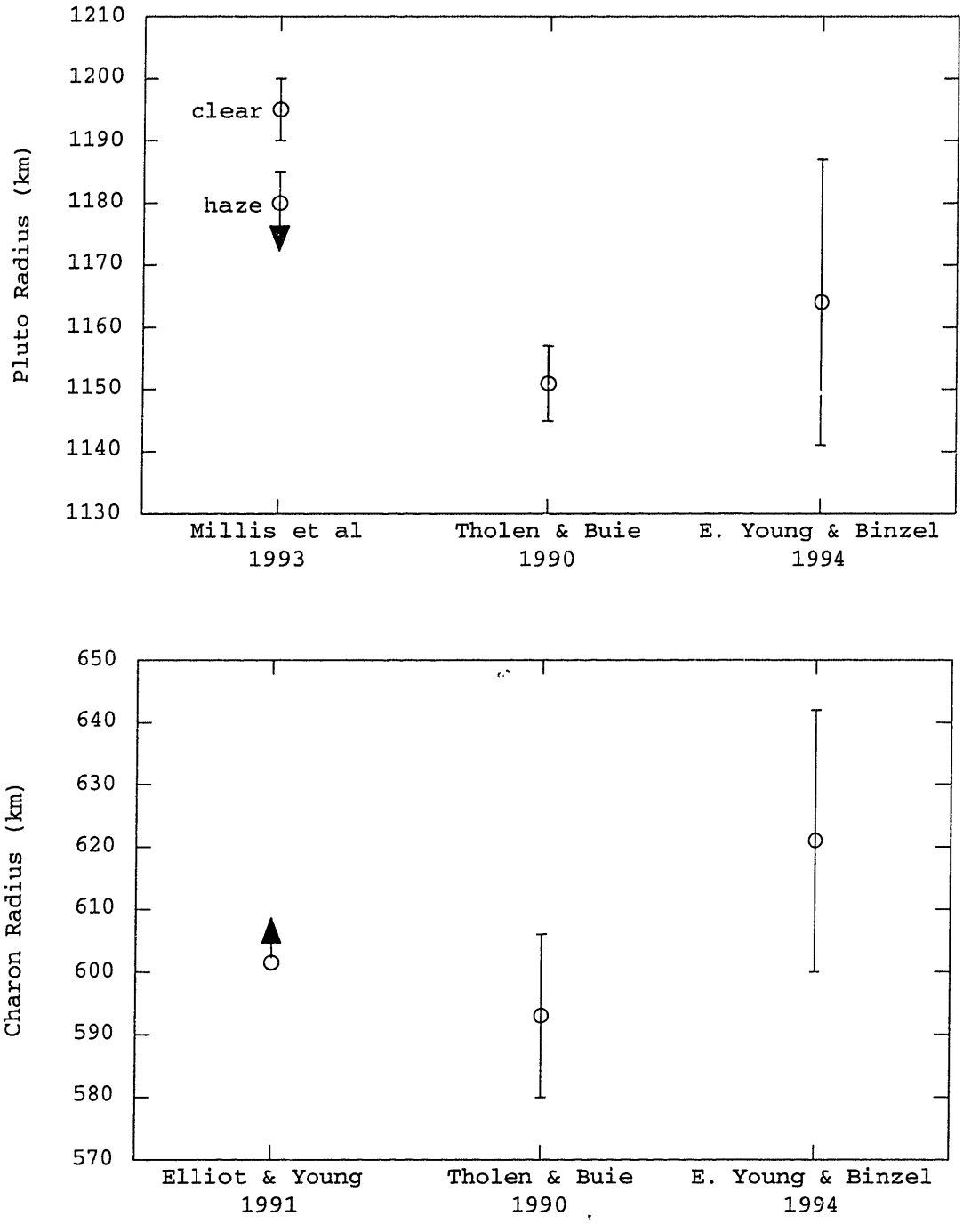

Figure 2.1. Radii of Pluto and Charon. The radii from Millis *et al.* (1993) and Elliot and Young (1991) are derived from stellar occultations. The radii of Tholen and Buie (1990) and E. Young and Binzel (1994) are derived from the mutual-event season.

2.2 OBSERVATIONS

We obtained images of Pluto, Charon, and field stars from 1992 February 26 to March 2 with the University of Hawaii 2.2-m telescope at Mauna Kea. The telescope is an f/10 Ritchey-Chrétien, which we used in direct imaging mode for maximum transmission and minimum field distortion. The detector, a 1024x1024 Tektronics CCD, had a nominal image scale of 0.22 arcsec per pixel for a field of view of 225 arcsec on a side. Images were taken with B, V, R, and I filters, and are used to find the rotational light curves of Pluto and Charon in these filters (Olkin *et al.* 1993). The center-of-light offsets (Buie *et al.* 1992) are calculated for observations in the B filter, so only the B exposures are included in this chapter.

Our observing run consisted of the two hours before each morning twilight on 1992 February 25 to March 2. High winds precluded observations on February 25, and delayed the start of observations on February 26. Table 2.1 shows a log of our observations. We increased our data rate by taking multiple exposures before reading out the CCD, moving the telescope 10 arcsec south between exposures. The telescope tracked at the Pluto rate. We typically took 4 exposures of 60 seconds each before reading out the CCD, with approximately 10 seconds between exposures. Asteroid 1981 Midas was also observed to establish the plate constants from its motion across the field. This object was chosen for three reasons: (i) the motion was known to within a few parts in 10^6 (Marsden 1989); (ii) Since Midas is a fast-moving near-Earth asteroid, it crossed the field of view in less than an hour, which made it feasible to observe Midas while still getting good coverage on Pluto; and (iii) Midas was 6° - 15° from Pluto during the observing run. Four exposures of the Midas field were taken before reading out the CCD. The telescope tracked at the sidereal rate during observations of Midas, and was not offset between exposures.

Table 2.1. Observation Log

Date 1992	Time (UT)	Object	FWHM (")	Predicted Separation (")	Exposures Converged / Observed	Ctr. of Light (km)[a] Pluto Δx	Pluto Δy	Charon Δx	Charon Δy
Feb. 26	15:29 – 16:03	Pluto	1.24	0.75	15 / 18	58	80	51	4
Feb. 27	14:05 – 14:33	Pluto	1.20	0.88	16 / 16	–90	52	51	45
	14:37 – 15:42	Midas	–	–	32 / 32	–	–	–	–
	15:47 – 15:50	Pluto	1.21	0.86	4 / 4	–86	49	47	46
Feb. 28	13:55 – 14:43	Midas	–	–	28 / 28	–	–	–	–
	14:48 – 15:17	Pluto	1.23	0.30	4 / 16	–7	38	–49	18
Feb. 29	13:52 – 14:17	Pluto	0.88	0.59	4 / 14	–8	53	–46	7
	14:24 – 15:16	Midas	–	–	21 / 21	–	–	–	–
	15:20 – 15:25	Pluto	1.02	0.63	2 / 4	–7	53	–42	8
Mar. 1	13:58 – 14:10	Pluto	0.98	0.91	8 / 8	–39	58	3	24
	14:20 – 15:05	Midas	–	–	28 / 28	–	–	–	–
	15:11 – 15:29	Pluto	0.91	0.91	12 / 12	–43	57	3	24
Mar. 2	13:51 – 14:27	Pluto	0.99	0.46	19 / 20	–1	24	–20	–6
	14:40 – 15:23	Midas	–	–	28 / 28	–	–	–	–

[a] The offset from the center of each body to the center of light, determined from the albedo map of Buie*etal.* 1992. The +x direction is toward the receding limb and the +y direction is toward Pluto's or Charon's rotational north pole.

Because Pluto passed through a stationary point in right ascension during the observing run, the motion was primarily in declination and spanned only 138 arcsec. Pluto could therefore be captured in a single field during the 6-day observing run (Fig. 2.2). Two occultation candidate searches report approximate positions for stars near Pluto's path. One search was conducted at the Smithsonian Astrophysical Observatory (SAO) with observations from Lick Observatory (Mink *et al.* 1991), using the Perth 70 catalog for reduction to a standard reference frame (Høg and von der Heide 1976). A deeper search was conducted at the Massachusetts Institute of Technology with observations from MIT's Wallace Astrophysical Observatory in Westford, MA (Dunham *et al.* 1991), using the Lick-SAO positions as a secondary astrometric network. The IDs used in this paper were assigned by the MIT occultation search team. We performed photometry of selected field stars in 1992 June at Lowell Observatory in Flagstaff, AZ. These observations are summarized in Table 2.2.

Table 2.2. Astrometry and photometry of field stars

MIT occultation search (Dunham *et al.* 1991)				Lick-SAO occultation search (Mink *et al.* 1991)				Lowell photometry (This work)		
ID	α (J2000)	δ (J2000)	mag[a]	ID	α (J2000)	δ (J2000)	V[b]	B	V	R
202	15 37 28.78	-4 01 19.4	13.3	1497	15 37 28.798	-4 01 19.40	14.3	14.60	13.69	13.20
203	15 37 29.30	-4 01 05.6	13.1	1499	15 37 29.311	-4 01 05.26	14.1	14.27	13.46	13.03
206	15 37 31.63	-4 01 51.7	12.4	1502	15 37 31.642	-4 01 51.35	13.7	14.26	12.93	12.22
211	15 37 34.02	-4 01 25.6	15.1	1506	15 37 34.029	-4 01 25.67	15.1	16.54	15.52	15.01
213	15 37 35.80	-4 00 01.3	16.6							
215	15 37 36.53	-4 00 02.8	15.5	1510	15 37 36.540	-4 00 02.72	15.2	16.64	15.79	15.30
218	15 37 37.62	-4 02 35.5	15.9	1511	15 37 37.632	-4 02 35.50	15.3			
220	15 37 38.23	–3 59 06.5	15.0	1514	15 37 38.222	–3 59 06.34	15.2			
221	15 37 38.22	-4 01 57.9	17.5							
223	15 37 40.98	–3 59 16.3	17.5							

[a] CCD with no filter (approximately R magnitude).
[b] Approximate magnitude

The frames were calibrated in the standard manner, with bias subtraction, dark subtraction, and flat fielding. Bias levels were found for each frame from an overscan region. The dark current, determined from a 3600-second dark exposure, was less than 1 ADU (Analog to Digital Unit) for the Pluto exposures. The flat for each night was the median of 3 or 4 dome flats. These flats appeared adequate: out-of-focus dust grains visible on the flats were undetectable in the flattened images.

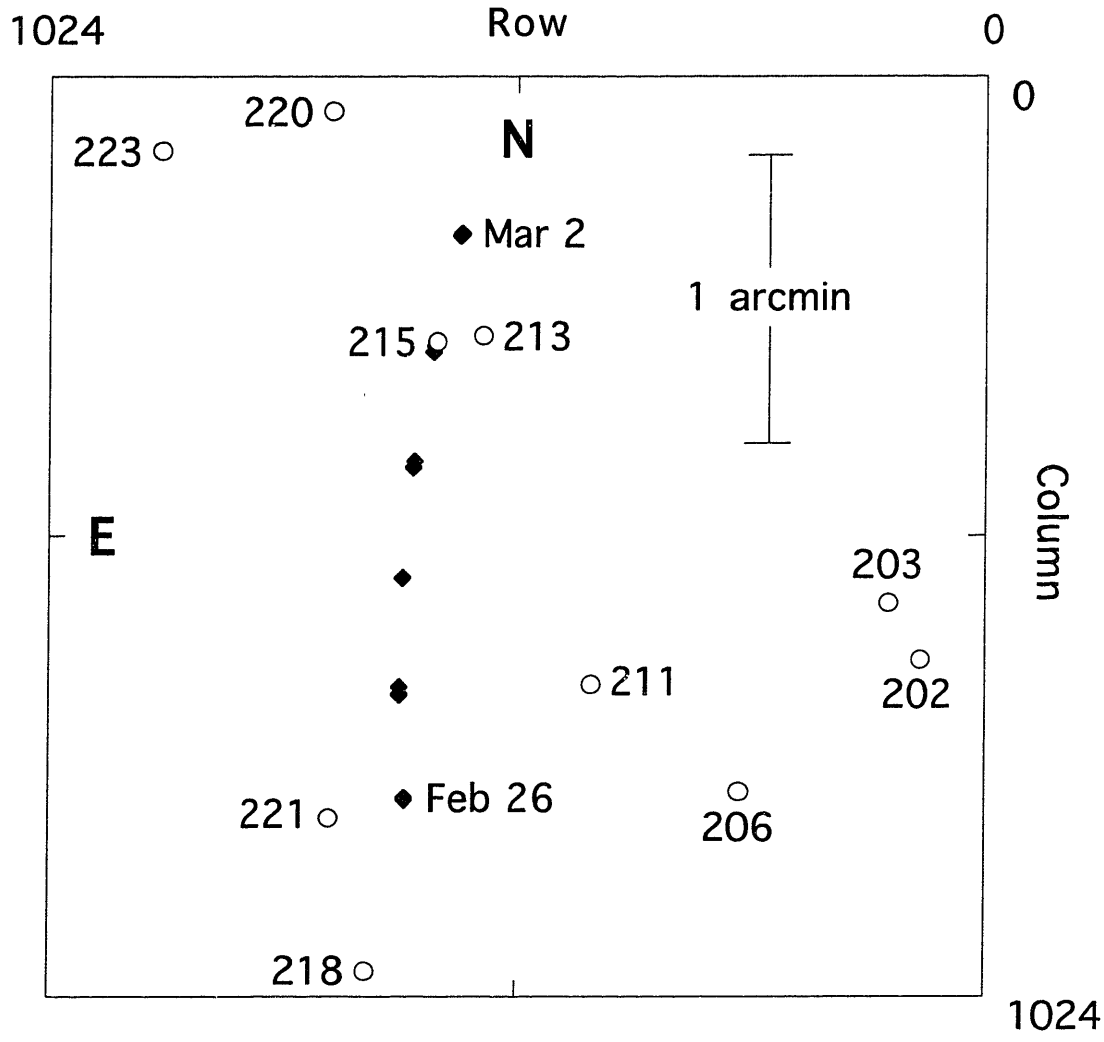

Figure 2.2. Pluto and field stars for 1992 February 26 - March 2 The open circles and 3-digit IDs mark the mean positions of the field stars brighter than ~18 mag. The black diamonds mark the location of Pluto on each of the 6 nights of observation. On February 27, February 29, and March 1, the distance Pluto covered in a single night is indicated by double diamonds. The dates of the first and last nights of observations are indicated. The image scale was 0.22 arcsec/pixel.

2.3. ANALYSIS

2.3.1 CENTERS OF PLUTO, CHARON, MIDAS, & FIELD STARS

Least-squares fitting of point-spread functions (PSFs) is an effective method for analyzing crowded fields. The stars on the field define the PSF, which is then fit to all objects of interest to find centers and brightnesses. In our analysis, most of the steps used the IRAF implementation of DAOPHOT (Stetson 1987). Ordinarily, DAOPHOT determines the background for a star from a sky annulus. Because of the multiple exposures, every star in the Pluto field has one or two stars 10 arcsec away that could inflate the estimate of the local background. To avoid this, we removed the background by fitting a second-order polynomial through the local background (determined by the median of the surrounding 100 × 100 box). Because DAOPHOT assigns weights based on Poisson statistics, a constant was added back to the image to restore the mean background level. This constant was used as the background for that frame in subsequent analyses.

The PSFs were constructed from field stars with the PSF routine of DAOPHOT. For the Pluto-Charon frames, the PSFs did not include star 206 (its profile was noticeably narrower than those of the other field stars), star 211 (it had two faint stars 3 arcsec away), and, for the night of March 1, star 215 (it was too close to Pluto and Charon). It is not clear why star 206 is narrower than the other stars; however, it is both the reddest and the brightest, and we felt it was safer to leave all suspect stars out of the PSF. Because the Pluto field was offset between exposures, star 218 never appears on the first exposure, and star 220 never appears on the fourth. For the Midas frames, the PSF simply included the five to ten brightest field stars.

We used the NSTAR routine of DAOPHOT to fit for the centers and brightnesses of objects on the Pluto exposures. As with all PSF-fitting routines, NSTAR attempts to minimize the weighted sum of the squares of the values in the residual image. The blended images of Pluto and Charon were modeled as the sum of two PSFs. Pluto and Charon were fit simultaneously, and star 215 was included in the simultaneous fit for the night of March 1. Figs. 2.3 and 2.4 show the results of a fit to a typical blended Pluto-Charon image. NSTAR was originally designed for crowded-field photometry of stars; if the signal-to-noise ratio of the dimmer of two objects in a simultaneous fit is too low, the routine interprets this as an erroneous detection of the second object. The number of exposures for which the fit successfully converged is listed in Table 2.1. As NSTAR does not report the errors in the centers it finds, errors were assigned to the centers on the basis of the width of the best-fitting Gaussian and the errors in the signal (King 1983):

$$\frac{\sigma_x}{w} = k\frac{\sigma_s}{s} \tag{2.1}$$

where σ_x is the error in the position, w is the width of a Gaussian, σ_s is the error in the peak signal, and s is the peak signal. The coefficient k depends on the shape of the PSF; we used $\sqrt{2}$, which is appropriate for a Gaussian PSF.

Because of the large albedo variation over Pluto's surface, the fitted centers of Pluto and Charon were the centers of light, not the centers of disk. From the maximum-entropy solution to the mutual event and rotational light curves (Buie *et al.* 1992), we calculated the predicted distance between the center of light and the center of disk for each exposure. Table 2.1 includes the average offsets in x (toward the receding limb) and y (toward the rotational north pole). These were converted to offsets in row and column from a preliminary solution for the orbit and plate constants, and subtracted from the center-of-light positions.

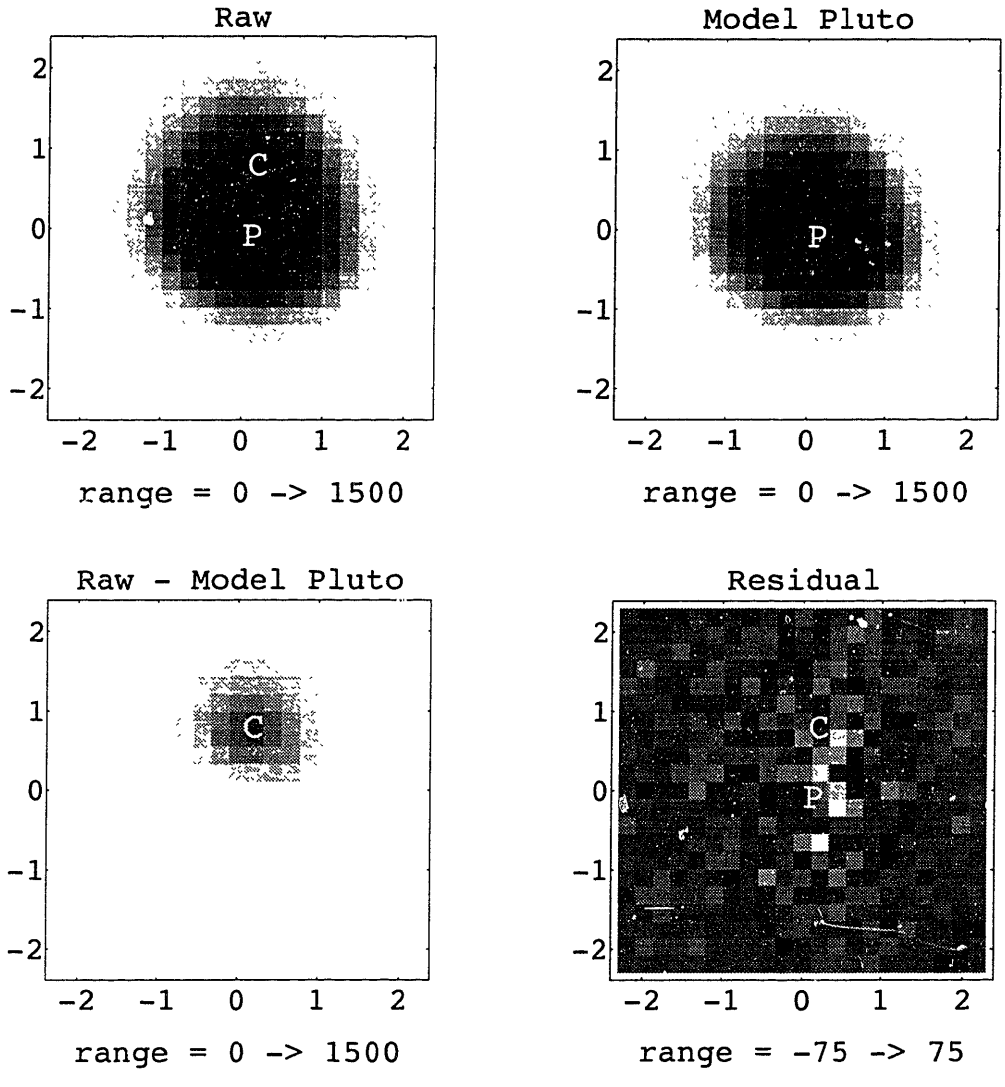

Figure 2.3. Typical Pluto/Charon image. The upper left shows the image after background subtraction. The letters "P" and "C" mark the positions of Pluto and Charon. A simultaneous fit was performed for the centers and brightnesses of Pluto and Charon. The model Pluto, in the upper right, is a scaled and shifted model PSF. The lower left shows the image with the model Pluto subtracted. The remaining image, which should be just Charon, has the same shape as the model Pluto. The lower right shows the residual when both the model Pluto and the model Charon are subtracted. The scale is increased by a factor of 10, and no systematic residual is apparent. The axes are marked in arcsec. North is up and east is to the left.

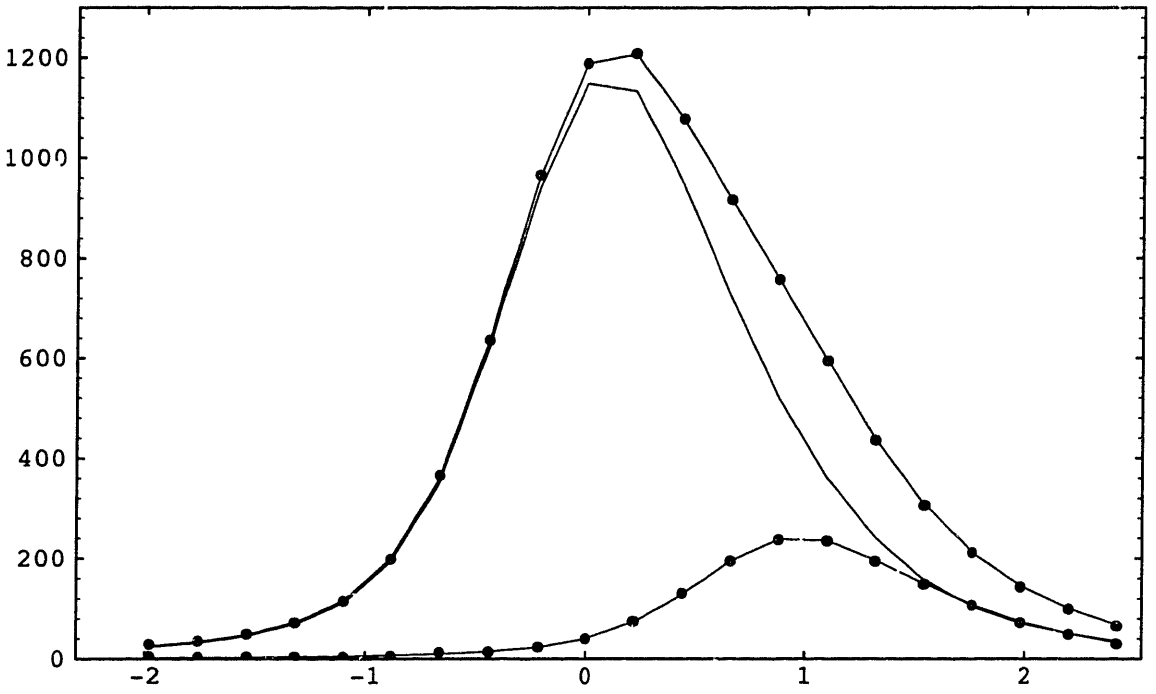

Figure 2.4. Typical Pluto/Charon image (marginal column). A marginal column is the average of all the columns in an image, such as the images of Fig. 2.3. The upper set of points is the raw data (upper left in Fig. 2.3). The lower set of points is the raw data with the model Pluto subtracted (lower left of Fig. 2.3). The lines are (from lowest to highest) the model Charon, the model Pluto, and the sum of the two model PSFs.

Since Midas moved 7 to 12 pixels during an exposure, the PSF was convolved with Midas' motion to model the elongated image. The "Midas-spread function" was fit to the Midas images and the unconvolved PSF to the field stars. Because DAOPHOT does not handle this case easily, we used our own least-squares package.

2.3.2 REGISTRATION OF EXPOSURES

The star centers defined the astrometric relationship between the different exposures. A set of coefficients (a_{ij}, b_{ij}) linearly converted the rows and columns (r and c) for a given exposure to the transformed rows and columns (r_{trans} and c_{trans}) of a reference frame:

$$\begin{aligned} r_{trans} &= a_{00} + a_{10}r + a_{01}c \\ c_{trans} &= b_{00} + b_{10}r + b_{01}c \end{aligned} \qquad (2.2)$$

We built up the reference frame by minimizing the weighted scatter of each star's transformed positions around its mean transformed position. One exposure was chosen to define the absolute scale of the reference frame; for this exposure, $r = r_{trans}$ and $c = c_{trans}$. The Pluto and Charon positions are transformed to the reference frame as well.

The Midas frames for each night were registered in a similar manner. Since the Midas observations were used to determine the image scale and orientation, the centers of the field stars and Midas were corrected for differential aberration and refraction before the exposures were registered. The differential changes in position were cast as linear equations in row and column, using the linear terms from Green (1985, Eq. (13.24) and (13.32)). Correcting for differential refraction and aberration decreased the image scale by 3 parts in 10^4 and had no significant effect on the orientation.

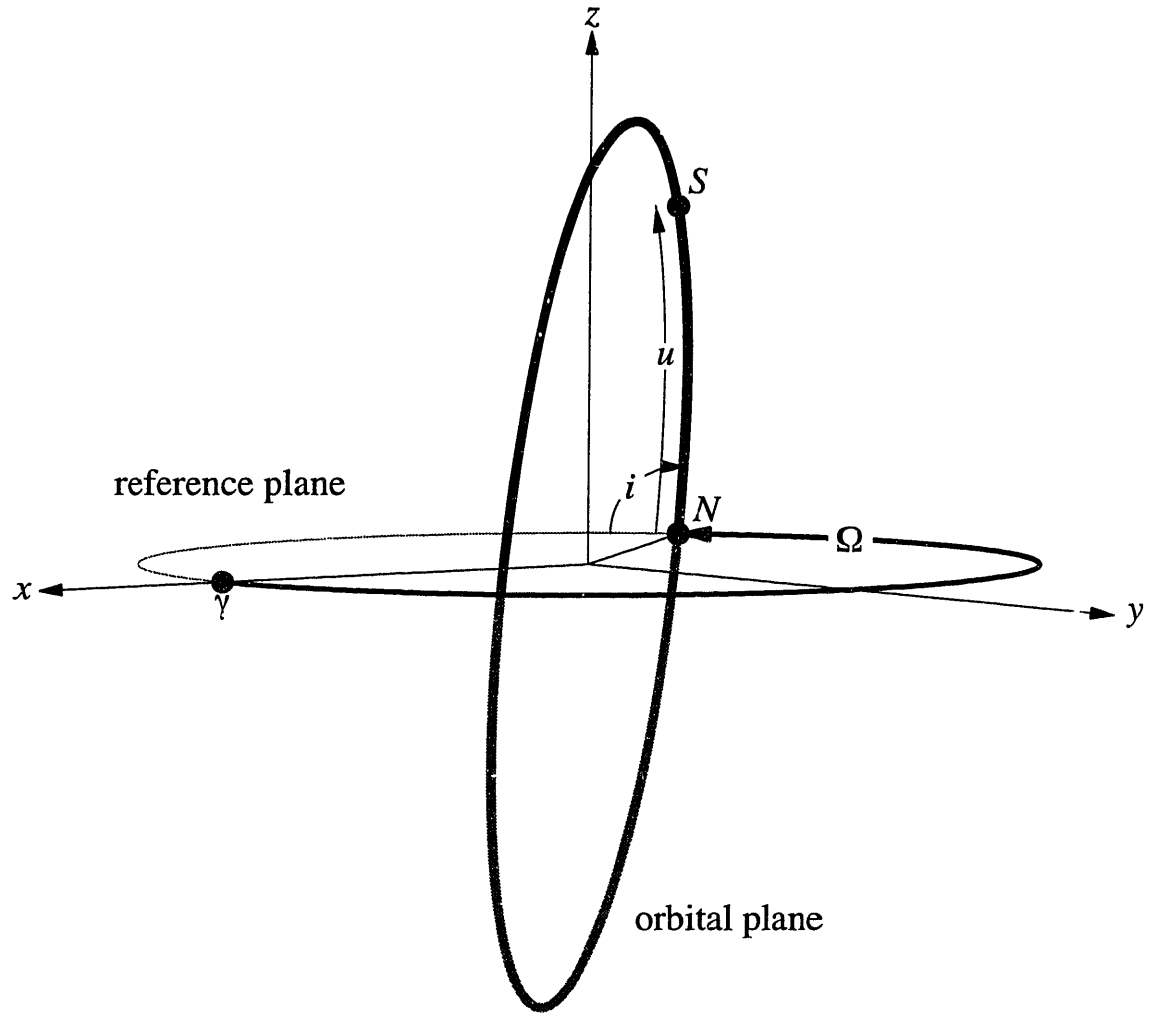

Figure 2.5. Orbital elements. The apparent ellipse depicted was generated using Charon's orbital elements. The line-of-sight vector is perpendicular to the paper, so this figure depicts Charon's orbit as seen from Earth. The angles indicated are the longitude of the ascending node (Ω), the inclination (i), and the argument of latitude (u). The dots indicate the position of the satellite (S), the ascending node (N), and the origin of the longitude (γ).

2.3.3 MODEL ROWS AND COLUMNS

The first step in calculating the rows and columns of Pluto and Charon is finding the apparent orbit of Charon around Pluto. TB90 found that the eccentricity of Charon's orbit around Pluto was 0.00020±0.00021, unless the line of apsides happens to be along the line of sight, in which case it could be as high as 0.01. The eccentricity is assumed to be

zero for this analysis. The remaining orbital elements, shown in Fig. 2.5, are the inclination (i), the longitude of the ascending node (Ω), the argument of latitude (u, identical to TB90's "mean anomaly, measured from the ascending node"), and the semimajor axis of Charon's orbit around Pluto (a, not shown).

All calculations involving the right ascension (α) and declination (δ) are performed in tangent-plane ("standard") coordinates (ξ and η). These are obtained by gnomonic projection: the projection of the celestial sphere onto a plane tangent at a given right ascension and declination (α_0, δ_0) (Green 1985, Eq. (13.12)):

$$\xi = \frac{\cos\delta \sin(\alpha - \alpha_0)}{\sin\delta_0 \sin\delta + \cos\delta_0 \cos\delta \cos(\alpha - \alpha_0)}$$

$$\eta = \frac{\cos\delta_0 \sin\delta - \sin\delta_0 \cos\delta \cos(\alpha - \alpha_0)}{\sin\delta_0 \sin\delta + \cos\delta_0 \cos\delta \cos(\alpha - \alpha_0)} \qquad (2.3)$$

From the orbital elements and the position of the barycenter (α_b and δ_b), the difference in the standard coordinates of Pluto (ξ_p, η_p) and Charon (ξ_c, η_c) is adequately defined by:

$$\begin{bmatrix} \xi_c - \xi_p \\ \eta_c - \eta_p \end{bmatrix} = \frac{a}{\Delta} \begin{bmatrix} -\sin(\alpha_b - \Omega) & \cos(\alpha_b - \Omega)\cos i \\ -\cos(\alpha_b - \Omega)\sin\delta_b & -\sin(\alpha_b - \Omega)\sin\delta_b \cos i + \cos\delta_b \sin i \end{bmatrix} \cdot \begin{bmatrix} \cos u \\ \sin u \end{bmatrix} \qquad (2.4)$$

where Δ is the Earth-Pluto distance.

The rotational phase (p) and (under the assumption of a circular orbit) the argument of latitude increase at a constant rate, starting from initial values p_0 and u_0 defined at an initial Julian date, JD_0. If JD is the time of observation, then

$$\frac{u - u_0}{360^\circ} = p - p_0 = \frac{JD - (\Delta / c) - JD_0}{P} \qquad (2.5)$$

where c is the speed of light (173 AU/day), and P is the period, for which we adopt 6.387246 ± 0.000011 days from TB90. To compare results with TB90, we use their epoch, JD2446600.5. At 1992 Mar 1 9:53:27 UT, an integral number of orbits had occurred since JD_0, so at that time $u = u_0$ and $p = p_0 = 0.46111$. The phase is calculated using the definition of Binzel *et al.* (1985), with the substitution of TB90's value for the period.

The standard coordinates relative to the barycenter depend on the mass ratio, q:

$$\begin{bmatrix}\xi_p\\ \eta_p\end{bmatrix} = \begin{bmatrix}\xi_b\\ \eta_b\end{bmatrix} - \frac{q}{1+q}\begin{bmatrix}\xi_c - \xi_p\\ \eta_c - \eta_p\end{bmatrix}$$

$$\begin{bmatrix}\xi_c\\ \eta_c\end{bmatrix} = \begin{bmatrix}\xi_b\\ \eta_b\end{bmatrix} + \frac{1}{1+q}\begin{bmatrix}\xi_c - \xi_p\\ \eta_c - \eta_p\end{bmatrix} \qquad (2.6)$$

We generated a light-time corrected, geocentric, J2000 ephemeris of the barycenter at 10-minute intervals from JPL's DE202 ephemeris (Standish 1987) using the SPICELIB library provided by the NAIF group at JPL (Acton 1990). These were linearly interpolated to the times of observations, and converted to topocentric α and δ. We then calculated ξ_b and η_b from Eq. (2.3), choosing a tangent point whose J2000 position was near the center of the CCD: $\alpha_0 = 15^h\ 37^m\ 35^s$, $\delta_0 = -4°\ 00'\ 55''$.

The standard coordinates were transformed linearly to the row and column of the reference frame using the plate constants m_{11}, m_{12}, m_{21}, and m_{22}.

$$\begin{bmatrix}r_{trans}\\ c_{trans}\end{bmatrix} = \begin{bmatrix}r_0\\ c_0\end{bmatrix} + \begin{bmatrix}m_{11} & m_{12}\\ m_{21} & m_{22}\end{bmatrix}^{-1} \times \begin{bmatrix}\xi\\ \eta\end{bmatrix} \qquad (2.7)$$

The free parameters (q, a, i, Ω, u_0, m_{11}, m_{12}, m_{21}, m_{22}, r_0, c_0) were adjusted to minimize (in a least-squares sense) the difference between the model and observed rows and columns.

2.4. RESULTS

In this section, we apply the model of Section 2.3 to the Pluto and Charon centers. In the first battery of fits (Table 2.3a), we do not constrain any parameters. We first apply the model to all converged Pluto and Charon centers (Fit #1). The night of February 28 is a poor fit to the model for the following reasons: (i) we will see in Section 2.5 that the position of Charon is particularly sensitive to the shape of the constructed PSF on this night; (ii) the FWHM is large while the separation is small; (iii) only 4 out of 16 exposures converged; and (iv) the errors assigned to the Charon centers on February 28 were seven times larger than on the other nights. When the fitted data do not include February 28 (Fit #2), the mean residuals are much lower, but the mass ratio changes by only a third of its formal error. For the remainder of the paper, we exclude February 28 from the analysis. Fits #3 - 6 include just the first, second, third, or fourth exposure on each frame. Since the four exposures were offset from one another by 10 arcsec, fitting one exposure at a time tests if the results are strongly dependent on the locations of the images. The average scatter of the parameters for Fits #3 - 6 is close to twice the formal error of Fit #2, as expected because only one quarter of the data were used. The scatter for q is somewhat higher, at 3.2 times the formal error of Fit #2. We fit for the Pluto positions alone, in Fit #7. In this fit, we need to fix a, because we are effectively fitting for Pluto's orbital semimajor axis, $a_p = a\ q\ (1+q)^{-1}$. The amplitude of the Pluto wobble is consistent with Fit #2, but the other elements are not as well determined.

Table 2.3a: Sensitivity to choice of data. All parameters are unconstrained.

	Fit #1 All data	Fit #2 No Feb. 28	Fit #3 No Feb. 28 1st Exposures	Fit #4 No Feb. 28 2nd Exposures	Fit #5 No Feb. 28 3rd Exposures	Fit #6 No Feb. 28 4th Exposures	Fit #7 No Feb. 28 Pluto alone
q	0.1554 ± 0.0035	0.1565 ± 0.0035	0.1425 ± 0.0045	0.1581 ± 0.0055	0.1702 ± 0.0047	0.1555 ± 0.0048	0.1644 ± 0.0093
a (km)	19489 ± 64	19484 ± 64	19621 ± 91	19520 ± 103	19539 ± 83	19382 ± 74	(19484)[a]
i (deg)	95.17 ± 0.27	95.15 ± 0.27	95.12 ± 0.38	94.52 ± 0.43	95.16 ± 0.35	95.74 ± 0.34	87.80 ± 3.10
Ω (deg)	222.52 ± 0.86	222.46 ± 0.87	222.91 ± 1.01	222.09 ± 1.44	222.08 ± 1.17	223.28 ± 1.27	225.52 ± 8.99
u_0 (deg)	260.48 ± 0.64	260.37 ± 0.64	260.62 ± 0.75	259.71 ± 1.07	260.29 ± 0.91	260.41 ± 0.91	269.07 ± 7.42
m_{11}(mas/pix)	218.071 ± 0.157	218.086 ± 0.158	218.594 ± 0.196	217.899 ± 0.258	217.594 ± 0.207	217.806 ± 0.222	218.609 ± 1.079
m_{12}(mas/pix)	–0.601 ± 0.015	–0.602 ± 0.015	–0.642 ± 0.019	–0.576 ± 0.025	–0.554 ± 0.021	–0.599 ± 0.022	–0.722 ± 0.104
m_{21}(mas/pix)	–0.410 ± 0.120	–0.347 ± 0.122	–0.053 ± 0.150	–0.386 ± 0.200	–0.333 ± 0.171	–0.816 ± 0.180	0.697 ± 0.908
m_{22}(mas/pix)	–218.477 ± 0.016	–218.485 ± 0.016	–218.485 ± 0.021	–218.445 ± 0.027	–218.508 ± 0.024	–218.471 ± 0.027	–218.588 ± 0.088
r_0 (pix)	487.846 ± 0.089	487.854 ± 0.090	488.105 ± 0.111	487.745 ± 0.148	487.585 ± 0.119	487.723 ± 0.128	488.156 ± 0.614
c_0 (pix)	506.945 ± 0.069	506.911 ± 0.069	506.750 ± 0.085	506.921 ± 0.115	506.873 ± 0.098	507.193 ± 0.103	506.317 ± 0.517
σ_p (mas)	11	11	9	8	7	8	9
σ_c (mas)	56	22	20	20	23	19	–

[a] Parenthesized values were not fit.

In the second battery of fits (Table 2.3b), we used all the centers except those from the night of February 28, and fixed various parameters. The independently determined values and errors for the fixed parameters are parenthesized in Table 2.3b. Fit #8 fixes the shape of the orbit by fixing i, u_0, and Ω at the TB90 orbital elements, precessed to the J2000 equinox. TB90's formal errors in u_0 and Ω are smaller than those from the imaging observations of this work (Fit #2) and NOS93. This is true even if we consider the additional 0.20° error in u_0 that arises from propagating the error in the period forward from JD_0. The mutual events are most sensitive to the elements best measured at minimum separation: the timing of the orbit (controlled mainly by u_0) and the width of the apparent ellipse (controlled mainly by Ω). In contrast, imaging is more sensitive to those elements measured at elongation: the semimajor axis of the orbit (controlled entirely by a) and the orientation of the apparent ellipse (controlled mainly by i). Fit #9 uses u_0 and Ω from TB90. Because Fit #9 is consistent with the unconstrained fit (Fit #2), with fewer degrees of freedom, we adopt Fit #9 as our solution.

We can determine the plate constants from the motion of Pluto, the motion of 1981 Midas, and the locations of the field stars. Midas moved in essentially a straight line across the field, providing the image scale and orientation. These are converted to plate constants ($m_{11}, m_{12}, m_{21}, m_{22}$) for Fit #10, and adjusted for the differential refraction and aberration appropriate for the reference frame. For Fit #11, we fixed the plate constants at those determined by an unweighted fit of the mean star positions to the positions found by the MIT occultation search.

Fits #1 - 11 all give mass ratios much larger than the value of 0.0837 ± 0.0147 found by NOS93. Fit #12 demonstrates what happens when we force a small value of q on our observations. The rms Pluto residuals are 40% larger than those for the adopted solution.

Table 2.3b: Sensitivity to fixing parameters. All data except Feb 28.

	Fit #8	Fit #9[a]	Fit #10	Fit #11	Fit #12
	orbital elements from TB90	Ω and u_0 from TB90	plate constants from Midas	plate constants fromMIT astrom.	q from NOS93
q	0.1553 ± 0.0049	0.1566 ± 0.0035	0.1597 ± 0.0013	0.1736 ± 0.0047	(0.0837 ± 0.0147)[b]
a (km)	19542 ± 82	19460 ± 58	19464 ± 64	19392 ± 215	19428 ± 105
i (deg)	(99.10 ± 1.00)	95.00 ± 0.24	95.09 ± 0.27	91.78 ± 0.91	95.38 ± 0.45
Ω (deg)	(223.01 ± 0.03)	(223.01 ± 0.03)	223.41 ± 0.81	224.19 ± 2.77	222.46 ± 1.41
u_0 (deg)	(259.76 ± 0.08)[c]	(259.76 ± 0.08)[c]	259.63 ± 0.61	258.79 ± 2.06	260.99 ± 1.04
m_{11} (mas/pix)	218.196 ± 0.203	218.132 ± 0.144	(218.478 ± 0.061)	(219.164 ± 0.127)	218.688 ± 0.233
m_{12} (mas/pix)	-0.598 ± 0.020	-0.606 ± 0.014	(-0.621 ± 0.064)	(-0.985 ± 0.107)	-0.673 ± 0.023
m_{21} (mas/pix)	-0.395 ± 0.156	-0.390 ± 0.112	(-0.619 ± 0.260)	(-0.773 ± 0.167)	-1.100 ± 0.174
m_{22} (mas/pix)	-218.477 ± 0.022	-218.481 ± 0.016	(-218.471 ± 0.120)	(-218.505 ± 0.141)	-218.213 ± 0.017
r_0 (pix)	487.909 ± 0.115	487.880 ± 0.082	488.070 ± 0.005	488.572 ± 0.016	488.200 ± 0.132
c_0 (pix)	506.939 ± 0.089	506.935 ± 0.063	507.062 ± 0.004	507.140 ± 0.013	507.350 ± 0.098
σ_p (mas)	11	11	12	45	18
σ_c (mas)	44	24	27	74	27

[a] Adopted solution

[b] Parenthesized values are not fit. The parenthesized errors, taken from the same sources as the corresponding values, do not affect the fit in any way and are included for comparison only.

[c] This is the error for u_0 at JD_0. Due to the 5.7-year span between JD_0 and the observations, the effective error in u_0 increases to 0.22 deg.

Pluto's barycentric orbit and residuals for the adopted solution and for the low-q solution are shown in Fig. 2.6. For the adopted solution, the nightly means in the residuals of $\eta_p - \eta_b$ are scattered around zero. In contrast, the nightly mean residuals for the low-q

solution are as large as 26 milliarcsec, and the residuals are quantitatively sinusoidal. Clearly, we did not achieve a good fit when we fixed the mass ratio at such a low value.

The results from this work, TB90, and NOS93 are summarized in Table 2.4. When comparing with the previous results, note that the elements in TB90 are referred to the equator of B1950 and have been precessed to J2000 in this work and NOS93.

Table 2.4. Bulk properties for Pluto and Charon

	TB90	NOS93	This Work[a]
Semimajor axis, a (km)	19640 ± 320	19405 ± 86	19460 ± 58
Inclination[b], i (deg)	99.1 ± 1.0	96.56 ± 0.26	95.00 ± 0.24
Long. of ascending node[b], Ω (deg)	223.015 ± 0.028	(223.007 ± 0.041)	(223.015 ± 0.028)[c]
Argument of latitude[b], u_0 (deg)	259.76 ± 0.08	(260.00 ± 0.24)	(259.76 ± 0.08)[c]
Mass ratio, q	–	0.0837 ± 0.0147	0.1566 ± 0.0035
System mass, M_{sys} (10^{24}g)	14.72 ± 0.72	14.20 ± 0.19	14.32 ± 0.13
Pluto mass, M_p (10^{24}g)	–	13.10 ± 0.24	12.38 ± 0.12
Charon mass, M_c (10^{24}g)	–	1.10 ± 0.18	1.94 ± 0.04

[a] Fit #9
[b] Referred to the mean equator and equinox of J2000 at epoch JD 2446600.5
[c] Fixed at value from Tholen and Buie 1990.

The mass ratio is the main goal of this work and NOS93, and the values differ by nearly a factor of two. However, our semimajor axis is consistent with previous results (where the TB90 value is taken from Beletic *et al.* 1989). The elements Ω and u_0 were fixed at the TB90 values in this work. NOS93 describe how they constrained Ω and u_0 to be near the TB90 values. Both this work and NOS93 find a smaller inclination than TB90, although the differences among all three inclinations are larger than the formal errors. This difference is not due to a real change in the inclination, as the observations of NOS93 and this work were taken only 6 months apart. The ~0.25° error in the inclination implies an accuracy of about 0.4%, as does the ~70 km error in the semimajor axis. The apparent orbit of Charon around Pluto is shown in Fig. 2.7 for all three sets of elements, along with the observed offsets.

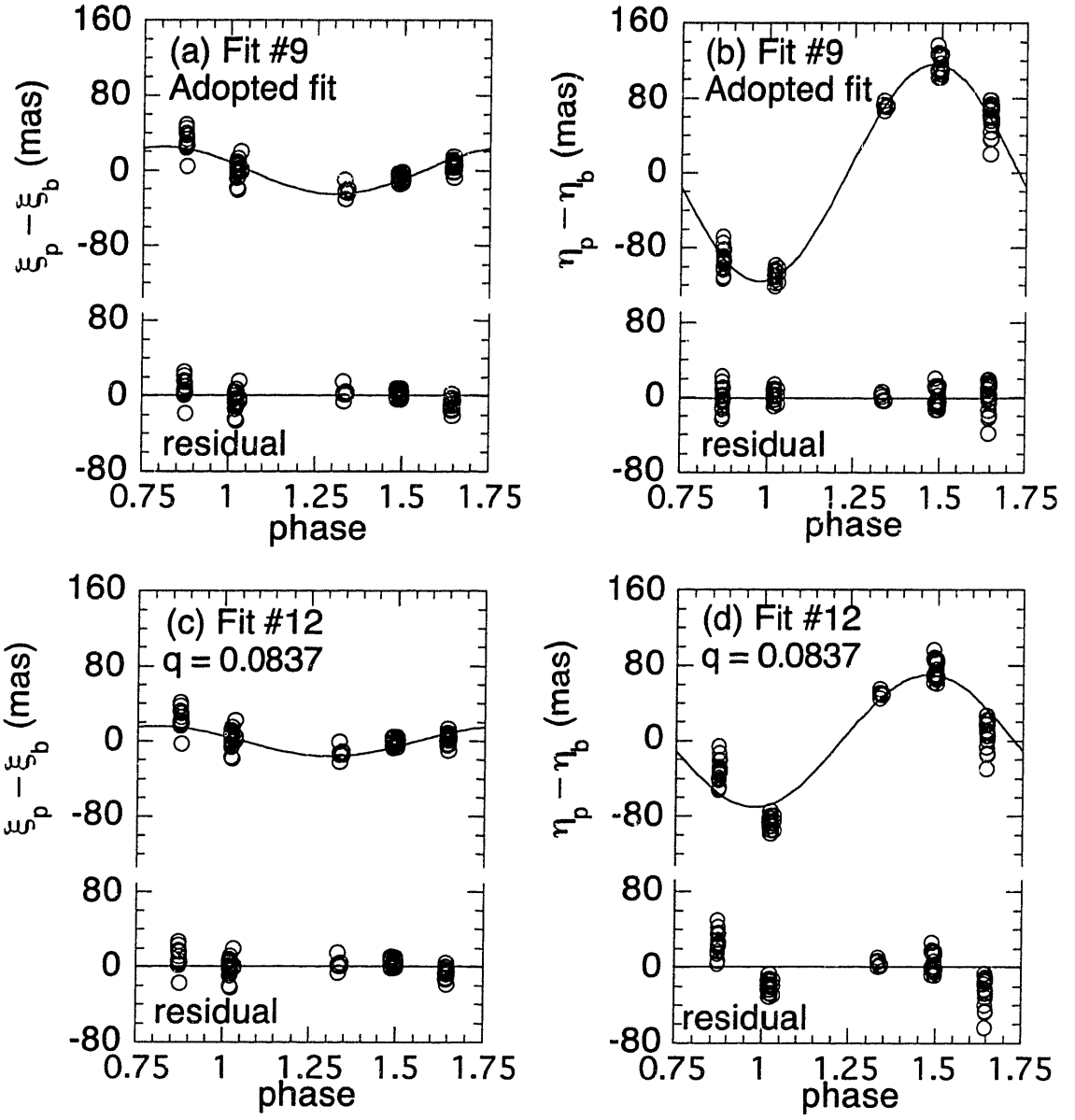

Figure 2.6. Pluto's distance from the barycenter in the direction of increasing right ascension ($\xi_p - \xi_b$) and increasing declination ($\eta_p - \eta_b$). Shown are (a) $\xi_p - \xi_b$ for the adopted fit, (b) $\eta_p - \eta_b$ for the same fit, (c) $\xi_p - \xi_b$ for the low-q fit, and (d) $\eta_p - \eta_b$ for the same fit. In the upper portion of each plot, the curve is the model separation and the open circles are the observed separations. The lower portion shows the residuals, at the same vertical scale. Note that the nightly means of the η residuals are clustered around zero for the adopted fit, but are as large as 26 milliarcsec when q is fixed at the value from NOS93.

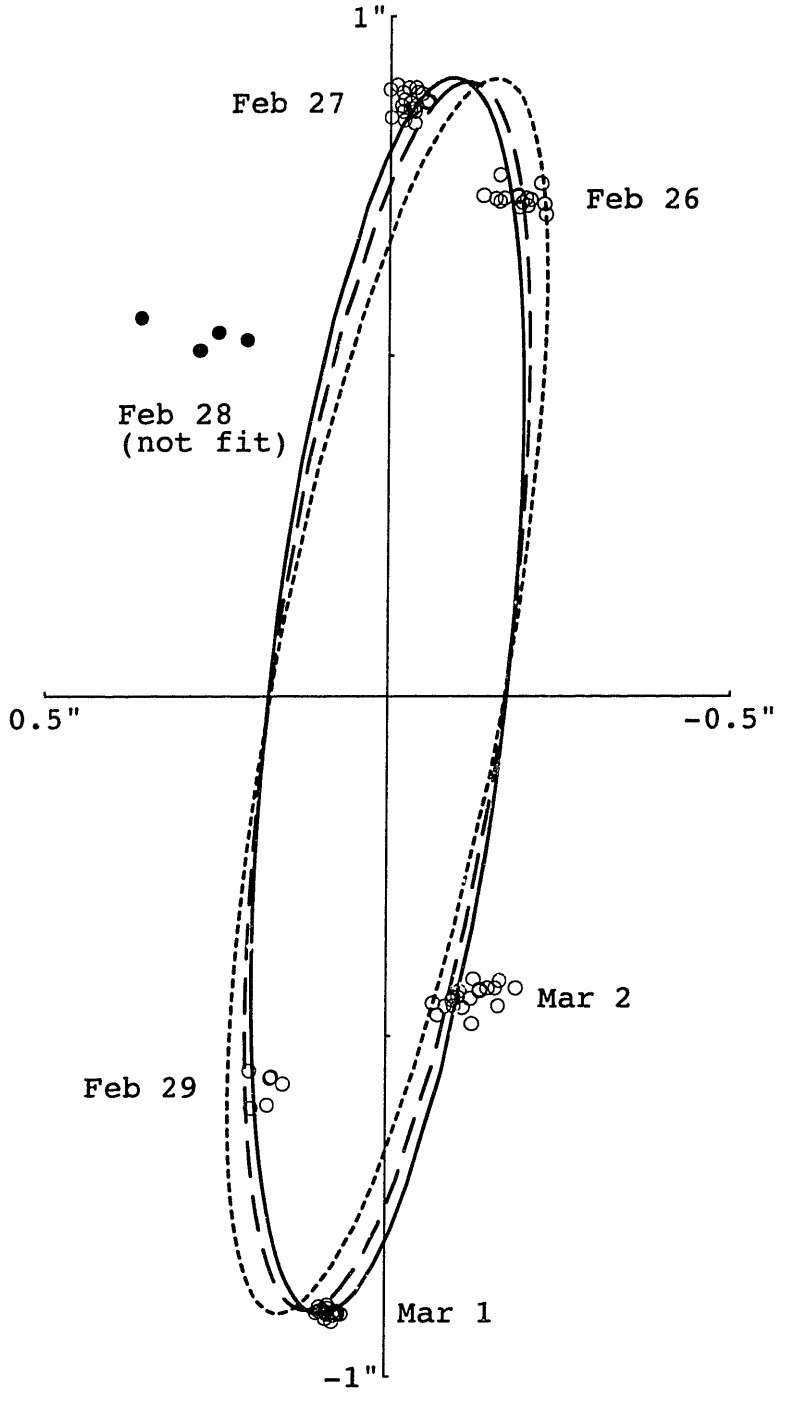

Figure 2.7. Charon's orbit around Pluto. The solid line is the adopted solution (Fit #9). The open circles are the observations that were included in the fit. The solid circles were excluded. The dashed line is the orbit from NOS93, and the dotted orbit is for TB90. North is up and east is to the left.

2.5. BOUNDS ON SYSTEMATIC ERRORS

This section investigates possible sources of the difference in the measurement of q by this work and NOS93. The effect of random errors on the derived mass ratio should be reflected in its formal error. To the extent they can be modeled, systematic corrections should not degrade the results. Unmodeled or incorrectly modeled systematic corrections can lead to an incorrect measurement of the mass ratio. Table 2.5 summarizes the mean random error, the maximum systematic correction, and the associated error for the various steps in the analysis.

Table 2.5. Sources of random and systematic error.

	Random Error (milliarcsec)		Systematic Effects (milliarcsec)		Comments	
	this work	NOS93	this work	NOS93	this work	NOS93
Finding centers						
Pluto	± 5	± 2	0 ± 3	0 ± 0	blended,	distinct peaks,
Charon	± 24	± 8	0 ± 7	10±(3)	PSF from field stars	PSF from literature
Registration	± 2	± 2	0 ± 1	0 ± 46	6-10 field stars, full linear solution	1 field star, same scale for row & col
Field Distortion	0	0	0 ± 20	89 ± 2	direct imaging	reimaging optics
Center-of-light	0	0	4 ± (4)	10±(10)	Buie *et al.* (1992)	Buie & Tholen (1989)
# of exposures					80	14
Span of data					78% of orbit	50% of orbit

Both NOS93 and this work found the centers by PSF fitting. The formal errors in the centers were smaller for NOS93 than for this work, because their PSF had a smaller core. Balancing this, we use 80 observations for 5 nights spanning 6 nights, compared with NOS93's 14 observations, spanning 4 nights. PSF fitting can introduce systematic errors; if the constructed PSF is a bad match to Pluto at the distance of Charon, Charon's center and brightness are adjusted to compensate. As discussed in Section 4.4 of NOS93, their model PSF probably was an inexact match to the actual HST PSF. They established the required systematic correction by fitting the model PSF to synthetic "Pluto-Charon"

images constructed from field stars. They found the required systematic correction was up to 10 milliarcsec for Charon, with no significant effect on Pluto. They do not quote an error in the correction, but state that "the larger, well-determined corrections were usually about twice as large as the corresponding solution scatter and were roughly the same for different choices of registration stars. Therefore, an average correction from a combination of several star pairs was selected for Charon centroid calibrations." From this statement we infer that NOS93's error in the systematic correction to fitted centers was roughly 3 milliarcsec.

In this work, fits of the model PSF to synthetic "Pluto-Charon" images implied no systematic correction. Any other result would have been surprising, since the PSF was itself constructed from the field stars. There may still be an unmodeled systematic effect, if Pluto or Charon differed significantly from the mean PSF determined from the stellar images. One such difference is the angular diameter of Pluto, which at 29.4 AU is 0.11 arcsec. For our best images, which have a FWHM of 0.91 arcsec, we can apply the results of Jones *et al.* (1988), who find that Pluto's angular diameter increases the FWHM by 0.5%. The telescope tracked at Pluto rates, during which time the stars' centers move 0.02 arcsec on the detector.

We placed an upper limit on the systematic correction to the center-finding algorithm by fitting Pluto and Charon again, with a different model PSF. The nominal PSF was described in Section 2.3.1. The second PSF was dominated by star 206, and was constructed using backgrounds derived from a sky annulus. We found, as did NOS93, that the Pluto positions were relatively insensitive to changes in the PSF. Pluto centers changed less than 3 milliarcsec. Charon centers changed by 25 milliarcsec for the February 28 data, and by 5-7 milliarcsec for the remaining nights. If the second PSF

represented the range of reasonable deviation of PSFs from the nominal, then these changes provided the estimate for the systematic error inherent in the PSF fitting.

The semimajor axes of this work and NOS93 differed by only 0.4% and the inclinations by 1.6°. This agreement was probably not a coincidental cancellation of errors in the image scale and the center-finding algorithms; as evident in Table 2.3, we found the image scale to much better than this accuracy. This implies that the systematic errors in the Pluto-Charon separations are probably less than 0.4% of the semimajor axis, or 4 milliarcsec. The difference in the mass ratio cannot be explained by a difference in Charon's orbit because (i) the two studies find similar orbits; and (ii) both studies find that leaving out the Charon centers increases the formal error, but does not change the mass ratio significantly. Since our tests indicate that Pluto's center is much less sensitive than the separation to changes in the PSF, we believe that the difference in the mass ratio is not due to systematic errors in PSF fitting.

We next consider the effects that stellar aberration, refraction, changes in the tangent point, precession, and nutation have on our registration (Section 2.3.2). Precession and nutation are completely removed by defining ξ and η with respect to the equator and equinox of J2000. NOS93 corrected for stellar aberration explicitly, and had no need to correct for refraction. In our work, the registration of exposures implicitly accounted for the linear terms of differential refraction (from the variation in airmass over the field), changes in the tangent point, and aberration. The remaining higher-order terms were less than a milliarcsec. The variation of refractivity with color was important only for star 206, whose position was refracted by about 10 milliarcsec relative to the other stars between the minimum and maximum observed zenith distances. The remaining objects had similar colors, and so their relative positions were not shifted significantly by the variation of refraction with wavelength. In particular, the color of Pluto and Charon over

a rotation did not vary enough to significantly change their positions relative to the other stars.

The scatter of the stars' transformed positions provided an estimate of the accuracy of the registration (Section 2.3.2). Fig. 2.8 shows a plot of this scatter (σ_{total}) as a function of the mean of the formal error assigned by Eq. 2.1 (σ_{assign}). Assuming Eq. 2.1 assigned appropriate relative weights, the error introduced by the registration (σ_{reg}) and the ratio of the true errors to the assigned errors (f) were estimated from σ_{total} and σ_{assign}:

$$\sigma_{total}^2 = \sigma_{reg}^2 + f^2\sigma_{assign}^2 \tag{2.8}$$

The best-fit solution (indicated by the curve in Fig. 2.8) implies $\sigma_{reg} \approx 2.5$ milliarcsec and $f \approx 1.3$.

The concept of "registration error" had to be modified for the NOS93 observations. In this work, we register the frames to find the positions of Pluto and Charon relative to the field stars. Since there was only one field star present in the NOS93 observations, the equivalent measurement is the angular distance between the field star and Pluto or Charon. The random error introduced was the error in the star's position, or 2 milliarcsec. NOS93 assumed that the scale is constant between exposures, and they quoted a stability in the scale of 5 parts in 10^5. Therefore, the systematic errors due to changes in scale with time were less than 0.1 milliarcsec. A more crucial assumption is that the scale in row or line (S_y) equals that in column or pixel (S_x). NOS93 adopted a scale ratio (S_y/S_x) of 1.000 $\pm$ 0.002. We evaluated the bounds on the systematic errors implied by the error on the scale ratio; we calculated the Pluto-star separation from Table 4 of NOS93 twice, once assuming $S_y/S_x = 1.000$ and again with $S_y/S_x = 1.002$. The second set of separations was multiplied by an overall scale change to minimize the difference between the two sets of separations. The remaining difference is 3 - 46 milliarcsec, with a mean of 28 milliarcsec.

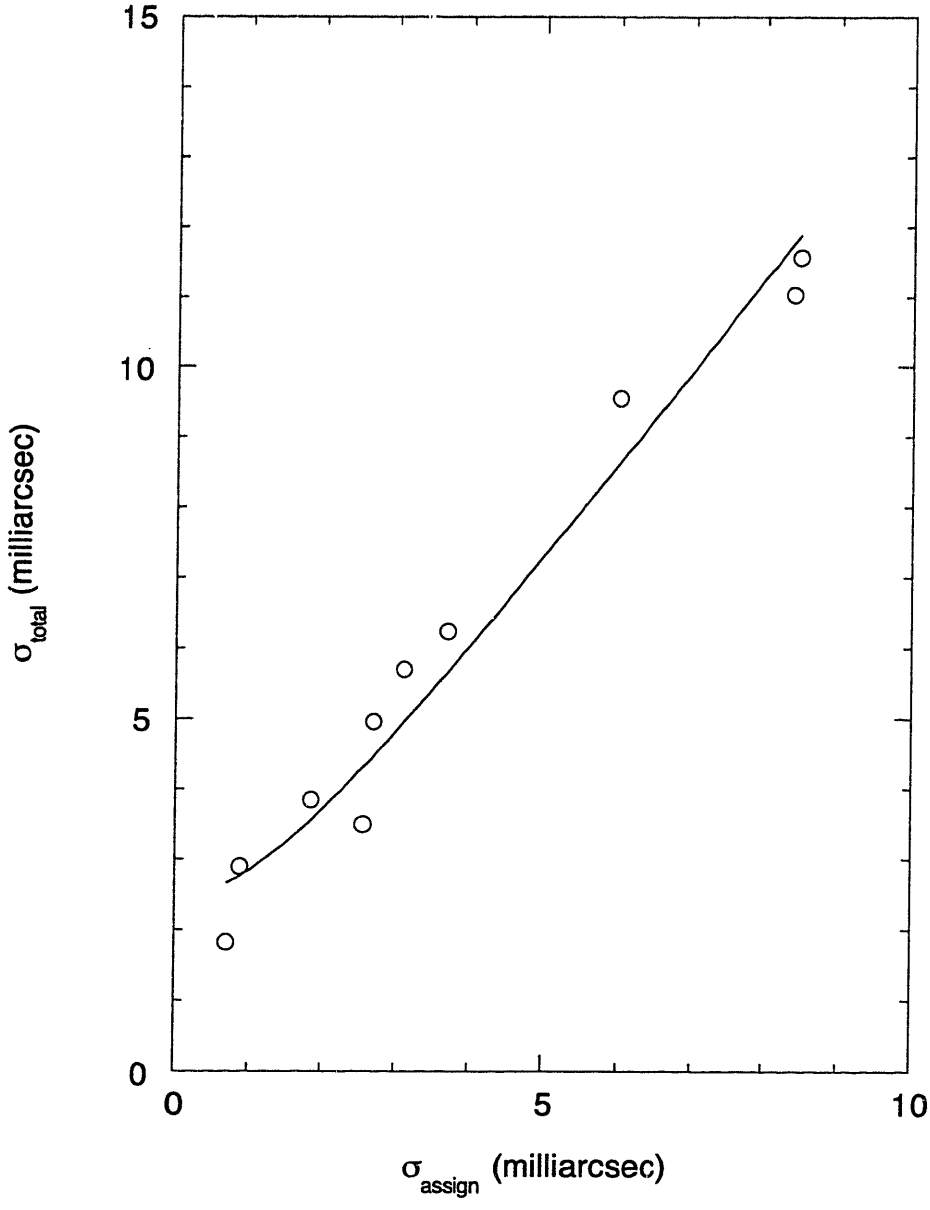

Figure 2.8. Residuals in the star positions. For each exposure, a linear transformation of centers was found to minimize the scatter of each stars' transformed position. The scatter is shown as a function of the formal error. The curve is the best fit to $\sigma_{total}^2 = \sigma_{reg}^2 + f^2 \sigma_{assign}^2$, demonstrating that the random error introduced by the registration is about 2.5 milliarcsec.

Therefore, the systematic error in NOS93's calculation of the Pluto-star separation is less than 46 milliarcsec. This is a very loose bound on the systematic error, and could account for the difference in the measurements of q. However, NOS93 performed one fit with S_y/S_x as a free parameter, and found that q increased by only 1.1 σ.

NOS93 have up to 89 milliarcsec of field distortion, mainly from the reimaging optics. They determined the field distortion from 5 overlapping exposures of an open cluster. Their maximum error in the field distortion at the locations of Pluto is 2 milliarcsec.

We expected the field distortion for the UH 2.2-m to be insignificant. The back-illuminated CCD is mounted in such a way that it is mechanically supported, which should eliminate the "potato chip" warping that was considered by NOS93 (Gerard Luppino, personal communication). In direct imaging mode, the only optical elements are the primary and secondary mirrors, the filter, and the dewar window. Ray-tracing programs for the 2 2-m optics predicted submilliarcsec field distortions for a range of focus positions (Richard Wainscoat, personal communication).

Although our field distortion is expected to be negligible, we need to place observational limits on this. We have five nights of Midas moving from one corner of the field to the opposite corner, which we used to find an image scale and orientation (Section 4). We use the differences between the observed and predicted Midas centers to fit for a field distortion. As the centers follow essentially one path across the field, we can fit for field distortions only along that path. The residual distance (Δd) is the difference between the observed distance (d) and the predicted distance. The residuals were fit with a third order radial function (Eichhorn 1974, Section 2.3.7):

$$\Delta d = p_1 d + p_2 d^2 + p_3 d^3 \qquad (2.9)$$

The results of the fit are shown in Fig. 2.7. There is no apparent field distortion, but we can place only a relatively loose bound of ~20 milliarcsec.

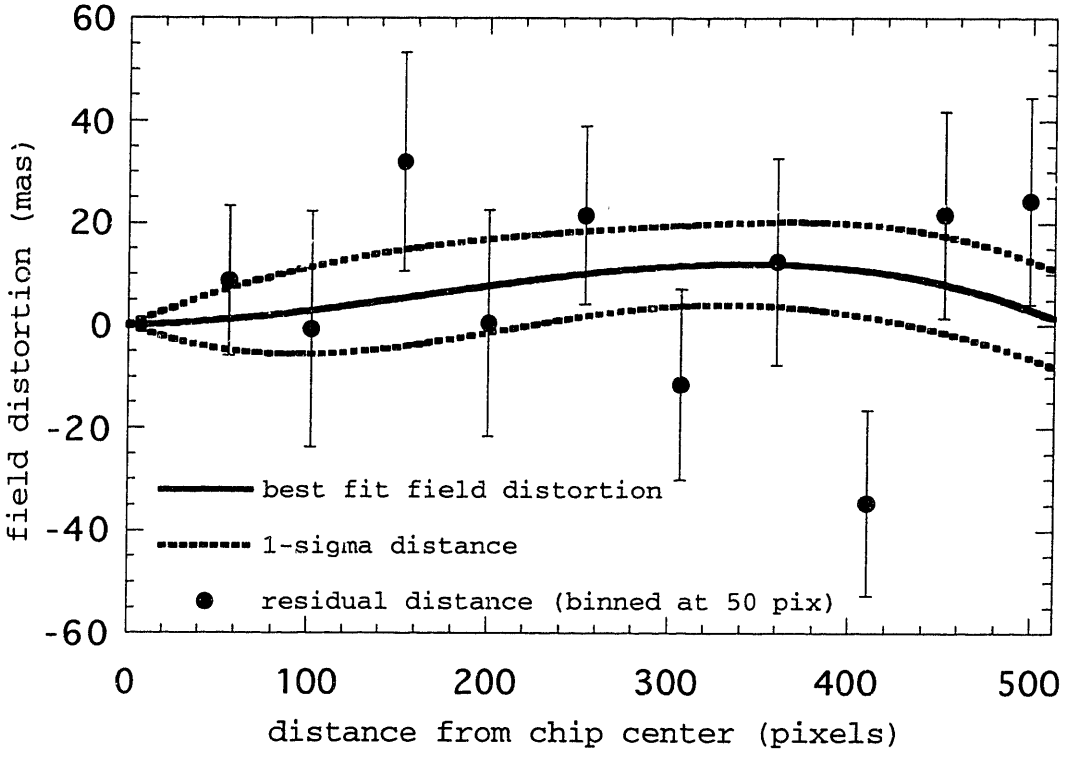

Figure 2.9. Field distortion from Midas observations. The 1-s limit of the fit to the field distortion is observed to be less than 20 milliarcsec.

Other assumptions in the model led to small systematic errors. The correction from the observed center of light of Pluto to the desired center of disk depends on the albedo distribution assumed for Pluto. The size of the center-of-light offset is 4 milliarcsec; this serves as a reasonable bound on the uncertainty in position introduced by the model-dependent nature of the albedo maps. Uncertainties in the starting times of the exposures corresponded to errors of 0.01 milliarcsec. Errors in the ephemeris during one week of observation can be simply treated as an offset. The mutual events constrain the

eccentricity of Charon's orbit only if the longitude of periapse is not along the line of sight. If it is, the eccentricity could be as high as 0.01, which would introduce a systematic error of 5 milliarcsec.

CHAPTER 3
OCCULTATIONS BY SMALL-PLANET ATMOSPHERES*

3.1 INTRODUCTION

The definitive detection of Pluto's atmosphere occurred on 1988 June 9, when starlight dimmed gradually as it was occulted by Pluto (Fig. 3.1). The upper portion of the occultation light curve has the shape characteristic of an occultation by an isothermal atmosphere, but just below half light is a kink where the light curve becomes steeper. Previous analysis of this occultation assumed an isothermal atmosphere that was clear above the kink, while the lower portion has been explained by an absorbing haze layer (Elliot *et al.* 1989) or a steep thermal gradient (Eshleman 1989; Hubbard *et al.* 1990).

Calculations of radiative heating and cooling by methane predict the region above the drop should be isothermal (Hubbard *et al.* 1990; Yelle and Lunine 1989). The detection of, or limits on, a thermal gradient in this region would provide a test of this prediction. To make such a detection, we needed a light-curve model for a non-isothermal atmosphere. Goldsmith (1963) derived a light-curve model for an atmosphere with a linear thermal profile. Unfortunately, this model is not valid for Pluto because it assumes that the scale height is much smaller than the radius of the region probed. In this "large-planet" limit, the following are ignored: (i) variable gravity; (ii) focusing of the starlight in the plane perpendicular to the direction of propagation; and (iii) variation of the radius during the occultation compared with the radius itself. These effects are of the same order as the effects of the thermal gradient we were trying to detect. This requires us to derive a model that includes a thermal gradient and all the small-planet effects.

---

* Chapter 3 and Appendix I are exerpted from the paper Elliot, J. L., and L. A. Young 1992. Analysis of stellar occultation data for planetary atmospheres. I. Model fitting, with application to Pluto. Astron. J. 103, 991-1015.

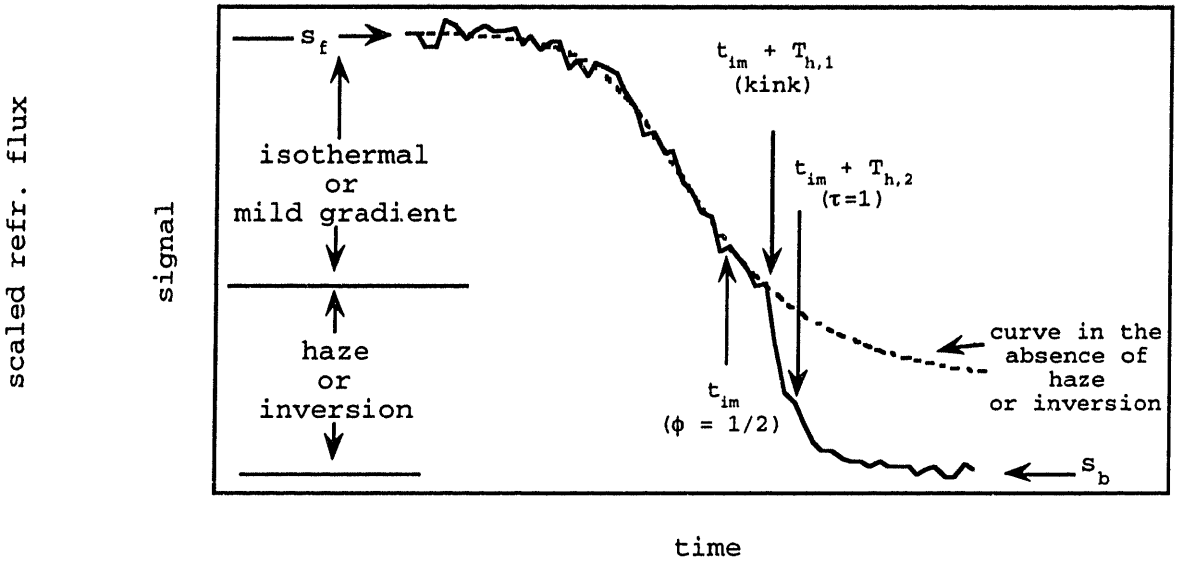

Figure 3.1. Anatomy of Pluto's stellar occultation light curve. Signal level is plotted versus time for the immersion portion of an occultation light curve, from the start of the occultation to the midtime. At the start of the occultation, the flux is at its unocculted level, s_f, and drops to the background level, s_b, at mid-occultation. The upper portion has the shape characteristic of an atmosphere with at most a mild thermal gradient. If the atmosphere did not experience some sort of transition, the lightcurve would follow the dashed line. At the time $t = t_{im} + T_{h,1}$, the Pluto occultation has a sharp drop. The times when the stellar flux has dropped to half its unocculted value (t_{im} and t_{em}) correspond to the "half-light" radius on the planet. The time corresponding to optical depth = 1 of an assumed haze is also indicated.

Analyses of occultation light curves by atmospheres rely on the equations relating the observed flux to the refractivity profile. In numerical inversions of the light curve, the refractivity profile is obtained directly from the data, and is then related to the thermal profile by assuming hydrostatic equilibrium. In least-squares fitting, one specifies the functional form of the temperature and local scale height; hydrostatic equilibrium is again assumed, and the flux-refractivity relations are used to produce a synthetic light curve. I will first present the equations for the flux in terms of arbitrary functions of temperature, local scale height, and linear extinction coefficient. These equations are the starting point

for generating any synthetic stellar occultation light curve (Baum and Code 1953; Elliot *et al.* 1989; Elliot and Young 1992; Goldsmith 1963).

I apply these general equations to the specific problem of a small planet with a haze layer and thermal and compositional gradients. This leads to equations written in terms of the physical characteristics of the atmosphere (such as the refractivity and linear absorption coefficient) and the occultation geometry (such as the observer-body distance or the observer's position in the shadow as a function of time).

To perform least-squares fitting, one would like a set of parameters that have low correlations and whose relationship to the light curve is easily visualized. I describe one such set, and how to convert between the "atmospheric" parameters (used for deriving the light curve) and the "data" parameters (used for least-squares fitting).

3.2 GENERAL FLUX EQUATION

Fig. 3.2 illustrates light from a star being occulted by a planetary atmosphere. Monochromatic, parallel light rays are incident on a planetary atmosphere from the left and then encounter a spherically symmetric planet. The center of the occulting planet's shadow lies on the line that is parallel to the incoming light rays and passes through the center of the planet. The "observer's plane" is the plane that contains the observer and is perpendicular to the incident light rays. The observer's position is described by the observer-planet distance, D, and the distance from the center of the shadow in the observer's plane, ρ.

A light ray with closest approach distance r to the center of the planet is bent by the atmosphere and then deviates from its original path by an angle $\theta(r)$, remaining in the plane containing the center of the planet and the original path of the ray. This ray

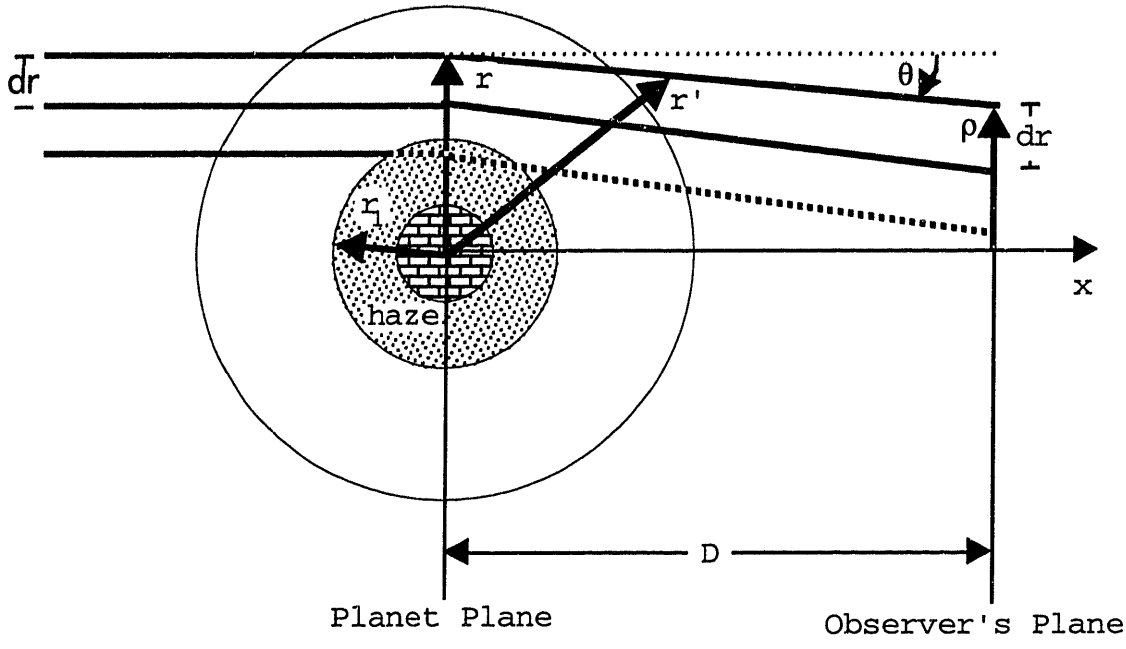

Figure 3.2. Occultation by a planetary atmosphere. Starlight encounters a planetary atmosphere and is bent by the gradient of refractivity in the atmosphere. Since the refraction increases exponentially with depth in the atmosphere, two neighboring rays separate, causing the star to dim as seen by a distant observer. Another dimming effect is atmospheric extinction, which exists in our model only for radii less than r_1.

intersects the planet plane at a radius r and the observer plane at a radius ρ. The refraction angle is negative, since rays bend toward the center of the planet, and we assume it is a small angle for the purpose of trigonometric approximations. If there is enough bending, or if the observer is far enough from the planet, the ray will arrive at the observer's plane on the far side of the shadow center. The light from this ray is called the far-limb contribution to the flux, and it is generally much less than the near-limb contribution. Since ρ would never be negative, we have the following relation between the intersection points of a light ray in the two planes of interest:

$$\rho(r) = |r + D\theta(r)| \tag{3.1}$$

The stellar flux will be changed by three effects upon passing through the planetary atmosphere: (i) differential bending of the light rays; (ii) absorption by the atmosphere; and (iii) partial focusing of the light by the curvature of the planetary limb in the plane perpendicular to the path of the ray. An initial bundle of light rays that has a width dr before interaction with the planet will be expanded into a width $d\rho$ in the observer's plane, due to differential bending. This decreases the stellar flux by the factor $|dr/d\rho|$. Atmospheric absorption diminishes the flux by a factor $\exp[-\tau_{obs}(r)]$, where $\tau_{obs}(r)$ is the observed optical depth along the path of the ray. Finally, the focusing by the planetary limb increases the flux by the ratio of the circumferences of the "circles of light" of radius r and ρ. Hence, the flux in the observer's plane, $\zeta(r)$, is simply written as a product of three factors:

$$\zeta(r) = \frac{r}{\rho(r)}\left|\frac{dr}{d\rho(r)}\right|\exp\left[-\tau_{obs}(r)\right] = \frac{\exp\left[-\tau_{obs}(r)\right]}{\left|1 + D\frac{\theta(r)}{r}\right|\left|1 + D\frac{d\theta(r)}{dr}\right|} \tag{3.2}$$

Eq. (3.2) describes the contribution from a single limb. To find the normalized stellar flux, $\phi(\rho)$, in the observer's plane, we sum the single limb flux, $\zeta(r)$, for all values of r that would arrive at ρ. We assume the only contribution to the flux is from the near limb, so $\phi[\rho(r)] = \zeta(r)$. This implies there is no ray crossing, and we can write Eqs. (3.1) and (3.2) without taking absolute values. With this assumption, the observed normalized flux is:

$$\phi(\rho) = \frac{\exp\left[-\tau_{obs}(r)\right]}{\left(1 + D\frac{\theta(r)}{r}\right)\left(1 + D\frac{d\theta(r)}{dr}\right)} \tag{3.3}$$

The flux as defined is normalized so that it equals one in the absence of an occultation. The normalized flux is multiplied by the signal that would have been received by the unocculted star, $s_*(t)$, then added to the background signal, $s_b(t)$, that

includes signal from the planet and sky. The signal is integrated over a short time interval. If the i^{th} integration is centered on a time t_i, and has a length Δt_i, then the recorded signal for the i^{th} integration, s_i, can be expressed as:

$$s_i = \int_{t_i-\Delta t/2}^{t_i+\Delta t/2} s_*(t)\phi[\rho(t)] + s_b(t)dt \tag{3.4}$$

The refraction angle and observed optical depth depend on the refractivity, ν, and linear absorption coefficient, κ. Since our planet is spherically symmetric, its refractivity and linear absorption coefficient are functions only of the distance from the center of the planet r', (Fig. 3.2). To integrate refraction and absorption along the path of the ray, we define an x coordinate that lies along the path of the ray and has its origin at the closest approach of the ray to the center of the planet. The deviation of the ray from its original path within the atmosphere is small enough to be neglected, so that we have the following relation among x, r, and r':

$$r'^2 = r^2 + x^2 \tag{3.5}$$

The refraction angle is given by the r derivative of the integral of the refractivity along the path of the ray.

$$\theta(r) = \frac{d}{dr}\int_{-\infty}^{+\infty} \nu[r'(x,r)]dx = \int_{-\infty}^{+\infty} \frac{\partial \nu[r'(x,r)]}{\partial r}dx = \int_{-\infty}^{+\infty} \frac{r}{r'}\frac{d\nu(r')}{dr'}dx \tag{3.6}$$

To find the refractivity, we first find the pressure, p. In a spherically symmetric atmosphere, the pressure is related to the number density, n, through hydrostatic equilibrium

$$\frac{dp(r)}{dr} = -n(r)\mu(r)m_{amu}g(r) \tag{3.7}$$

and the ideal gas law

$$p(r) = n(r)kT(r) \tag{3.8}$$

where k is Boltzmann's constant, and m_{amu} is the mass of one atomic mass unit.

The scale height, H, is the height over which the pressure drops by a factor of e:

$$H(r) \equiv -\left(\frac{1}{p}\frac{dp(r)}{dr}\right)^{-1} = \frac{kT(r)}{g(r)\mu(r)m_{amu}} \tag{3.9}$$

We assume the local acceleration is due to gravity alone:

$$g(r) = \frac{GM_p}{r^2} \tag{3.10}$$

where G is the universal gravitational constant and M_p is the mass of the planet. We define the quantity $\lambda(r)$ as the ratio of the magnitude of the gravitational potential energy (referred to 0 at $r = \infty$) to kT:

$$\lambda(r) \equiv \frac{GM_p\mu(r)m_{amu}}{kT(r)r} = \frac{r}{H(r)} \tag{3.11}$$

The scale height can be integrated from a reference radius, r_0, and a reference pressure, p_0, to get the pressure as a function of radius.

$$p(r) = p_0 \exp\left[-\int_{r_0}^{r} \frac{du}{H(u)}\right] \tag{3.12}$$

The refractivity is proportional to the number density, so

$$\frac{\nu(r)}{\nu_0} = \frac{n(r)}{n_0} = \frac{T_0}{T(r)}\exp\left[-\int_{r_0}^{r} \frac{du}{H(u)}\right] \tag{3.13}$$

and

$$\frac{dv(r)}{dr} = -\left(\frac{1}{T(r)}\frac{dT(r)}{dr} + \frac{1}{H(r)}\right)v(r) \tag{3.14}$$

The observed optical depth is the integral of the linear absorption coefficient along the ray:

$$\tau_{obs}(r) = \int_{-\infty}^{+\infty} \kappa[r'(x,r)]dx \tag{3.15}$$

This completes the equations for calculating the observed stellar flux from specified temperature, molecular weight, and absorption profiles.

3.3 MILD THERMAL GRADIENT WITH HAZE

We chose a power law for the functional form of temperature and molecular weight, with indices $-a$ and b, respectively. This avoids negative values of the temperature or molecular weight, and shares the same functional form as the gravitational acceleration. The signs of the indices were chosen so that the power indices of gravity, temperature, and molecular weight appear with the same sign in the equation for the scale height. The mean molecular weight, $\mu(r)$, is:

$$\mu(r) = \mu_0\left(\frac{r}{r_0}\right)^{-a} \tag{3.16}$$

where μ_0 is the reference molecular weight, $\mu(r_0)$. Likewise, the reference temperature is T_0, and the temperature is:

$$T(r) = T_0\left(\frac{r}{r_0}\right)^{b} \tag{3.17}$$

Three parameters define the haze layer: (i) r_1, the radius of the upper boundary of the haze layer; (ii) κ_1, the linear absorption coefficient of the haze at r_1; and (iii) $H_{\tau 1}$, the scale height of the haze at r_1. Allowing the scale height of the haze to have the same radial dependence as gravity, we have the following equation for the linear absorption coefficient, $\kappa(r)$, of the haze:

$$\kappa(r) = \begin{cases} 0, & r > r_1 \\ \kappa_1 \exp\left[-\dfrac{r - r_1}{H_{\tau 1}(r/r_1)}\right], & r \le r_1 \end{cases} \tag{3.18}$$

We can now insert the equations for T and μ into the general equations for the scale-height, Eq. (3.9). We can consolidate most of the leading constants by introducing the quantity λ_0 as the value of $\lambda(r)$ at the reference radius

$$\lambda_0 \equiv \lambda(r_0) = \frac{GM_p \mu_0 m_{amu}}{kT_0 r_0} \tag{3.19}$$

so that the energy ratio is now

$$\lambda(r) = \lambda_0 \left(\frac{r}{r_0}\right)^{-(1+a+b)} \tag{3.20}$$

In terms of these, the scale height is:

$$H(r) = \frac{r_0}{\lambda_0}\left(\frac{r}{r_0}\right)^{2+a+b} \tag{3.21}$$

Hence, the refractivity, by integration of Eq. (3.9) is:

$$\nu(r) = \nu_0 \left(\frac{r}{r_0}\right)^{-b} \exp\left[\frac{\lambda(r) - \lambda_0}{1 + a + b}\right] \tag{3.22}$$

Next we find the refraction angle for a light ray passing through the planetary atmosphere. We take the derivative of the refractivity required by Eq. (3.6) and express the result in terms of the energy ratios, $\lambda(r)$ and $\lambda(r')$:

$$\theta(r) = -\nu(r)\int_{-\infty}^{\infty}\left(\frac{r}{r_0}\right)^{b+2}\exp\left[\frac{\lambda(r')-\lambda(r)}{1+a+b}\right]\frac{\lambda(r')+b}{r}dx \tag{3.23}$$

Our approach to the small-planet problem is to find power series approximations in terms of the parameter $\delta \equiv 1/\lambda(r)$.

$$\delta(r) \equiv \frac{1}{\lambda(r)} = \frac{H(r)}{r} \tag{3.24}$$

We note that δ becomes small in the large-planet limit, but it cannot be set to zero whenever it occurs. Hence we have adopted the convention of using δ in expressions where it is added to larger terms and can be set to zero in the large planet limit. However, we use λs and Hs in those parts of the expression where these quantities should be retained in the large planet limit.

After performing this integral (Appendix I), we find that $\theta(r)$ can be expressed as

$$\theta(r) = -\sqrt{2\pi\lambda(r)}\nu(r)A(\delta,a,b) \tag{3.25}$$

where $A(\delta, a, b)$ is a power series in δ. $A(\delta, a, b) \rightarrow 1$ as $\delta \rightarrow 0$, so that we can set $A(\delta, a, b) = 1$ for the large planet case.

$$A(\delta,a,b) = 1 + \left(-\frac{3+a-3b}{8}\right)\delta + \ldots \tag{3.26}$$

We also express the derivative of the refraction angle by using a power series, $B(\delta, a, b)$, that equals one in the limit $\delta \rightarrow 0$.

$$\frac{d\theta(r)}{dr} = \sqrt{2\pi\lambda^3(r)}\frac{\nu(r)}{r}B(\delta,a,b) \tag{3.27}$$

where

$$B(\delta,a,b) = 1 + \left(\frac{1+3a+15b}{8}\right)\delta + \ldots \tag{3.28}$$

In the large planet limit, $D\ d\theta/dr$ is of order one during the steepest part of the occultation. Writing $d\theta/dt$ in terms of θ,

$$D\frac{d\theta(r)}{dr} = -\frac{D\theta(r)}{r}\lambda(r)\frac{B(\delta,a,b)}{A(\delta,a,b)} \tag{3.29}$$

we see that the term $D\theta/r$ is smaller than $D\ d\theta/dr$ by the small-planet parameter, δ. This is why the focusing factor can be dropped from the flux equation in the large-planet limit.

The observed optical depth can now be found by integrating the linear extinction coefficient along the path of the light ray. The integration is performed only over the region where the haze exists. The x coordinate of the haze onset, x_1, is

$$x_1 \equiv x(r_1) = \sqrt{r_1^2 - r^2} \tag{3.30}$$

Combining Eqs. (3.15) and (3.18), we obtain the following expression for $\tau_{obs}(r)$:

$$\tau_{obs}(r) = \int_{-x_1}^{x_1} \kappa_1 \exp\left[-\frac{r' - r_1}{H_{\tau 1}(r'/r_1)}\right] dx \tag{3.31}$$

Again, the result contains a power series in a parameter that goes to zero in the large-planet limit.

$$\delta_\tau \equiv \frac{H_\tau(r)}{r} = \frac{H_{\tau 1} r}{r_1^2} \tag{3.32}$$

The result of the integration (Appendix I) is

$$\tau_{obs}(r) = \begin{cases} 0, & r > r_1 \\ \kappa(r)\dfrac{r}{r_1}\sqrt{2\pi H_{\tau 1} r}\,\mathrm{erf}\left[\dfrac{r_1}{r}\sqrt{\dfrac{r_1^2 - r^2}{2H_{\tau 1} r}}\right] C(\delta_\tau), & r \le r_1 \end{cases} \tag{3.33}$$

where C is a power series in δ_τ:

$$C(\delta_\tau) = 1 + \frac{9}{8}\delta_\tau + \ldots \tag{3.34}$$

To calculate the stellar flux in terms of ρ we first find $r(\rho)$. The radii r and ρ are related by Eq. (3.1), and we solve this equation for $r(\rho)$ with Newton's method – a straight-forward process, since the function is monotonic. To find the flux for a given time, $\phi(t)$, we find the observer's shadow radius as a function of time, $\rho(t)$. For a straight chord through the shadow that travels with a velocity v and has a minimum shadow radius of ρ_{min} at the midtime of the event, t_{mid}, the shadow radius is:

$$\rho(t) = \sqrt{\rho_{min}^2 + v^2 (t - t_{min})^2} \tag{3.35}$$

The velocity perpendicular to the limb, $v_\perp$, is the derivative of $\rho(t)$:

$$v_\perp(\rho) \equiv \frac{d\rho}{dt} = v\frac{\sqrt{\rho^2 - \rho_{\min}^2}}{\rho} \tag{3.36}$$

The final step before calculating a signal is to specify the signal levels and the integration interval called for in Eq. (3.4). For the KAO event, we used a constant star

signal level and even integration intervals. We used a linear background that was defined at t_{av}, the midtime of the data set (which is not necessarily the midtime of the occultation event):

$$s_b(t) = s_b + s'_b(t - t_{av}) \tag{3.37}$$

We can now calculate a light curve in terms of a fundamental set of parameters, which we shall call the "atmospheric parameter set," summarized in the first column of Table 3.1. These parameters fall into four groups: (i) signal levels; (ii) geometry and data recording; (iii) clear atmosphere; and (iv) haze.

The large-planet, isothermal equations (Baum and Code 1953) describe a family of light curves that have the same shape, and are scaled in time and signal. The signal is scaled by s_* and offset by s_b. The time is scaled by the time interval $H/v_\perp$ (which is constant throughout the occultation) and offset by the time of half-light. When fitting with this model, it is simpler to fit for these scaling parameters, rather than the physically more meaningful t_{mid}, r_h, and ν_h.

Even though our model does not preserve this scaling property, we also find it useful to describe the model light curve in terms of times and signal levels. These "data" parameters are easier to visualize, and tend to be less strongly correlated than the "atmospheric" parameters. We have formulated a set of data parameters, illustrated in Fig. 3.1 and summarized in Table 3.1. The parameters fall into four categories: (i) signal levels; (ii) times of events on the light curve; (iii) time scales of the refractive and extinction occultations; and (iv) parameters that affect the shoulders of the light curve.

To avoid a relatively large correlation between s_* and s_b, we use full-scale level, s_f:

$$s_f = s_* + s_b \tag{3.38}$$

To first order, a lightcurve generated from an atmosphere with a thermal gradient looks like an isothermal atmosphere with a slightly different scale height. This was first described by Goldsmith (1963). (Note that he found an incorrect correction fraction of (3/2 dH / dr), rather than (5/2 dH / dr), as discussed in Elliot and Young (1992), Section 8). We define the equivalent isothermal scale height, H_{iso}, as the scale height of an isothermal atmosphere that would produce a light curve with the same slope at half light as the non-isothermal atmosphere. We will use H_{iso} for fitting the light curve, since b is less correlated with H_{iso} than it is with the true scale height at half light, $H_h \equiv H(r_h)$.

Table 3.1. Parameters of the occultation.

Atmospheric Parameters		Data Parameters	
	Signal Levels		
s_b	background level	s_b	background level
s_b'	background slope	s_b'	background slope
s_*	star level	s_f	full-scale level
	Geometry and Data Recording		
D	planet-observer distance	D	planet-observer distance
υ	shadow velocity	υ	shadow velocity
Δt	integration time	Δt	integration time
ρ_{min}	minimum shadow radius	T_{min}	minimum shadow radius
t_{mid}	midtime		
	Clear Atmosphere		
a	exponent for molecular wt.	a	exponent for molecular wt.
b	exponent for temperature	b	exponent for temperature
r_0	reference radius	T_{Hiso}	refraction scale interval
λ_0	reference energy ratio	t_{im}	immersion half-light time
ν_0	reference refractivity	t_{em}	emersion half-light time
	Haze		
$H_{\tau 1}$	haze scale height	$T_{H\tau 2}$	haze scale interval
r_1	top of haze	$T_{h,2}$	$\tau = 1$ interval
κ_1	linear absorption coefficient	$T_{h,1}$	haze onset interval

The slope of the refractive portion of the occultation is $d\phi_{ref}/dt = (d\phi_{ref}/d\rho)\,(d\rho/dt)$. The first term, dr/dt, is the velocity of the planet perpendicular to the limb, so we define the perpendicular velocity at half light as $v_{\perp,h}$:

$$\left.\frac{d\rho}{dt}\right|_{r=r_h} \equiv v_{\perp,h} = v\frac{\sqrt{\rho_h^2 - \rho_{\min}^2}}{\rho_h} \tag{3.39}$$

and the other factor in the derivative is

$$\left.\frac{d\phi_{ref}}{d\rho}\right|_{r=r_h} = \frac{1}{8H_h}\left[1+\frac{1+3a+5b}{2}\delta_h + O(\delta_h^2)\right] \tag{3.40}$$

The relationship between H_h and H_{iso} is obtained by setting $a = b = 0$ in Eq. (3.40) for the right hand side.

$$\frac{1}{8H_h}\left[1+\frac{1+3a+5b}{2}\delta_h+\ldots\right] = \frac{1}{8H_{iso}}\left[1+\frac{1}{2}\delta_h+\ldots\right] \tag{3.41}$$

so that

$$H_{iso} = \frac{H_h}{1+\frac{3a+5b}{2}\delta_h+\ldots} \tag{3.42}$$

This equation is more useful as a relationship between the energy ratios:

$$\lambda_h \equiv \lambda(r_h) = \frac{r_h}{H_{iso}} - \frac{3a+5b}{2} + O(\delta_h)^2 \tag{3.43}$$

For fitting, we convert H_{iso} into a time interval. According to Eq. (3.40), this is the time it takes the flux to drop by about 1/8.

$$T_{iso} = H_{iso}/v_{\perp,h} \tag{3.44}$$

The timing offset is defined by the immersion and emersion half-light times, t_{im} and t_{em}. We can solve Eq. (3.35) for ρ_h, but finding r_h is more complicated. This is a special case of finding the radius r_f corresponding to a given flux level f. Using only the refraction terms, the flux at the radius r_f is:

$$f = \left[\left(1+\frac{D\theta_f}{r_f}\right)\left(1-\frac{D\theta_f}{r_f}\frac{\lambda_f B_f}{A_f}\right)\right]^{-1} \tag{3.45}$$

where $\theta_f = \theta(r_f)$, $\delta_f = \delta(r_f)$, $A_f = A(\delta_f, a, b)$, $B_f = B(\delta_f, a, b)$, and $\lambda_f = \lambda(r_f)$. If r_0, λ_0, and ν_0 are specified at some arbitrary reference radius, Eq. (3.45) can be solved numerically for r_f, using Eq. (3.20), (3.24), and (3.25) to find λ_f, δ_f, and θ_f. Conversely, if r_f and λ_f are specified, this equation is quadratic in $D\,\theta_f/r_f$. The positive root is taken, so that the large-planet limit for the case of $f = 1/2$ is $D\,\theta_h/r_h = -\delta_h$. The solution is:

$$D\theta_f = \frac{r_f}{2}\left(\frac{A_f}{\lambda_f B_f} - 1 + \sqrt{1 + \left(2 - \frac{4}{f}\right)\frac{A_f}{\lambda_f B_f} + \left(\frac{A_f}{\lambda_f B_f}\right)^2}\right) \tag{3.46}$$

We use this to find r_h and λ_h by successive substitution, given ρ_h and H_{iso}. The initial guess for the half-light radius is the large-planet solution:

$$r_{h(1)} = \rho_h + H_{iso} \tag{3.47}$$

In each succeeding iteration, the energy ratio for the i^{th} iteration, the energy ratio for the i^{th} iteration is found by Eq. (3.43).

$$\lambda_{h(i)} = \frac{r_{h(i)}}{H_{iso}} = \frac{3a + 5b}{2} \tag{3.48}$$

The next guess for the half-light radius is found from the refraction angle and the specified ρ_h, where $D\theta_h$ is given by Eq. (3.46):

$$r_{h(i+1)} = \rho_h - D\theta_h \tag{3.49}$$

The iterations continue until $|r_{h(i+1)} - r_{h(i)}| / r_{h(i)}$ is less than a specified precision. Once the refraction angle at half-light is known, the refractivity at half-light, ν_h, can be calculated using Eq. (3.25).

The time of the sharp drop is specified as a time interval from the half light time. The time of unit optical depth (at which time $\phi = \phi_{ref}/e$) is given as the time interval between

half light and unit optical depth, $T_{h,2}$. These parameters have been given as intervals (rather than specific times) in order to impose symmetry between immersion and emersion. These time intervals are:

$$T_{h,1} = |t(\rho_1) - t(\rho_h)| \tag{3.50}$$

and

$$T_{h,2} = |t(\rho_2) - t(\rho_h)| \tag{3.51}$$

We scale the minimum shadow radius, ρ_{min}, by the velocity. Now all the spatial coordinates are expressed as times or time intervals.

$$T_{min} = \rho_{min} / v. \tag{3.52}$$

Next we define an extinction scale height, $H_{\tau 2}$, at the radius r_2:

$$H_{\tau 2} \equiv H_\tau(r_2) = H_{\tau 1}(r_2/r_1)^2 \tag{3.53}$$

To treat the haze scale height analogously to the pressure scale height, we divide by the half-light perpendicular velocity:

$$T_{H\tau 2} = H_{\tau 2} / v_{\perp,h} \tag{3.54}$$

Substituting r_2 for r and $\delta_{\tau 2}$ for δ_τ in Eq. (3.33) results in the condition for unit optical depth at $r = r_2$:

$$\tau_{obs}(r_2) \equiv 1 = \kappa_1 \frac{r_2}{r_1}\sqrt{2\pi H_{\tau 1} r_2}\ \mathrm{erf}\left[\frac{r_1}{r_2}\sqrt{\frac{r_1^2 - r_2^2}{2H_{\tau 1} r_2}}\right]\exp\left[-\frac{r_2 - r_1}{H_{\tau 1}(r_2 / r_1)}\right]C(\delta_{\tau 2}) \tag{3.55}$$

The preceding completes the prescription for converting between the data parameters and the atmospheric parameters summarized in Table 3.1.

Table 3.2. Best fit parameters to KAO occultation.

Model Parameter	Fit #1 All Data	Fit #2 All Data *b* free
Data Parameters		
background level, s_b (ADU)	633.3 ± 6.8	633.1 ± 6.8
full-scale level, s_f (ADU)	3346.3 ± 5.3	3344.2 ± 6.1
immersion half-light time, t_{im} (s*)	53.89 ± 0.15	53.94 ± 0.17
emersion half-light time, t_{em} (s*)	139.92 ± 0.15	139.88 ± 0.17
refraction scale interval, T_{Hiso} (s)	4.61 ± 0.09	4.71 ± 0.18
exponent for temperature, b	0.0	–0.61 ± 0.87
haze scale interval, $T_{h,1}$ (s)	4.16 ± 0.17	4.11 ± 0.19
haze onset interval, $T_{h,2}$ (s)	7.10 ± 0.25	7.01 ± 0.28
haze reference interval, $T_{H\tau 2}$ (s)	2.27 ± 0.41	2.34 ± 0.44
Atmospheric parameters		
background level, s_b (ADU)	633.3 ± 6.8	633.1 ± 6.8
star level, s_* (ADU)	2713.0 ± 8.7	2711.2 ± 9.1
midtime, t_{mid} (s*)	96.906 ± 0.046	96.907 ± 0.046
reference refractivity, ν_0 (10^{-9})	1.01 ±0.16	0.97 ± 0.17
reference energy ratio, λ_0	21.3 ± 0.69	22.4 ± 1.8
exponent for temperature, b	0.0	–0.61 ± 0.87
transition radius, r_1 (km)	1216 ± 11	1215 ± 11
haze scale height, $H_{\tau 1}$ (km)	29.0 ± 5.2	29.8 ± 5.6
linear absorption coefficient, κ_1 (cm^{-1})	(2.20 ± 0.18) 10^{-8}	(2.22 ± 0.18) 10^{-8}
Fit Information		
degrees of freedom	992	991
sum of squared residuals	374043	373875
rms residual per degree of freedom (ADU)	19.418	19.424

*after 1988 June 9, 10:35:50 UTC

The above model was fit to the KAO observation of the 1988 stellar occultation by Pluto (Elliot and Young 1992). That paper presented several permutations of fixed or free parameters and subsets of the data. Here we summarize the results for two fits (Table 3.2). In Fit #1, the atmosphere is assumed to be isothermal until below the time the star was last detected. In Fit #2, the entire region probed is allowed to have a mild

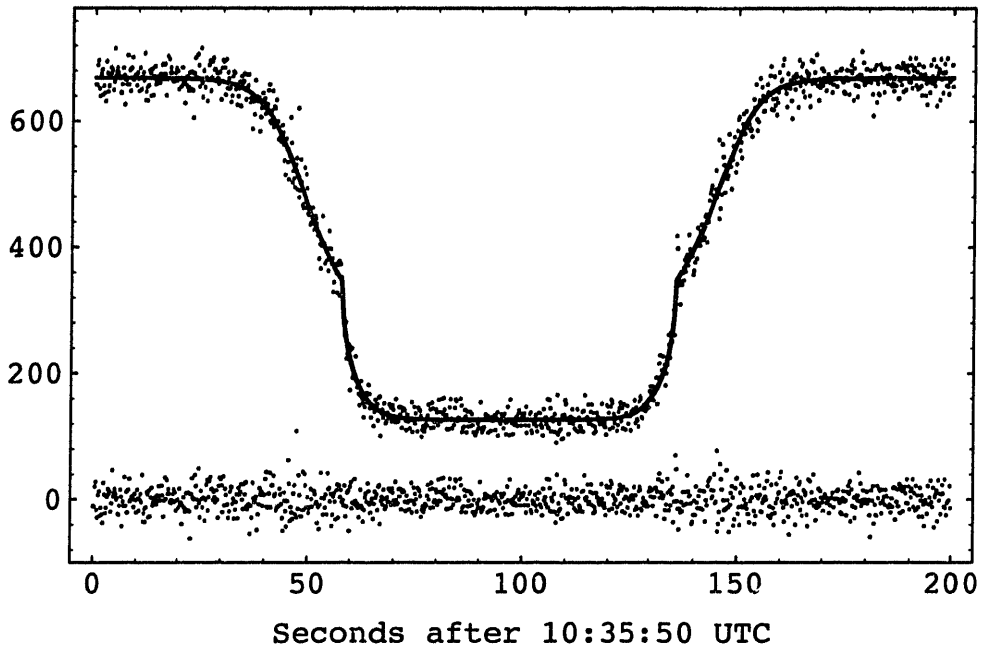

Figure 3.3. Stellar occultation data and model. The stellar-occultation light curve observed with the KAO (Elliot *et al.* 1989) has been plotted as points and the best-fitting model as a line. The residuals from the model fit are the points in the lower part of the figure.

thermal gradient. The results are summarized in Table3.3. In both these fits, a and s_b' were fixed at 0, and T_{min} was fixed at ρ_{min}/υ = 865.69 km / 18.475911 km s^{-1}.

The data, model, and residual are shown in Fig. 3.3. Fig. 3.4 is a close-up of Fig. 3.3 (with the emersion data folded around the midtime), showing the effect of thermal gradients on the shape of the shoulder. We find that the occultation is consistent with an atmosphere that is isothermal above the transition radius. For an N_2 atmosphere, the gradient above the transition radius is –0.049 ± 0.066 K km^{-1}.

3.6 ISOTHERMAL OVERLYING AN INVERSION LAYER

Eshleman (1989), Hubbard *et al.* (1990), and Stansberry *et al.* (1994) all reported purely refractive models that could explain the main features of the KAO lightcurve. Two of these are shown in Fig. 3.5. These models assume an isothermal atmosphere

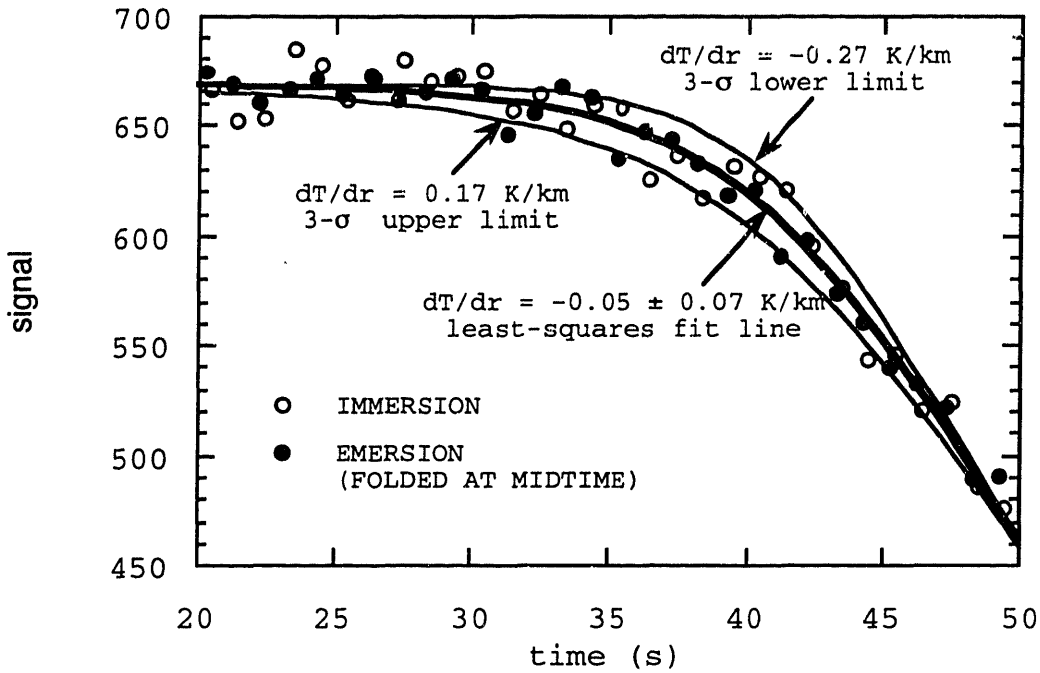

Fig. 3.4. Effect of temperature gradient on the occultation light curve. Shown are three models for the flux; the best fit model and the models with $b = \bar{b} \pm 3\sigma$. The data, plotted as filled or open circles, are one-second averages of the raw data.

above the transition radius, an assumption that is supported by the results of the previous section. The reported gradients range from 8.5 K km^{-1} (Eshleman 1989) to 30 K km^{-1} (Stansberry *et al.* 1994). However, these gradients might not be directly comparable, since the thermal gradient below the transition radius is a function of radius. To put the results on the same footing, we matched the reported thermal profiles with the Bates (1959) analytic profile for the thermosphere (Table 3.3),

$$T(r) = T_\infty\left(1 - \alpha e^{-\beta z}\right) \tag{3.56}$$

where z is the geopotential distance from some reference radius, r_3.

$$z = \frac{r^3 - r_3^3}{3r_3^2} \approx r - r_3 \tag{3.57}$$

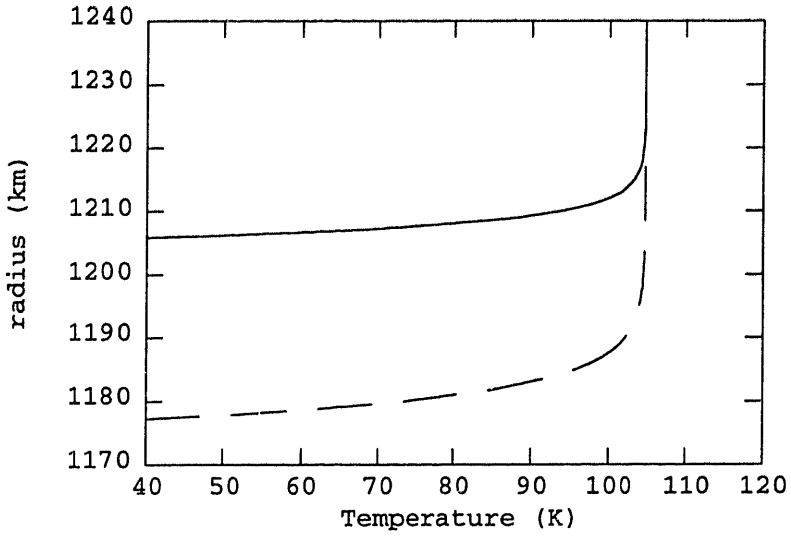

Figure 3.5. Thermal profiles that reproduce the occultation light curve. The upper profile is from Stansberry *et al.* (1994), and the lower curve is from Eshleman (1989). These profiles are described by the parameters in Table 3.3.

The Bates thermal profile is isothermal at high altitudes, then achieves a thermal gradient at lower altitudes. The profile matches that of the methane-thermostat model (Holman 1991; Stansberry *et al.* 1994), and reproduces the "bite" in the light curve (Stansberry *et al.* 1994).

Table 3.3. Parameters for inversion layer.

reference	T_∞	r_3	α	β
Eshleman (1989)	104.7	1178.0	0.5	0.250
Stansberry *et al.* (1994)	106.0	1206.2	0.5	0.565

CHAPTER 4
ATMOSPHERIC METHANE MIXING RATIO

4.1 INTRODUCTION

The temperature of Pluto's atmosphere above 1215 km is near 100 K for an N_2 atmosphere (Elliot and Young 1992; Owen *et al.* 1993). Since the surface temperature lies between 30K (Stern *et al.* 1993) and 60 K (Sykes *et al.* 1987), there must be some source of heating in the atmosphere. Yelle and Lunine (1989) proposed the absorption of sunlight in the 3.3 μm band of CH_4 as the source of heating. In their model, radiative heating by the 3.3-μm band of CH_4 and radiative cooling at the 7.7-μm band of CH_4 will heat the atmosphere to about 100 K, if the atmospheric CH_4 abundance exceeds 0.1%. A detection of the atmospheric CH_4 abundance will test if heating by CH_4 is important in Pluto's atmosphere.

The initial detections of CH_4 on Pluto were attributed to surface frosts (Cruikshank *et al.* 1976). These observations used special filters near the 1.7 μm CH_4 feature to distinguish between the ices of H_2O, NH_3, and CH_4 – constituents that were considered likely under cosmochemical arguments (Lewis 1972). Benner *et al.* (1978) inferred that Pluto must have at least a tenuous CH_4 atmosphere, in equilibrium with this frost, and derived a CH_4 column height of 3 m-A from their 6800 –9000 Å spectrum of Pluto. Further observations confirmed the presence of CH_4 absorptions (Barker *et al.* 1980; Cruikshank and Silvaggio 1980; Fink *et al.* 1980; Apt *et al.* 1983; Spencer *et al.* 1990), with interpretations ranging from mostly solid to mostly gaseous. The spectra of solid and gaseous CH_4 are very similar, even at moderate resolutions, making these interpretations difficult. At high resolution, however, the spectrum of gaseous CH_4 contains lines from vibration-rotation transitions. These transitions do not occur for the solid, so they provide a means to distinguish between the solid and gaseous CH_4.

4.2 OBSERVATIONS

We obtained spectra of Pluto on 25 and 26 May 1992 (UT) with CSHELL, the eschelle spectrograph at NASA's Infrared Telescope Facility on Mauna Kea (Tokunaga *et al.* 1990). The spectral range was 5998 - 6018 cm^{-1} (1661.8 - 1666.9 nm), and contained the R(0) line and the Q branch of the $2\nu_3$ band of CH_4. We used a slit of 1.5 arcsec, for a nominal resolution ($\lambda/\Delta\lambda$) of 13,300. At this resolution, the rotation lines are readily distinguishable from the broad absorption of the CH_4 frost. We took spectra in beam-switched pairs. We will refer to these as the "A" beam and the "B" beam, and the pairs as "A1, B1," etc. The spectra were roughly aligned with the rows, with the A beam centered near row 15, and the B beam centered near row 35.

Table 4.1. Observation log.

		radial velocity (km/s)			# of	Exposure
object	H magnitude	from earth	from sun	airmass	exposures	time (s)
May 25						
532 Herculina	7.68	0.41	2.95	1.9-2.2	4	300
16 Cyg B	4.77	–37.7	n/a	1.2	6	60
Pluto	12.36	6.29	0.15	1.1-2.3	34	600
May 26						
532 Herculina	7.68	0.84	2.94	1.7-2.0	6	300
16 Cyg B	4.77	–37.7	n/a	1.2	6	60
Pluto	12.36	6.77	0.15	1.1-1.9	32	600

The rotational phase was 0.84 on 25 May (midway between the extremes in Pluto's rotational lightcurve, when Charon was just past western elongation) and 0.97 on 26 May (just prior to the minimum in Pluto's rotational lightcurve, when Charon was just before northern elongation). On both nights, the spectra included light from both bodies.

Our two primary standards were the asteroid 532 Herculina and the solar analog 16 Cyg B (Hardorp 1978; Campins *et al.* 1985). These were used to confirm the validity of

the modeled telluric and solar lines. The stars observed in the course of focusing and other start-of-night preparations included two other solar analogs, HD129655 and 35 Leo, which were used as secondary standards and checks on the reduction.

4.3 REDUCTION

We performed the normal preprocessing steps of dark subtraction, flat-field division, and interpolation over hot pixels. The hot pixels were generally different for each exposure, and were identified by eye for each exposure. A bias was subtracted from each exposure by the CSHELL electronics before it gets saved in a file. We removed most of the background by forming the differences of the beam-switched pairs, so that A1' = A1 –B1, B1' = B1 – A1, A2' = A2 –B2, etc. Fig. 4.1 shows an A beam exposure of 35 Leo with the B beam subtracted. For Pluto, we used the average of the two neighboring frames for the background image, so that A2' = A2 –(B1+B2)/2, etc. This eliminated most of the background signal and variation.

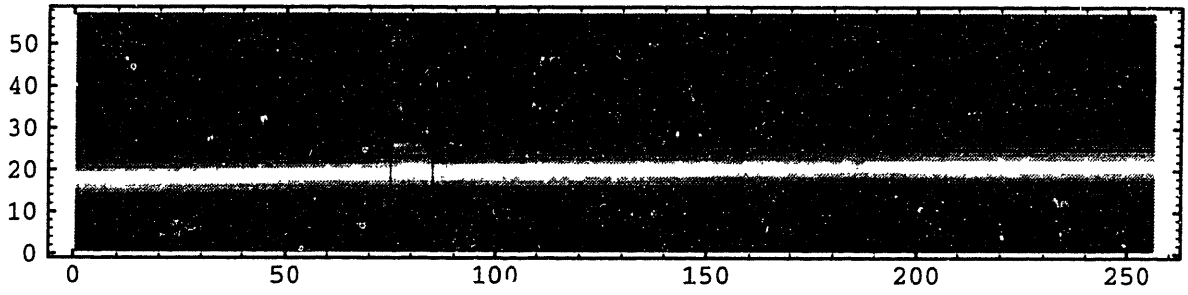

Figure 4.1. Standard-star frame with a background frame subtracted. Rows run from 1 to 57, columns run from 1 to 256, and bright is positive. The bright thick stripe at row 20 is the spectrum. For each column, the pixels between the two lines bordering the spectrum are included in the final one-dimensional spectrum. The background for each column is determined from the pixels above the line near row 50 and below the line near row 8. The dark (i.e., negative) stripe near row 40 is the subtracted B beam. The vertical lines mark the position of the slit. A residual image of a star is visible in the slit just above the spectrum.

We used IRAF's APALL package to extract the spectra, find the wavelength as a function of pixel, and interpolate the spectra to a common set of wavelengths.

A necessary step is to define the shape and position of the spectrum on the detector as a function of row versus column, which IRAF calls the "trace" of the spectrum. A 4^{th} order polynomial was fit to the traces of each of the standard spectra. The signal-to-noise ratio of a single Pluto exposure was too low for that spectrum to define the shape of its own trace. Instead, the standard spectra defined the shape as a function of center row, and this was used to extract the Pluto spectra.

The width of the trace is shown by the two lines flanking the bright spectrum in Fig. 4.1. We chose an 8-pixel wide trace, to avoid the signal from the inverted spectrum. This is a relatively narrow trace, containing 80% of the light, but tests showed the standard spectra were insensitive to the narrowing the aperture width to 8 pixels.

The background for each column was determined from the areas at the top and bottom of the column, away from either the positive or the negative spectrum (Fig. 4.1). The median of each region was found, and the background was linearly interpolated between the two medians. This allowed for a linear background while simultaneously offering some protection from outliers in the background. For the standards in the A beam, we defined the background regions as those pixels at least 10 pixels below the spectrum, or at least 33 pixels above. For the standards in the B beam, the limits were switched. For the Pluto exposures, we customized the limits on the background regions for each exposure. We required that background pixels had to be at least 10 pixels from any spectrum. If the smaller of the two background regions had fewer than 3 pixels, we only used only the larger region to determine the background.

We extracted the spectra with APALL's optimal algorithm. In the optimal algorithm, the shape of the stellar profile (in our case, signal versus row) is used to calculate the weights that will optimize the signal-to-noise ratio. The dispersion for the extracted

spectra was determined from four lines from the CSHELL's Xe, Kr, and Ar lamps. The resulting dispersion ranged from 0.0199 to 0.0204 nm per pixel. The spectra were then rebinned to 0.02 nm per pixel. The signal-to-noise for each spectrum was calculated from the scatter of its continuum. For each object, the spectra were all normalized, and then combined in a weighted mean. The error for each pixel was calculated from the scatter in the weight sum. The mean airmass for the combined spectrum was calculated using the same weights that were used for the combining the spectra.

4.4 ANALYSIS

The shapes of the standard spectra are the products of three effects: telluric absorption, solar lines, and a low order undulation caused by interference fringing. The Pluto spectra are the product of these three effects and the absorption by Pluto's atmospheric CH_4.

4.4.1 INTERFERENCE FRINGING

In the flat fields (taken with CSHELL's flat-field source lamp) and the twilight sky spectra, an obvious fringing pattern ran from the upper left to the lower right of the exposures. When spectra of the twilight sky or astronomical objects are divided by the flat fields, this fringing pattern does not flatten out completely. The uncancelled fringing is thought to be due to the difference between the f/# of the beam from the flat field lamps and the beam from the sky (Tokunaga, personal communication). The ratio of the flat fields for the two nights shows uncancelled fringing at the 7% level (Fig. 4.2), demonstrating that the fringing in the flat fields can change over time.

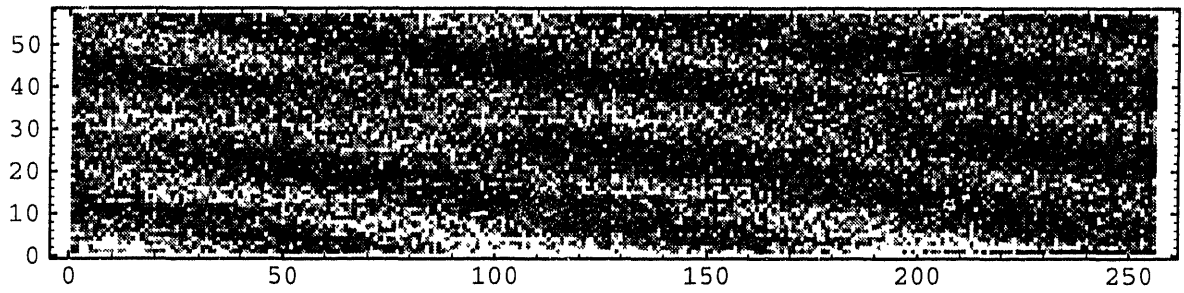

Figure 4.2. Interference fringing (2-D). The ratio of the flats for May 25 and 26 is plotted, with the intensity ranging from 0.93 (black) to 1.07 (white). The lines of light and dark that stretch from the upper left to the lower right are uncancelled interference fringes.

The undulations are of low order and periodic, and so are candidates for modeling with a Fourier series. The effect of the uncancelled fringing on a spectrum can be seen in Fig. 4.3, where a single spectrum of 35 Leo is divided by the nightly mean. Since the spectra were taken within a 12 minute period, the variation between the single spectrum and the mean must be purely instrumental, not solar or telluric. We found that the fringing can be well modeled by the first seven parameters in a Fourier series (a constant and three sine-cosine pairs).

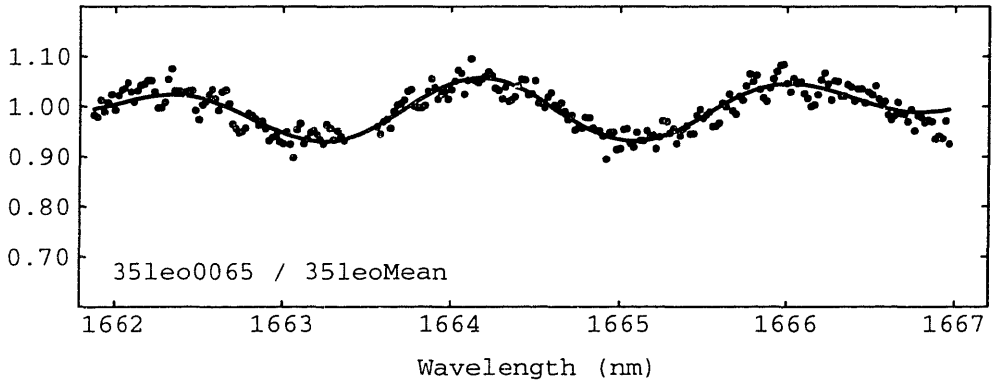

Figure 4.3. Interference fringing (1-D). A single observation of 35 Leo divided by the nightly mean. Since the observations were taken within a 12 minute span, the solar and telluric features cancel. The remaining variation is due to fringing. The line shows the fringing can be modeled with the first seven parameters in a Fourier series.

4.4.2 TELLURIC ABSORPTION

The ATRAN program (Lord 1992) generates telluric absorption for specified resolutions, wavelengths, and amount of precipitable H_2O. In the spectral region observed, the telluric absorptions are CH_4 and H_2O. This program assumes 1.6 parts per million (ppm) of CH_4. Measurements of Earth's atmospheric CH_4 at Cape Meares show an increase of about 0.14 ppm per decade, and a daily variation of only about 0.002 ppm (Khalil *et al.* 1993). Therefore, we could assume that the Earth's CH_4 abundance was constant during the two-day observing run, but we could not assume that it had the nominal value of 1.6 ppm. We used the standards to determine if the effective airmass had to be increased to account for an increase in the telluric CH_4. Although H_2O abundance can vary considerably during a night, the difference in absorption for 1000 mm and 3000 mm precipitable H_2O was less than 1%, at 1663.48 and 1666.27 nm. This was small enough to ignore, and all telluric absorption spectra were calculated for the mean value for 3000 mm precipitable H_2O.

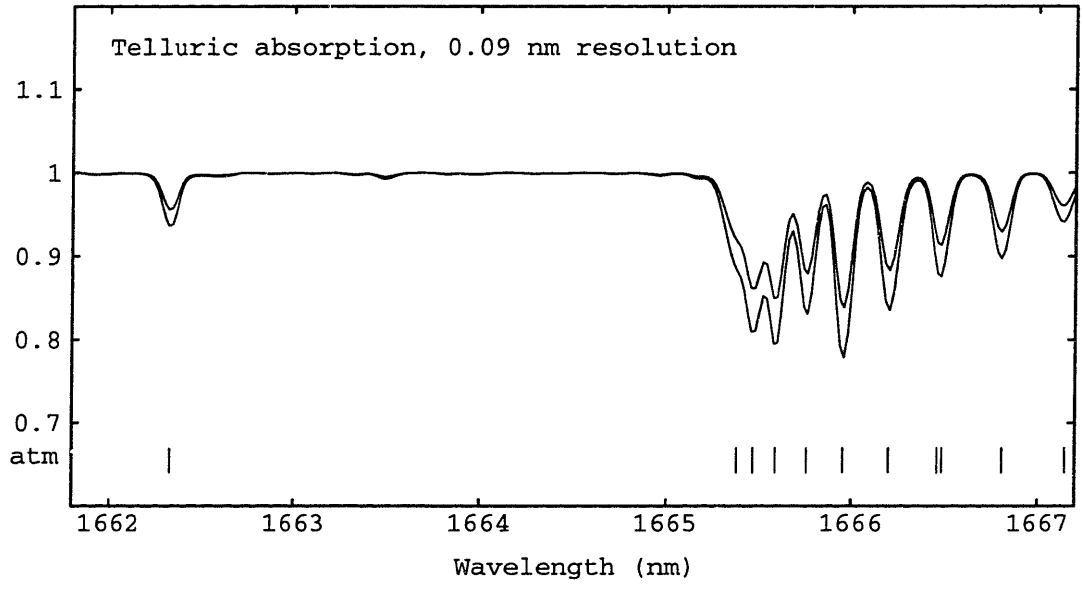

Figure 4.4. Calculated telluric absorption. The ticks mark the stronger atmospheric lines (all CH_4). The upper curve is the absorption at Pluto's mean airmass of 1.3, and the lower is at Herculina's mean airmass of 1.8. The data have been smoothed to 0.09 nm.

4.4.3 SOLAR SPECTRUM

The KPNO Solar Atlas (Livingston and Wallace 1991) is provided as a table of wavenumbers and normalized solar fluxes. They are tabulated every 0.0025 nm and have a resolution of 400,600.

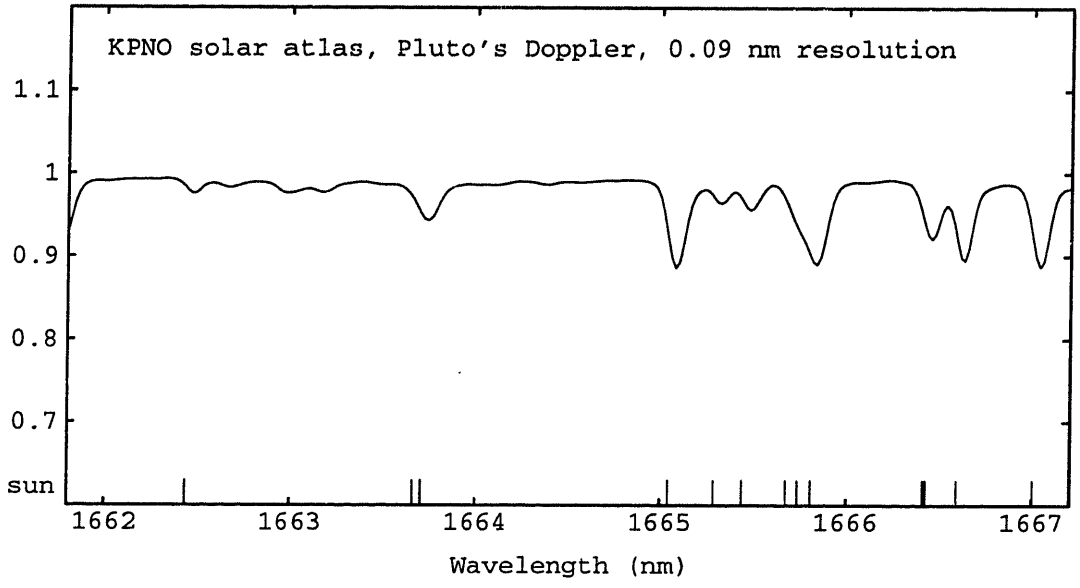

Figure 4.5. KPNO Solar Atlas. The ticks mark the stronger solar lines. The solar spectrum has been smoothed to 0.09 nm resolution.

4.4.4 PLUTO'S METHANE

The Doppler width (α_D) for a given temperature (T) and molecular weight (μ) is

$$\alpha_D = \frac{\nu_0}{c}\sqrt{\frac{2kT}{\mu m_{amu}}}. \qquad (4.1)$$

where k is Boltzmann's constant, and m_{amu} is the mass of one atomic mass unit. At 100 K and 3.4 μbar, the Doppler width is 6.65×10^{-3} cm^{-1}, while the collision-broadened width is only about 4×10^{-7} cm^{-1}. With this ratio in the widths, the pressure-broadened wings are not important, even for 50 cm-A of CH_4. It is therefore not necessary to use the Voigt

profile (the convolution of the Doppler-broadened and the collision-broadened line shapes). The CH_4 line shape, due entirely due to Doppler broadening, is a function of the wavenumber (ν) and the central wavenumber (ν_0):

$$L(\nu - \nu_0) = \frac{1}{\alpha_D \sqrt{\pi}} \exp\left[-\left(\frac{\nu - \nu_0}{\alpha_D} \right)^2 \right] \tag{4.2}$$

The Doppler line shape does not depend on the pressure. By assuming that most of the CH_4 was at a single temperature, we can calculate the absorption as a single-layer atmosphere. We call the amount of CH_4 needed in a single-layer atmosphere the "two-pass CH_4 abundance," since it represents the abundance seen by a photon making two passes through the atmosphere. As discussed in more detail in Section 4.5, the two-pass CH_4 abundances are roughly 4 times greater than the actual column height. Pluto's CH_4 absorption was calculated on a line-by-line basis, using the 65 lines in the HITRAN database that fell within our spectral range. The spectrum was calculated at a resolution of 0.00095 nm, and then binned to a resolution of 0.02 nm. The HITRAN database provides the wavenumber (ν_0, in cm^{-1}), the line strength at STP ($S(0)$, in cm $molecule^{-1}$), and the energy of the lower state (ν_i, in cm^{-1}). The line strength (S) at some other temperature T (Lord 1992) can be found by

$$S_i = S_i(0)\left(T/T_0\right)^{3/2} \frac{\exp\left[-hc\nu_i/kT\right]}{\exp\left[-hc\nu_i/kT_0\right]} \frac{\left(1-\exp\left[-hc\nu/kT\right]\right)}{\left(1-\exp\left[-hc\nu/kT_0\right]\right)} \tag{4.3}$$

The variation of the methane absorption with two-pass column height at 100 K is shown in Figure 4.3. Notice that the Q branch is significant even at low column heights, but does not increase quickly with concentration. Due to the narrowness of the Doppler width, some of the lines are quickly saturated, at which point the equivalent width increases slowly with column height.

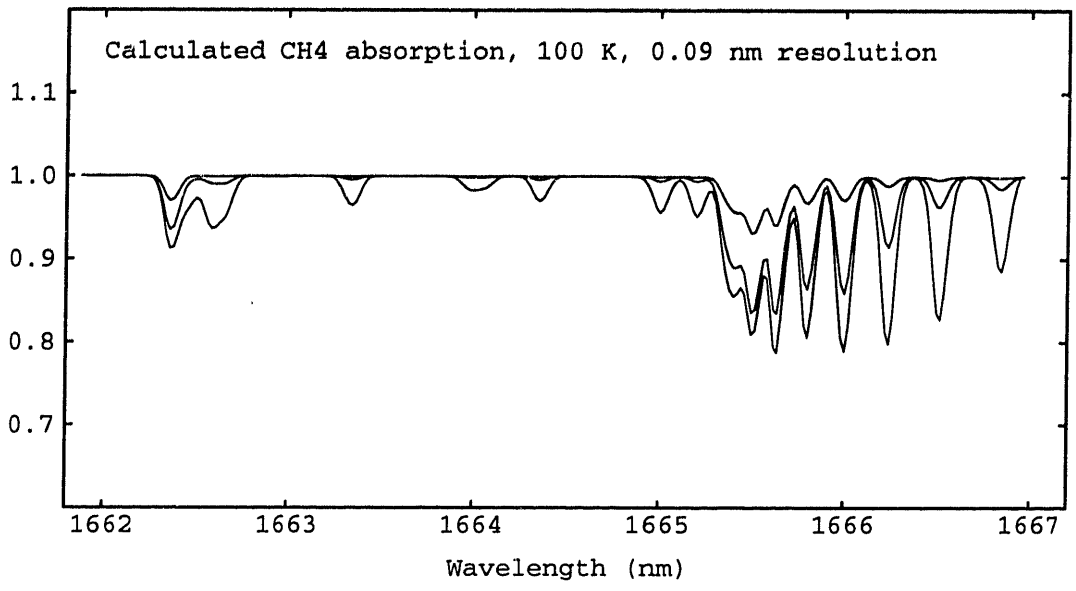

Figure 4.6. Calculated CH_4 absorption at 100K and 3.4 μbar. The three spectra shown have been calculated for two-pass abundances of 0.1, 1.0, and 10.0 cm-A. The spectra have been smoothed to 0.09 nm resolution.

We need to include Charon's contribution to the system flux. Spectra taken during the mutual events have not detected any CH_4 on Charon (Buie *et al.* 1987; Marcialis *et al.* 1987; Fink and DiSanti 1988), so the flux from Charon is assumed to be constant over this wavelength region. During an eclipse of Charon by Pluto, Buie *et al.* (1987) measured Charon's relative flux with a CVF at a bandpass of 1.62 – 1.72 μm. The average system flux within this range is higher than the system flux at 1.662 – 1.667 μm (Owen *et al.* 1993). From these two sets of observations, we find that Charon contributes an average of 22% of the system flux in the range 1.662 –1.667 μm. In this calculation, we ignore the variation of the depth of the CH_4 frost features with rotation. The system flux (F) is found from the calculated CH_4 transmission spectrum (T_{CH4}) by

$$F = 0.78T_{CH4} + 0.22 \qquad (4.4)$$

4.4.5 STANDARD SPECTRA

Dividing the Pluto spectra by the standard spectra would have been a difficult way to reduce this dataset, because the three objects (Pluto, 16 Cyg B, and 532 Herculina) each had Doppler shifts of several pixels. Furthermore, the ATRAN telluric absorption program and the KPNO Solar Atlas were of higher quality than our standard spectra, especially considering the fringing. Our approach was to fit the calculated telluric absorption and the solar atlas to the standard spectra, to (i) demonstrate that these calculated absorptions match the standard spectra; (ii) identify any instrumental effects that needed to be accounted for (in addition to the fringing); and (iii) determine if the calculated calibrations had to be adjusted. To adjust the telluric absorption for a possible increase in Earth's telluric CH_4, we calculated the absorption at an effective airmass, where $X_{eff} = (1+a)\ X$. Although 16 Cyg B is rated as a solar analog, we expected some differences at this resolution. However, we also expected that the strengths of the lines would vary in tandem, if they varied at all. To allow this variation, we raised the solar atlas to the $(1 + s)$ power.

Table 4.2 and Figs. 4.7 and 4.8 show the results of the fits to the standards. Because the objects were narrower than the slit, the resolution on any one exposure depended on the seeing and tracking during that exposure. The telluric resolution is the full width half max (FWHM) of a convolving gaussian applied to the ATRAN absorption spectrum to degrade it to the observed resolution. Objects that fill the 1.5 arcsec slit have the instrumental resolution, but our objects were narrower than the slit. The resolution for a given exposure depended on the seeing and tracking during that exposure. It is somewhat different for the two spectra, and we will keep it as a free parameter when we fit the Pluto spectra. The KPNO Solar Atlas is a solar spectrum of the center of the sun's disk. To account for a widening of the disk-integrated solar flux (reflected by 532 Herculina or

approximated by the solar analog 16 Cyg B), we allowed the KPNO atlas to be convolved by a Gaussian with a different FWHM. The difference between the two widths is about 0.002 for both objects, and we take that as the empirical relationship between the solar and telluric convolving widths. The precise wavelength per pixel also depends on the position of the object in the slit. The average wavelength shifts of the combined spectra are different for the two objects by about three pixel's worth. The dispersion also changes slightly from the nominal value of 0.02 nm pixel^{-1}. The seven Fourier terms describing the fringing were free parameters, but are not listed in Table 4.2.

Table 4.2. Fits to the standards.

param	532 Herculina	16 Cyg B	For Pluto
telluric resolution (nm)	0.0906 ± 0.0024	0.0952 ± 0.0042	free
solar resolution (nm)	0.1077 ± 0.0062	0.1144 ± 0.0062	(see text)
wavelength shift (nm)	0.0025 ±0.0049	0.0594 ± 0.0069	free
dispersion (nm pixel^{-1})	0.019987 ± 0.000024	0.019823 ± 0.000032	0.02
adjustment to Doppler (nm)	0.00072 ± 0.00026	–0.00009 ± 0.00029	0
Telluric increase	0.002 ± 0.036	–0.049 ± 0.060	0
Solar increase	–0.009 ± 0.047	0.092 ± 0.054	0
Fit information			
degrees of freedom	222	222	
χ^2	128.4	288.3	

We expected the next three parameters to be zero, as they are. A change in the Doppler shift would indicate we had calculated the velocity incorrectly. As discussed in 4.4.2, we were looking for any increase in the observed telluric CH_4 relative to the calculated telluric CH_4. The telluric absorption apparently did not increase enough to warrant our changing the ATRAN output. As expected, the solar spectrum had to be adjusted to match the solar analog, but not to match the reflected sunlight from the asteroid. Finally, we note that the quality of the fits allows us to confidently apply the fringing and the calculated solar and telluric absorption to Pluto.

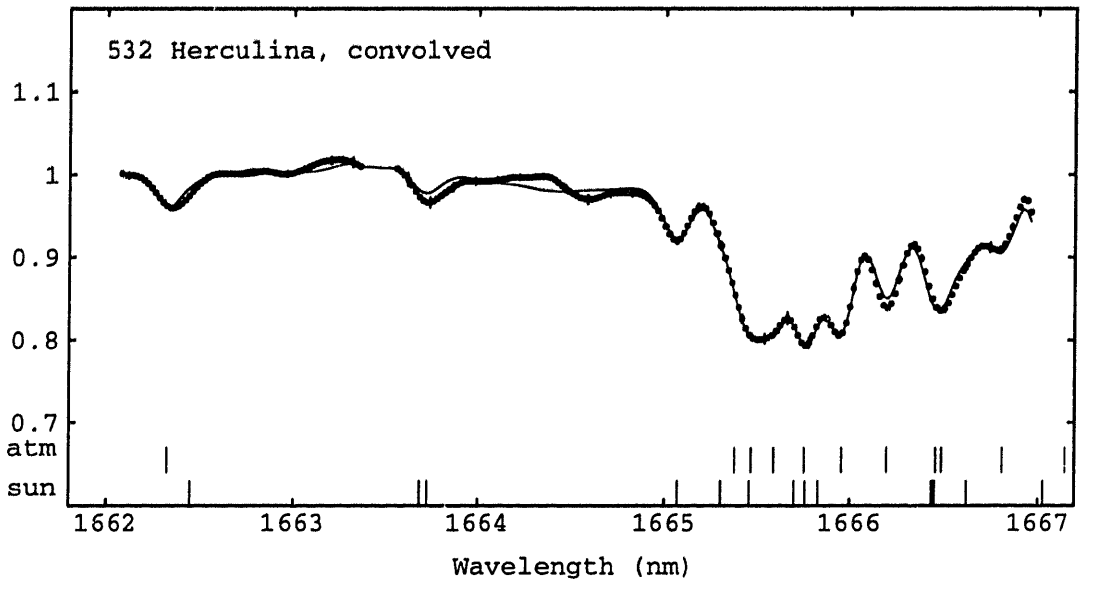

Figure 4.7. Fit of interference fringing, solar, and telluric lines to 532 Herculina. The points are the data, and the line is the model.

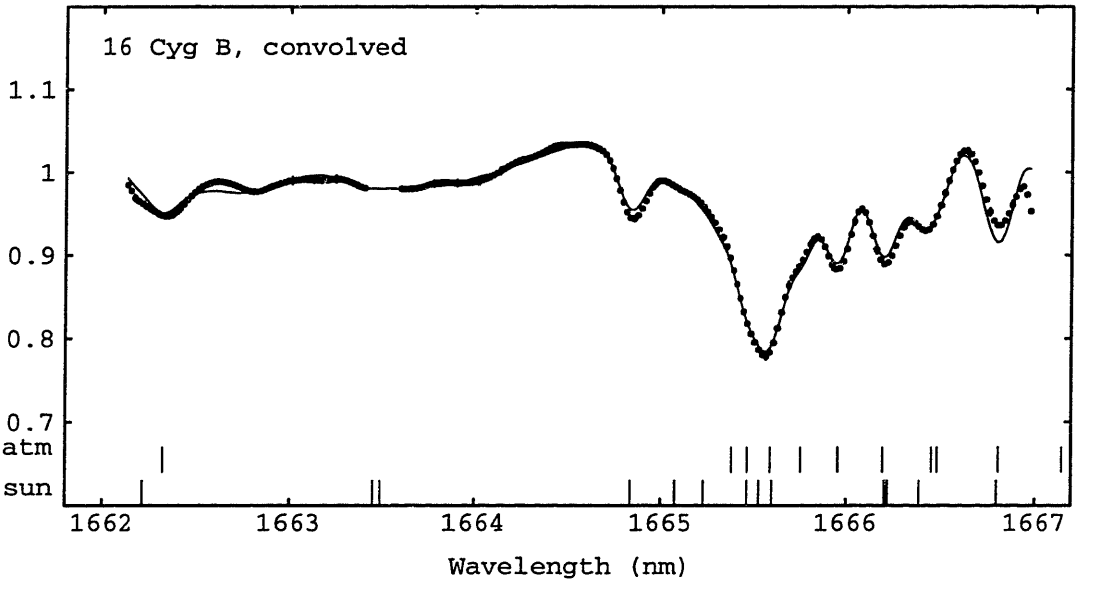

Figure 4.8. Fit of interference fringing, solar, and telluric lines to 16 Cyg B. The points are the data, and the line is the model.

4.4.6 PARAMETER-SPACE SEARCH

With the atmospheric and solar contributions confirmed with the standards, these could be taken as given when we fit to Pluto. To find the approximate column height, we

performed a search of parameter space. The CH_4 abundance is set to test values and a fit is performed. This results in a χ^2 for each test abundance. Fig. 4.10 shows the minimum χ^2 for observed abundances of 0.1, 0.2, 0.5, 1.0, 2.0, 5.0, 10, 20, and 50 cm-A. In these fits, the temperature was fixed at 100 K, the width of the convolving Gaussian was fixed at 0.12 nm, the wavelength shift was 0 nm, and the dispersion was 0.02 nm pixel^{-1}. The Fourier coefficients were the only free parameters. The minimum χ^2 is near 2.7 cm-A, so that is where we begin our least-squares fits.

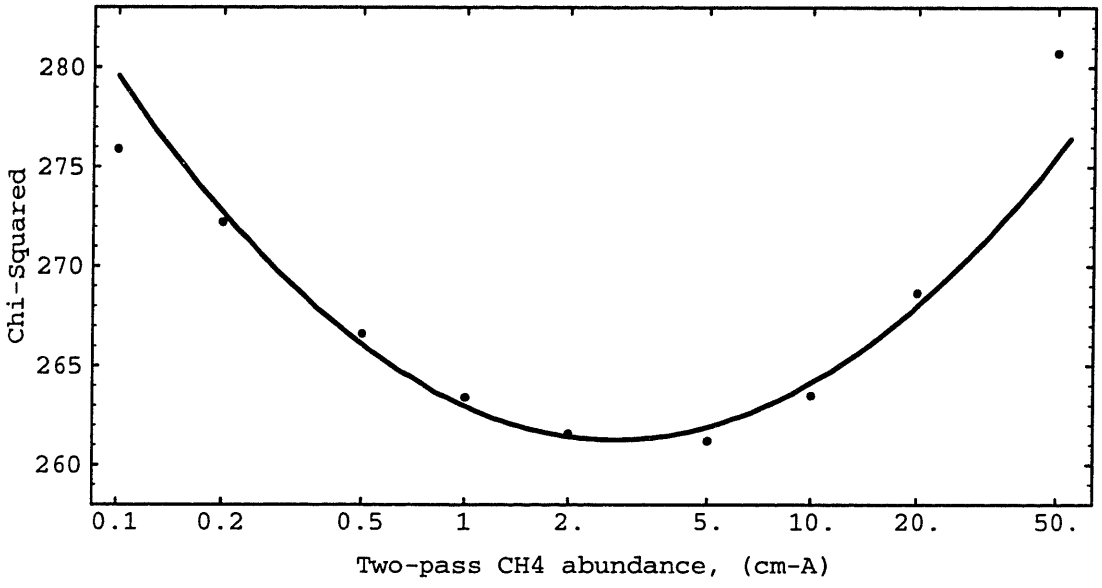

Figure 4.9. Parameter-space search for two-pass CH_4 abundance. Fits were performed holding the temperature at 100 K and observed abundance at the plotted x values. The minimum abundance is near 2.7 cm-A, indicating the initial parameters we should use for a least-squares fit for the observed abundance.

4.5 RESULTS

We fit for the methane abundance, the telluric resolution, the wavelength shift, and the fringing parameters. We fix the temperature at 100 K, the temperature derived from the stellar occultation for a predominately N_2 atmosphere. Allowing the dispersion to be free results in wavelength shifts up to 20 pixels. This should be investigated further, but

for now, we also hold the dispersion fixed at 0.02 nm pixel^{-1}. The best-fit two-pass abundance is listed in Table 4.3.

Table 4.3. Atmospheric CH_4 abundance.

parameter	$T = 100$
two-pass CH_4 abundance (cm-A)	$4.81^{+12.60}_{-3.48}$
airmass factor (assumed)	4
CH_4 column height, ξ_{CH_4} (cm-A)	$1.20^{+3.15}_{-0.87}$
fit information	
degrees of freedom	228
χ^2	258

The data are plotted in Fig. 4.10, along with the complete model (lower line) and a model that includes just the fringing, atmospheric absorption, and solar lines (upper line). The spectrum from the Pluto-Charon system is plotted in Fig 4.11. This is the data plotted in Fig. 4.10, divided by the upper line of Fig. 4.10.

Because the data have been smoothed for plotting in Figs. 4.7, 4.8, 4.10, and 4.11, the points are correlated. Error bars have been plotted on every 6th pixel; to get a better idea of the uncorrelated spectrum, imagine the spectrum consisting of only the pixels with error bars. The large dips in Fig. 4.10 at 1665.5 nm, 1666.0 nm, and 1666.2 nm are due to a combination of solar lines, telluric CH_4, and Pluto's CH_4. The absorptions due to solar and telluric lines alone (upper line) are too shallow to explain the observed dips. When the data are divided by the modeled fringing, the solar lines, and the telluric lines (Fig. 4.11), these three features remain, and are due entirely to Pluto's CH_4. The features shortward of 1665 nm are due to random noise. The peak in the data at 1665.8 nm does not appear in the model, and this prevents the model from going deep enough at 1665.5 nm and 1666.0 nm. This increases the formal error, and probably leads to an underestimate in the CH_4 abundance.

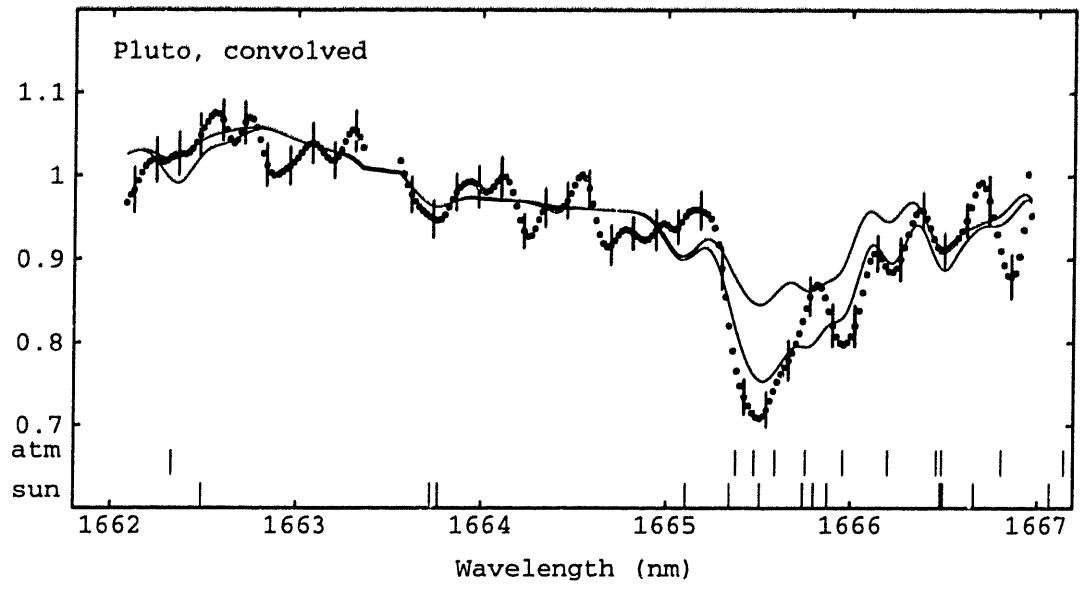

Figure 4.10 Convolved Pluto-Charon data and models. The upper line is the product of (i) solar lines; (ii) telluric absorption for Pluto's mean airmass of 1.25; and (iii) a low order undulation in the continuum due to interference fringing. The lower line is the product of the above three effects and Pluto's methane at a temperature of 100 K and a two-path column height of 4.81 cm-A. The model and data have been smoothed by convolution with a Gaussian of FWHM = 0.12 nm.

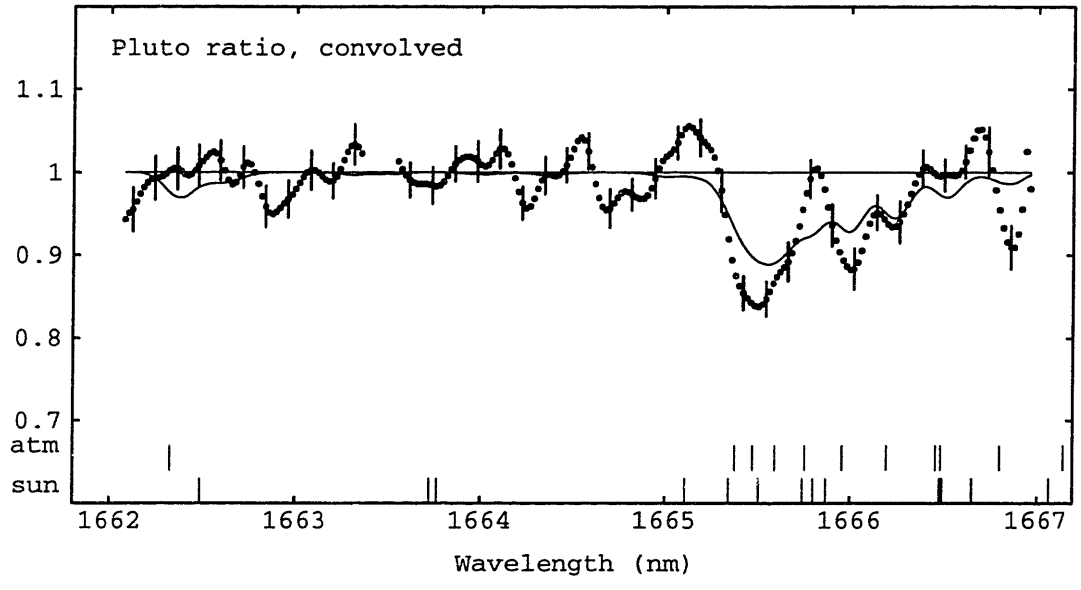

Figure 4.11 Convolved, calibrated Pluto-Charon. This figure shows the data of Fig. 4.10, divided by the upper line of Fig. 4.10. Thus, this is the spectrum from Pluto and Charon. The remaining features are due to methane in Pluto's atmosphere. The lower line is Pluto's methane at a temperature of 100 K and a two-path column height of 4.81 cm-A. The model and data have been smoothed by convolution with a Gaussian of FWHM = 0.12 nm. The CH_4 features are visible at 1665.5 nm, 1666.0 nm, and 1666.2 nm.

The two-pass abundance is converted into the column height, by dividing by the "airmass factor." This factor takes account of two effects. The first effect is that the atmosphere gets two chances to absorb a photon – once when the light travels from the top of the atmosphere to the surface and again after it is reflected from the surface. An additional effect is that the effective airmass of the atmosphere is one at the center of the disk, and increases toward the limb. A Lambert sphere has an airmass factor of 3, while a planet with no limb darkening has an airmass factor of 4. E. Young and Binzel (1994) found that Pluto was not limb darkened. A detailed integration over the albedo distribution of Pluto (using the map of Buie *et al.* 1992) confirms an airmass factor near 4. If Pluto's atmosphere has a haze, the effective path length, and therefore the airmass factor, would be higher.

CHAPTER 5
SYNTHESIS

5.1 INTRODUCTION

The 1988 stellar occultation probed Pluto's atmosphere down to about 1206 km from Pluto's center (Chapter 3). From a radius of about 1500 km to a radius of 1215± 11 km, the occultation light curve is consistent with that caused by an isothermal N_2 atmosphere with a temperature of about 100 K. Just below half-light, the occultation light curve shows a kink, indicating a change in the atmospheric structure. The light curve below the kink can be explained by a temperature inversion of 10 – 30 K km^{-1} (Eshleman 1989; Hubbard *et al.* 1990; Stansberry *et al.* 1994), an extinction layer (Elliot *et al.* 1989; Elliot and Young 1992), or some intermediate structure. We refer to the radius of the kink as the transition radius, the isothermal region between the transition radius and 1500 km as the middle atmosphere, and the region below the kink as the lower atmosphere (Fig. 5.1).

The occultation cannot distinguish among three proposed structures for the lower atmosphere: (i) an absorbing haze with an optical depth greater than 0.145 (Elliot and Young 1992); (ii) a steep temperature inversion directly above a surface just a few km below the transition radius (Eshleman 1989; Hubbard *et al.* 1990); or (iii) a steep temperature inversion overlying a deep troposphere (Stansberry *et al.* 1994). The three models predict different surface pressures, temperatures, and radii. Therefore they also predict different bulk densities. By examining the physical and observational constraints on the surface, the middle atmosphere, and the lower atmosphere, we can find self-consistent models for the lower atmosphere.

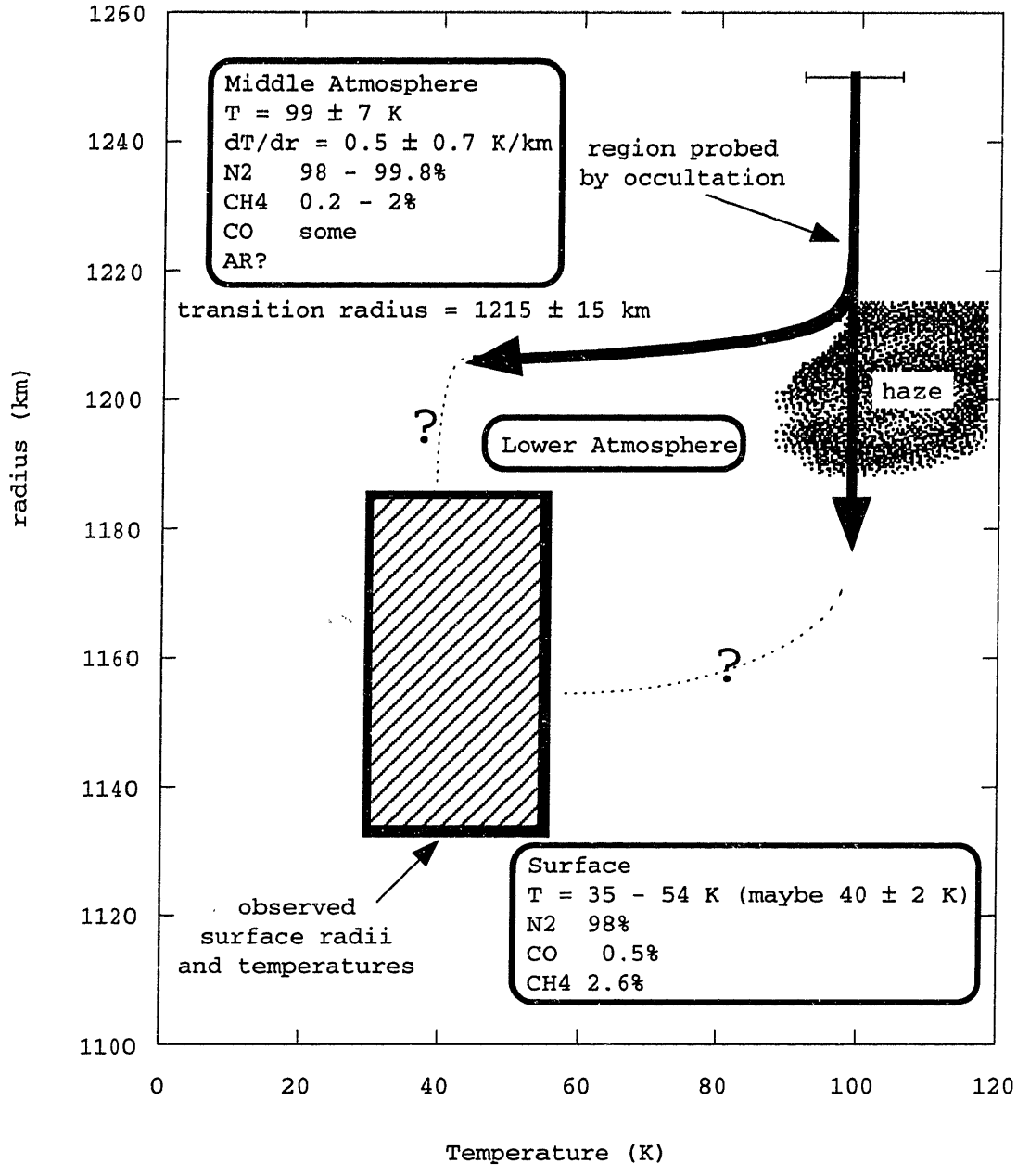

Figure 5.1. Observed temperatures and radii of Pluto's surface and atmosphere. The stellar occultation indicates a transition in the structure near 1215 km. The middle atmosphere, above this radius, has a temperature of 99 ± 7 K for an N_2 atmosphere. Interpretation of the occultation for the lower atmosphere depends on whether the atmosphere is assumed to have a steep temperature gradient or an abrupt extinction layer. In either case, there are no detections of the temperature in the lower atmosphere between the surface and the last radius observed by the occultation (marked with arrowheads). The box represents the range of reported values for the radius of visible limb (Buie *et al.* 1992; E. Young and Binzel 1994) and temperature of the surface (see Jewitt 1993, for a review). Hence, the solid curve must take a path that ends somewhere within or below the box.

5.2 SURFACE

5.2.1 SURFACE COMPOSITION

Modeling of near-IR reflectance spectra indicates that Pluto's frost is primarily N_2, with some CO and CH_4, and that the CH_4 bands are shifted, suggesting that CH_4 is mixed with the N_2 at the molecular level (Owen *et al.* 1993).

Table 5.1. Surface composition (Owen *et al.* 1993).

species	surface mass fraction (%)	surface mole fraction (%)
CH_4	$1.5^{+1.5}_{-0.7}$	$2.6^{+2.6}_{-1.4}$
CO	$0.5^{+0.5}_{-0.2}$	$0.5^{+0.5}_{-0.2}$
N_2	$98^{+0.9}_{-2.0}$	$97^{+1.6}_{-3.1}$

Maps of Pluto's albedo from the mutual events show extreme variation, ranging from albedos near 1.0 at the south pole (as defined by the right-hand rule) to albedos near 0.2 in the southern equatorial region (Buie *et al.* 1992; E. Young and Binzel 1993). The bright areas appear to be areas of CH_4 concentration, since CH_4 absorption lines are deepest when Pluto is brightest (Marcialis and Lebofsky 1990). The composition of the dark areas is unknown.

5.2.2 VAPOR-PRESSURE EQUILIBRIUM

Pluto's atmosphere is generally assumed to be in vapor-pressure equilibrium with its surface, as is the case for Triton, Io, and the Martian polar caps. In vapor-pressure equilibrium, the number of molecules leaving an area every second has to equal the number of molecules being redeposited. An atmosphere that is in contact with the surface will stick to the surface with a rate (molecule s^{-1} cm^{-2}) of

$$\left(\frac{dN}{dt}\right)_{dep} = fvp_s / (4kT_s) \qquad (5.1)$$

where f is the sticking coefficient, v is the mean molecular speed of the gas, p_s is the surface pressure, and N is the column abundance of the atmosphere (Trafton 1990). The rate of sublimation is

$$\left(\frac{dN}{dt}\right)_{sub} = \begin{cases} fvP_{sat}(T)/(4kT_s), & \text{frost on surface} \\ 0, & \text{no frost on surface} \end{cases} \tag{5.2}$$

where $P_{sat}(T)$ is the saturation vapor pressure at temperature T. Since the surface pressures and temperatures are implicitly functions of location, so are the deposition and sublimation rates.

The assumption of vapor-pressure equilibrium is rooted in the conservation of mass, or $dN/dt = 0$. In a closed system in steady state, $dN/dt = (dN/dt)_{sub} - (dN/dt)_{dep}$. If $p_s > P_{sat}(T)$, then the deposition rate exceeds the sublimation rate, and the atmosphere will freeze out onto the surface, lowering the column abundance and thus the surface pressure. At the same time, it releases the latent heat of vaporization, raising the surface temperature and saturation vapor pressure. This continues until equilibrium, when $p_s = P_{sat}(T)$. Conversely, if $p_s < P_{sat}(T)$, then the sublimation rate exceeds the deposition rate and any available frost will sublime, increasing the surface pressure. This will continue until equilibrium is reached, as before, or until there is no more frost available on the surface.

An atmospheric column on Pluto is neither a closed system nor in steady state, so there will be some departure from vapor-pressure equilibrium. Gas is leaving the top of the column at the escape rate, R_{esc}, and leaving the sides of the column depending on the wind velocities, while Pluto's atmosphere is changing its total bulk based on the insolation:

$$\frac{dN}{dt} = \left(\frac{dN}{dt}\right)_{sub} - \left(\frac{dN}{dt}\right)_{dep} - R_{esc}(t) - \nabla\cdot(N\mathbf{v}) \tag{5.3}$$

Here, $-\nabla\cdot(N\mathbf{v})$ is the vertically integrated flux convergence. We consider the effects of non-zero R_{esc}, dN/dt, or $\nabla\cdot(N\mathbf{v})$ separately. Including an escape rate of ~2 × 10^{10} molecule s^{-1} cm^{-2} (Trafton 1990) lowers the surface pressure to about 10^{-7} μbar below the saturation vapor pressure. If half the atmosphere freezes out over the next 20 years (E. Young 1992), the resulting dN/dt is on the order of 10^{12} molecule s^{-1} cm^{-2}, causing a deviation from equilibrium of about 10^{-5} μbar. The winds transport mass from the equator to the poles, which, through the latent heat, transport energy as well. The frost will deposit on the night side at a rate that balances the heat lost by thermal radiation (Trafton and Stern 1983; E. Young 1992),

$$L\left[(dN/dt)_{sub} - (dN/dt)_{dep}\right] = (1-A)F\cos\Psi - \varepsilon\sigma T^4 \tag{5.4}$$

where L is the latent heat of sublimation (J $molecule^{-1}$), A is the albedo, F is the solar flux (J s^{-1} cm^{-2}), and Ψ is the angle from the sub solar point. For N_2 at $T = 40$ K, the surface pressures on the night side are about 3 × 10^{-3} μbar greater than the saturation vapor pressures.

These departures from vapor-pressure equilibrium are small compared with the surface pressures (at least 2.4 μbar and probably nearer to 50 μbar). Furthermore, if the system is somehow forced into a state of disequilibrium, the time scale for the system to relax to hydrostatic and vapor-pressure equilibrium is only about 20 minutes (Trafton 1990). Therefore, we assume the surface is in vapor-pressure equilibrium with the surface frosts.

We assume the mixture of frosts is an ideal solution (Trafton 1990), so the partial pressure (p_i) of the i^{th} molecular species is proportional to its molar mixing ratio in the ice, X_i.

$$p_i = X_i P_{sat,i}(T) \tag{5.5}$$

N_2 is more volatile than either CH_4 or CO, and it is the dominant volatile detected in the frost. Therefore, the atmosphere is mostly N_2 (Owen *et al.* 1993).

5.2.3 SURFACE TEMPERATURE

Since the atmosphere is in vapor-pressure equilibrium with the surface, the partial pressure of each species is determined by the surface temperature through Eq. (5.5). Even in the absence of sublimation and deposition, the frost temperatures will be maintained on the night side due to the storage of heat in the subsurface frost. Bodies are divided into fast or slow rotators according to the thermal parameter Θ (Lebofsky and Spencer 1989). Slow rotators ($\Theta < 0.1$) emit all their absorbed sunlight on the sunlit hemisphere, and fast rotators ($\Theta > 10$) have the same temperature on the night side as the day side. This parameter depends on the thermal inertia (Γ), the emissivity (ε), the Stefan-Boltzmann constant (σ), the angular velocity of the body (ω), and the temperature that the sub solar point would have in the slow rotating limit (T_{ss}):

$$\Theta = \frac{\Gamma\sqrt{\omega}}{\varepsilon\sigma T_{ss}^3} \tag{5.6}$$

Using $\Gamma = 5.3 \times 10^5$ erg cm^{-2} sec$^{-1/2}$ K^{-1} (Table 5.2, from Spencer and Moore (1992)), and taking $\varepsilon = 1.0$ and $T_{ss} = 55$ K, we find $\Theta \approx 255$, so Pluto is a fast rotator by this criterion, and an area of frost will remain essentially isothermal during its day-night cycle.

At perihelion, the equator receives more sunlight than the pole. To maintain a global temperature, energy has to be transported poleward. This is accomplished through the latent heat of sublimation. At the equator, solar energy expended for sublimation; the gas is transported to the poles, where it is redeposited, releasing the latent heat. The transport of mass and energy will keep the frost-covered areas at a global temperature as long as the wind velocities (v) needed to transport the mass are much less than the speed of sound, (v_s)

Table 5.2 Thermophysical Properties of Relevant Ices

Ice	T (K)	c erg g^{-1} K^{-1}	k erg cm^{-1} s^{-1} K^{-1}	ρ g cm^{-3}	Γ erg cm^{-2} $s^{-1/2}$ K^{-1}
N_2 (α)	30	1.2×10^7	2.9×10^4	1.0	5.9×10^5
N_2 (β)	40	1.3×10^7	2.1×10^4	1.0	5.3×10^5
CH_4	30	1.5×10^7	3.8×10^4	0.52	5.4×10^5
CH_4	40	1.8×10^7	4.2×10^4	0.52	6.3×10^5

(Ingersoll 1990; Trafton and Stern 1983; E. Young 1992). This is the case for Pluto at perihelion (E. Young 1992).

Pluto's temperature has been derived from its thermal flux (Sykes *et al.* 1987· Tedesco *et al.* 1987; Altenhoff *et al.* 1988; Jewitt 1993; Stern *et al.* 1993). As reviewed by Jewitt (1993), the fluxes from shorter wavelengths (60 - 100 μm) indicate temperatures near 53-59 (Aumann and Walker 1987; Sykes *et al.* 1987, both analyzing the 1983 Aug. 16 IRAS observations), while the fluxes from the longer wavelengths (800 –1300 μm) indicate temperatures near 30 - 44 K (Altenhoff *et al.* 1988; Stern *et al.* 1993). The two sets of fluxes cannot be fit by a Pluto whose surface is isothermal with an emissivity independent of wavelength. A non-isothermal Pluto with a lower temperature of 35 K and an upper temperature between 50 and 75 K can fit the two wavelength regions (Jewitt 1993). The solution is underconstrained; not only are there probably two temperatures on Pluto, each perhaps with its own emissivity and albedo, but Charon's thermal flux must be included as well. In particular, the fluxes cannot set a lower limit on the colder temperature (Jewitt 1994, personal communication).

A frost temperature of 40 ± 2 K has been derived from the 2.148 μm N_2 feature (Tryka *et al.* 1994). The shape of this feature is sensitive to the temperature and phase of N_2 frost (Grundy *et al.* 1993), and has also been used to determine the frost temperature and phase of N_2 frost on Triton (Tryka 1993).

Table 5.3. Surface temperatures

Frost Temperature (K)	Reference
53–54	(Sykes et al. 1987)
30-44	(Stern et al. 1993)
35 (assumed)	(Jewitt 1993)
40 ± 2	(Tryka *et al.* 1994)

5.2.4 SURFACE RADIUS

In the 1980s, Pluto and Charon passed in front of and behind each other in a series of eclipses, occultations, and transits collectively termed mutual events. Analyses of the mutual event season (Buie *et al.* 1992; E. Young and Binzel 1993; E. Young and Binzel 1994) have provided the elements of Charon's orbit (except the semimajor axis), albedo maps of the Charon-facing side of Pluto and the Pluto-facing side of Charon, and the ratios of the radii of Pluto and Charon to the semimajor axis. The semimajor axis of Charon's orbit around Pluto (a) is needed to calculate the radii from these ratios. This was presented in Chapter 2, in which we described measurements of the motions of Pluto and Charon around the system barycenter. The results are summarized in Tables 5.4a and 5.4b.

Table 5.4a. Fitted results from Chapter 2

		correlation (%)		
parameter	value	q	a	i
mass ratio, q	0.1566 ± 0.0035	100	-1	-2
semimajor axis, a (km)	16460 ± 58	-1	100	28
inclination, i (deg)	95.00 ± 0.24	-2	28	100

Table 5.4b. Derived results from Chapter 2

parameter	value
system mass, M_{sys} (10^{24} g)	14.32 ± 0.13
Pluto mass, M_p (10^{24} g)	12.38 ± 0.12
Charon mass, M_c (10^{24} g)	1.94 ± 0.04
gravitational acceleration at 1250 km, g_0 (cm s^{-2})	52.87 ± 0.51

Radii for Pluto and Charon are given in Table 5.5, using the semimajor axis from Table 5.4a. These Pluto radii refer to the visible limb of Pluto, which may or may not be the solid surface (Elliot and Young 1992). The errors in the scaled radii are the formal errors. The errors in the radii include the propagated errors in the semimajor axis, and, for E. Young and Binzel, the errors in the inclination of Charon's orbit and the error in Charon's relative flux. We use the radii calculated by Buie *et al.* (1992) as a lower limit on the surface, if the solid surface is detected, and the results of E. Young and Binzel (1994) as an upper limit on the visible limb in the haze model.

Table 5.5. Mutual event results

parameter	Buie *et al.* 1992	E. Young & Binzel 1994
period, P (d)	6.387245 ± 0.000012	
scaled radius of Pluto, R_p/a	0.0586 ± 0.0004	0.0599 ± 0.0003
scaled radius of Charon, R_c/a	0.0302 ± 0.0005	0.0320 ± 0.0008
radius of Pluto, R_p (km)	1140 ± 7	1165 ± 23
radius of Charon, R_c (km)	588 ± 13	623 ± 21

As discussed in Section 5.3.1, the stellar occultation provides upper limits to the surface radii. The maximum surface radius for the haze model is 1181± 11 km, while the maximum surface radius for the thermal gradient model is 1206 ±11 km (Table 5.7, with errors assumed to be the error on r_1 from Table 5.6).

5.3 UPPER ATMOSPHERE

5.3.1 STELLAR OCCULTATION

A model occultation light curve was fit to the 1988 Pluto occultation, as described in Chapter 3. This model included a temperature gradient, described by $T = T_0(r/r_0)^b$, and an extinction layer below a transition radius r_1, described by a linear optical depth of $\kappa(r) = \kappa_1 \exp\left[-(r-r_1)r_1/(H_{\tau 1} r)\right]$. Parameters have the subscript "0" if they are tabulated at the reference radius, r_0 = 1250 km, and the subscript "1" if they are tabulated at the

transition radius. These results in Table 5.6 are identical to that of Elliot and Young (1992).

Table 5.6. Fitted occultation parameters

parameter	value	correlation (%)					
		ν_0	λ_0	b	r_1	$H_{\tau 1}$	$\kappa_{\tau 1}$
refractivity, ν_0	$(0.97 \pm 0.17) \times 10^{-9}$	100	-15	35	95	-11	-2
energy ratio, λ_0	22.4 ± 1.8	-15	100	-94	14	15	13
power index for temperature, b	-0.61 ± 0.87	35	-94	100	10	-23	-16
transition radius, r_1 (km)	1215 ± 11	95	14	10	100	-9	-2
haze scale height, $H_{\tau 1}$ (km)	29.8 ± 5.6	-11	15	-23	-9	100	79
absorption coefficient, $\kappa_{\tau 1}$ (cm^{-1})	$(2.22 \pm 0.18) \times 10^{-8}$	-2	13	-16	-2	79	100

The lower portion of the light curve can be explained by a steep thermal gradient with the Bates thermal profile (Stansberry *et al.* 1994):

$$T(r) = T_\infty \left(1 - \alpha \exp\left[-(r^3 - r_3^3)\beta / 3r_3^2\right]\right) \tag{5.7}$$

with $r_3 = 1206$, $\alpha = 0.5$ and $\beta = 0.65$.

Table 5.7 lists the results of the occultation that are independent of the composition. The upper limit on the radius for the haze model is the radius at which the star is last detectable (Elliot and Young 1992). The profiles considered by Stansberry *et al.* (1994) depart from the Bates profile at a radius of 1206 km, which we take to be the upper limit on the radius in the inversion model. The first six values in Table 5.7 are those of Elliot and Young (1992); the only difference is the improved value for Pluto's mass (Section 2). The final three parameters are estimated from the profiles of Stansberry *et al.* (1994).

The temperature and its gradient depend on the molecular weight of the gas, while the number density depends on the refractivity of the gas at STP (standard temperature and pressure). Since the surface frost is 98% N_2, we assume the atmosphere is dominated by N_2.

Table 5.7. Occultation results independent of composition.

Parameters	Value
atmosphere above transition	
scale height, H_0 (km)	55.7±4.5
temperature-molecular weight ratio, T_0 / μ_0 (K)	3.54±0.29
fractional thermal gradient, $(dT/dr)_0$ / T_0 (km^{-1})	$(-4.9\pm7.0)\times10^{-4}$
haze, no steep thermal gradient	
surface radius (km)	<=1181
vertical thickness of haze (km)	>= 34
vertical optical depth, τ_v	>= 0.145
steep thermal gradient, no haze	
surface radius (km)	<=1206
T (1206) / T_∞	0.5
$(1/T_\infty)$ (dT/dr) at 1250 km (km^{-1})	0.35

Table 5.8. Occultation results for an N_2 atmosphere.

Parameters	100% N_2
Physical	
molecular weight, μ_0 (amu)	28.01
refractivity, ν_{STP} (10^{-4})	2.980
Clear Atmosphere	
temperature, T_0 (K)	99.2±8.07
temperature gradient, $(dT/dr)_0$ (K km^{-1})	-0.049±0.066
number density n_0 (10^{14} cm^{-3})	0.88±0.16
pressure, p_0 (μbar)	1.20±0.25
column height, ξ_0 (cm-A)	19.8±4.1
number density n_1 (10^{14} cm^{-3})	1.627±0.060
pressure, p_1 (μbar)	2.268±0.217
column height, ξ_1(cm-A)	35.3±3.3
haze, no steep thermal gradient	
surface number density, n_s (10^{14} cm^{-3})	>=3.1
surface pressure, p_s (μbar)	>=4.5
surface column height, ξ_s (cm-A)	>=64
τ_{obs} = 1 radius, r_2 (km)	1204 ± 22
steep thermal gradient, no haze	
surface number density, n_s (10^{14} cm^{-3})	>= 3.9
surface pressure, p_s (μbar)	>=2.8
surface column height, ξ_s (cm-A)	>=40

Previous determinations of Pluto's radius under the "steep thermal gradient, no haze" model did not allow for the possibility that the atmosphere was at vapor-pressure

equilibrium anywhere except the surface. This put the surface where the atmospheric pressure first equaled the saturation vapor pressure. For an N_2 atmosphere, this implies a surface radius of 1195 – 1205 km and a temperature of 35 K. We now take this radius as an upper limit, because it is possible that the atmosphere reaches saturation at 35 K and remains at saturation until it reaches the surface.

5.3.2 ATMOSPHERIC METHANE

The absorption from Pluto was modeled as a single-temperature atmosphere at 100 K. From this we find a two-pass CH_4 abundance. This is at least twice as large as the column height, because the solar flux transverses the atmosphere twice (once on the way into the atmosphere, and once after the light is reflected off the surface). Dividing by the airmass factor corrects for this, and for the longer pathlengths near Pluto's limb. As discussed in Chapter 4, the model does not agree with the data at 1665.8 nm, and the resolution of this disagreement will probably increase the CH_4 abundance and decrease the relative errors.

Table 5.9. Results from Chapter 4.

parameter	$T = 100$
two-pass CH_4 abundance (cm-A)	$4.81^{+12.60}_{-3.48}$
airmass factor (assumed)	4
CH_4 column height, ξ_{CH_4} (cm-A)	$1.20^{+3.15}_{-0.87}$
fit information	
degrees of freedom	226
χ^2	258

The molar mixing ratio of CH_4 may not be constant with height. However, the mean molar mixing ratio of CH_4 can be found by dividing the CH_4 column height, ξ_{CH_4}, by the total atmospheric column height. We can assume that the atmosphere is mostly N_2, so we divide ξ_{CH_4} by the N_2 column height, ξ_{N_2}, to find the vertical mean CH_4 mixing ratio.

This is compared with the CH_4 mixing ratio calculated from vapor-pressure equilibrium using Eq. (5.5), in Table 5.10. The pressures and the CH_4 vapor-pressure equilibrium mixing ratios are from Owen *et al.* (Owen *et al.* 1993).

Table 5.10. CH_4 molar mixing ratios.

	$T = 34$	$T = 45$	$T = 58$
surface pressure (μbar)	1.2	590	3.8×10^4
N_2 column height (cm-A)	19.8	9.7×10^3	6.3×10^5
vapor-pressure equilibrium CH_4 molar mixing ratio	9×10^{-7}	9×10^{-6}	5×10^{-5}
observed vertical mean CH_4 molar mixing ratio	6×10^{-2}	1×10^{-4}	2×10^{-6}

The Yelle and Lunine (1989) CH_4 heating model required an atmospheric mixing ratio of at least 0.1% CH_4. Vapor-pressure equilibrium predicts a CH_4 molar mixing ratio that is much lower than this 0.1% limit. The observed mean mixing ratio is high enough to heat the middle atmosphere in the low temperature case. In the other cases, the observed mixing ratio is too low, if the mixing ratio is constant with altitude.

5.4 LOWER ATMOSPHERE

There are no direct observations of the lower atmosphere, but we can constrain the atmospheric structure by boundary conditions with the surface and middle atmosphere. The pressure and temperature must match that of the middle atmosphere at the transition radius, and the surface must be in vapor-pressure equilibrium with the lower atmosphere. Between these two boundaries, the lower atmosphere will be in hydrostatic equilibrium. A further constraint is that lapse rate ($-dT/dr$) cannot exceed the dry adiabatic lapse rate:

$$-\frac{dT}{dr} \leq \frac{g}{C_p} \tag{5.8}$$

where C_p is the specific heat at constant pressure. If C_p for N_2 at Pluto's temperature is near that of N_2 at 300 K, then the lapse rate is 0.5 K km^{-1}.

We assume that N_2 cannot be supersaturated in the atmosphere. This requires that the pressure (p) cannot exceed its saturation vapor pressure (P_{sat})

$$p(T) \leq P_{sat}(T) \tag{5.9}$$

5.5 CONNECTING THE MIDDLE ATMOSPHERE TO THE SURFACE

To find the reasonable range of surface radii and temperature and pressure profiles that are consistent with the stellar occultation and with vapor-pressure equilibrium, we consider the variation of pressure with temperature, $p(T)$ (Fig. 5.2). In the middle atmosphere, the profile is essentially isothermal at 99.2 ± 8.1 K until the transition radius (marked with an "*O*" in Fig. 5.2), at a pressure of 2.27 ± 0.22 μbar. At that point, the kink in the occultation light curve could be caused by refraction only or by a haze layer. The pressures and temperatures at which the star was last detected in the occultation light curve are 2.8 μbar and 50 K for the refractive case ("*E*") and 4.5 μbar and 99 K in the haze case ("*F*"). For the haze solution, $p(T)$ starts at *F*; for the refraction solution, it starts at *E*. Intermediate solutions start between these two points.

The surface is in vapor-pressure equilibrium with the atmosphere. Therefore, the surface must lie on the saturation vapor pressure curve, $P_{sat}(T)$. The temperatures measured by Pluto's thermal emission, 30 K < T_s < 55 K (Sykes *et al.* 1987; Tedesco *et al.* 1987; Altenhoff *et al.* 1988; Jewitt 1993; Stern *et al.* 1993), is shown as a slightly thick line on the saturation vapor pressure curve. The thicker line at T_s = 40 ± 2 K represents the determination of the frost temperature by Tryka *et al.* (1994).

For a given surface temperature, there are several paths connecting the middle atmosphere (from *E* or *F*) to the surface (at *S*), each of which lead to different thermal structures and surface radii. For each surface temperature, we calculate the surface radii for

four paths. Path a is the cold refractive path; path b is the warm refractive path; path c is the cold haze path, and path d is the warm haze path.

The point E has a radius of r_E, a pressure of p_E, and a temperature of T_E. Similarly, points F and S have radii r_F and r_S, pressures of p_F and p_S, and temperatures of T_F and T_S respectively. For each point we also define scaled altitudes z_E, z_F, and z_S, where

$$z = -\ln p \tag{5.10}$$

For a given surface temperature and starting point (E or F), the only unknown is r_S. This can be found by specifying T as a function of p or z.

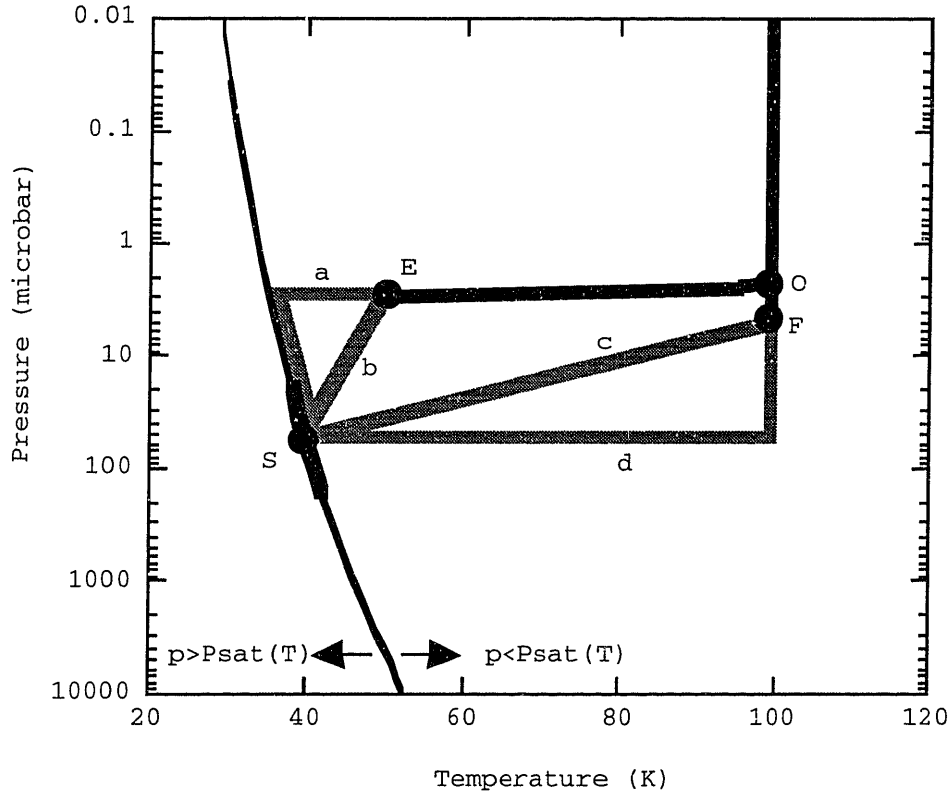

Figure 5.2. Pressure-temperature paths through the lower atmosphere. The gray paths *a*, *b*, *c*, and *d* are possible structures for the lower atmosphere that can connect the surface (*S*) to the observed pressures and temperatures of the middle atmosphere (in black, ending at *E* for the refraction-only solution to the occultation, *F* for the haze solution). The saturation vapor pressure, $P_{sat}(T)$, is plotted. The surface must lie on this line. We assume N_2 cannot be supersaturated in the atmosphere, so paths must lie to the right of this line.

Path *a* has two legs. The first leg proceeds at a constant pressure (and radius) from $\{T_E, p_E\}$ until it reaches the saturation temperature at $\{T_{sat}, p_E\}$, where $P_{sat}(T_{sat}) = p_E$. The actual atmosphere will have some finite thermal gradient, but this is a reasonable characterization of the 30 K km^{-1} slopes required by Stansberry *et al.* (1994). The path then proceeds from $\{T_{sat}, p_E\}$ to $\{T_S, p_S\}$ along the saturation curve. For paths *b* and *c*, the temperature is a linear function of z. Path *d* consists of an isothermal leg from $\{p_F, T_F\}$ to $\{p_S, T_F\}$, and a leg at constant pressure, from $\{p_S, T_F\}$ to $\{p_S, T_S\}$.

These paths satisfy the conditions discussed in 5.4: continuity (by connecting E or F to S); vapor pressure equilibrium (by situating S on the vapor-pressure curve); $p(T) \leq P_{sat}(T)$ (by not crossing the vapor-pressure curve); and not exceeding the dry adiabatic (which is five times steeper than the vapor-pressure curve). Other paths satisfy these conditions, if we allow paths with local maxima of temperature in the lower atmosphere. For example, a path could start at E, follow path a to the vapor-pressure curve, then depart from that curve at the dry adiabatic lapse rate until it reaches path c, where it returns to the surface at S along path c. Such paths are not considered here. Until there is evidence for these zigzag thermal profiles, we will assume that the structure of the lower atmosphere under the "no haze, steep thermal gradient" model fall between paths a and b, and that the structure of the lower atmosphere under the "haze, no steep thermal gradient" model fall between paths c and d.

To find the surface radii, we specify dT/dz and apply hydrostatic equilibrium

$$\frac{dz}{dr} = \frac{1}{H} = \frac{\mu m_{amu} g(r)}{kT} \tag{5.11}$$

and then integrate from the surface to E or F.

For path a, we use the Clausius-Clapeyron equation

$$\frac{dp}{dT} = \frac{pL\mu m_{amu}}{kT^2} \tag{5.12}$$

where L is the latent heat of sublimation. Eq. (5.12) can be expressed as

$$\frac{dT}{dz} = -\frac{kT^2}{L\mu m_{amu}} \tag{5.13}$$

The surface radius is found by multiplying Eqs. (5.11) and (5.13), then integrating the temperature from T_S to T_{sat} and the radius from r_S to r_E.

$$r_S = r_E\left[1+\frac{L}{g_E r_E}\ln\left(T_S/T_{sat}\right)\right]^{-1}, \text{ path } a \tag{5.14}$$

Along path b, the temperature depends linearly on z.

$$\frac{dT}{dz} = \Gamma = \frac{T_E - T_S}{z_E - z_S} \tag{5.15}$$

We multiply Eqs. (5.11) and (5.15)

$$\frac{dT}{dr} = \Gamma\frac{\mu m_{amu} g_R r_R^2}{kTr^2} \tag{5.16}$$

This can be integrated from S to E or F to give the radius as a function of temperature. The result is

$$r_S = r_E\left[1+(z_E - z_S)\frac{T_S + T_E}{2}\frac{k}{\mu m_{amu} g_E r_E}\right]^{-1}, \text{ path } b \tag{5.17}$$

The surface radius following path c can be found analogously,

$$r_S = r_F\left[1+(z_F - z_S)\frac{T_S + T_F}{2}\frac{k}{\mu m_{amu} g_F r_F}\right]^{-1}, \text{ path } c \tag{5.18}$$

For path d, we only integrate along the vertical leg.

$$r_S = r_F\left[1+(z_F - z_S)T_H\frac{k}{\mu m_{amu} g_F r_F}\right]^{-1}, \text{ path } d \tag{5.19}$$

Colder atmospheres have smaller scale heights. Thus, for any given surface temperature, path a leads to larger radii than path b, and pa: : leads to leads to larger radii than path d. To find the ranges of consistent radii for each starting point, we chose the radii, temperatures, and pressures at E and F to maximize the surface radius for paths a and c and to minimize the surface radius for paths b and d. From the nominal values, the

pressures are increased or decreased by the error in p_0 (0.25 μbar); the temperatures at F are increased or decreased by the error in T_0 (8 K); the temperatures at E are increased or decreased by half the error in T_0 (4 K); and the radii are increased or decreased by the error in r_1 (11 km). For a and c, we maximize r and p , and minimize T. Maximizing p_E for a minimizes T_{sat}. For paths b and d, we minimize r and p, and maximize T. These values are listed in Table 5.11. The surface pressure must be at least the pressure of the starting condition (p in Table 5.11). The surface temperature, T_s, must be greater than the saturation temperature for that pressure.

Table 5.11. Starting conditions for pressure-temperature paths.

path	r (km)	T (K)	p (μbar)	T_s (K)	k / ($\mu m_{amu} gr$) (K^{-1})	L / (gr)
a	1217	46	3.1	>35.2	–	0.372
b	1195	54	2.5	>34.9	4.294×10^{-4}	–
c	1192	91	4.8	>35.8	4.283×10^{-4}	–
d	1170	107	4.2	>35.6	4.204×10^{-4}	–

For each path, the surface radius was found for temperatures between the minimum surface temperature, T_s, and the maximum observed frost temperature of 55K. The results are shown in Fig. 5.3. The left-hand end of each curve is the minimum allowable frost temperature for that curve.

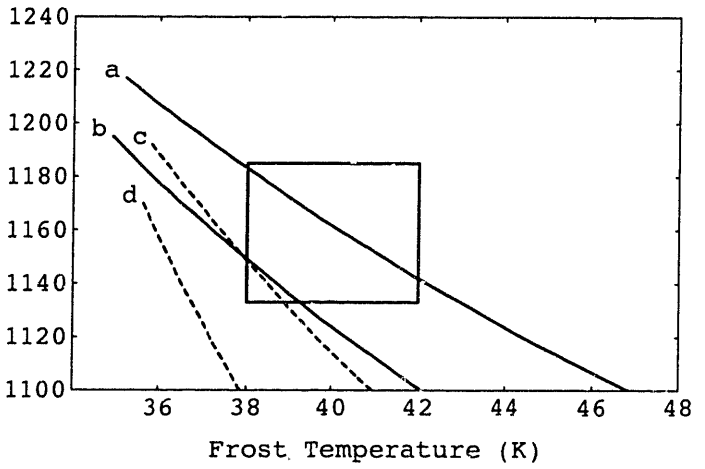

Figure 5.3. Surface radii as a function of surface temperature. Surface radii that can be in vapor-pressure equilibrium with an N_2 atmosphere and match the temperature and pressures determined from the 1988 KAO stellar occultation are plotted as a function of surface temperature. Surface radii derived for a purely refractive atmosphere lie between lines *a* and *b*. Surface radii derived for an atmosphere with no steep temperature inversion lie between lines *c* and *d*. Intermediate cases lie between curves *a* and *d*. The box indicates the mutual-event determinations of the visible-limb radius (Buie *et al.* 1992; E. Young and Binzel 1994) and frost temperature from N_2 line shapes (Tryka *et al.* 1994). Note that this temperature range is much narrower than the range of temperatures represented by the box in Fig. 5.1.

The height of the box in Figs. 5.3 and 5.4 indicates the mutual-event determinations of the radius of the visible limb, ranging from 1140± 7 km (Buie *et al.* 1992) to 1165 ± 23 km (E. Young and Binzel 1994). The width of the box indicates the frost temperatures of 40 ± 2 K derived from the shape of the N_2 band (Tryka *et al.* 1994). The frost temperatures derived from thermal emission range from 30 – 55 K (Sykes *et al.* 1987; Tedesco *et al.* 1987; Altenhoff *et al.* 1988; Jewitt 1993; Stern *et al.* 1993), and extend beyond the bounds of the figure.

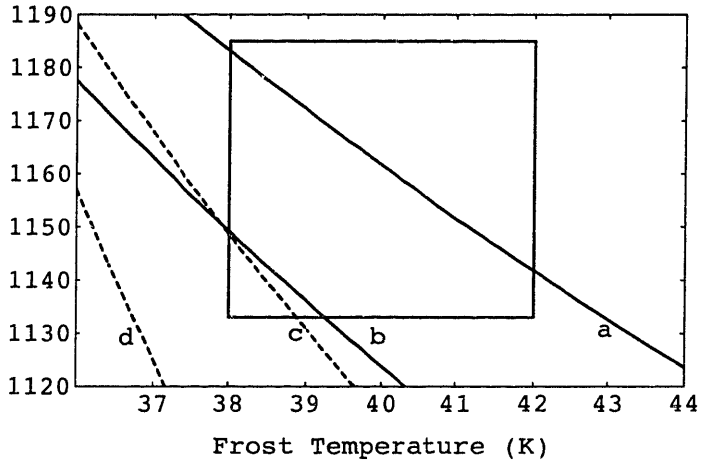

Figure 5.4. Surface radii as a function of surface temperature (expanded). This figure is the same as Fig. 5.3, at a larger scale.

5.6 DISCUSSION

The allowable combinations of surface radii and frost temperature for the "no haze" model lies between curves *a* and *b* in Figs. (5.3) and (5.4), while those for the "haze" model lie between curves *c* and *d*. The implications are summarized in Table 5.12.

Table 5.12. Pluto's surface and density.

	steep thermal gradient, no haze		no steep thermal gradient, haze	
Constraints				
frost temperature, T_S (K)	30 – 55	38 – 42	30 – 55	38 – 42
surface radius, r_S (km)	1133 – 1185	1133 –1185	1000 – 1185	1000 – 1185
Results				
frost temperature, T_S (K)	35.5 – 43	38 – 42	35.6 –50	38 – 42
surface radius, r_S (km)	1133 –1185	1133* – 1183	1000 – 1185	1005 – 1149
surface pressure, p_S (μbar)	3.9 –397.1	18.8 –158.7	4.2 – 3953.2	18.8 – 158.7
surface column height, ξ_S (cm-A)	64 – 6553	310 –2619	69 – 65229	310 – 2619
bulk density, ρ_p (g cm^{-3})	1.64 – 2.03	1.79 –2.03	1.75 – 3.00	1.95 – 2.91

*The lower limit, independent of the mutual event data, is 1100 km.

The frost temperatures observed from Pluto's thermal emission (30 K –55 K) do not constrain the structure of the lower atmosphere or the surface radius. Rather, the limits on the radii place constraints on surface temperature. If there is no extinction, the visible limb

of Pluto detected by the mutual-events must be Pluto's surface. This lower limit on the radius constrains the frost temperature to be less than 44 K. If there is extinction, the radius must be larger than 1000 km to keep the density greater than 3.0 g cm^{-3}, the density of Pluto's rock component (McKinnon and Mueller 1988). This density constraint is violated for temperatures greater than 50 K. Therefore, the limits on the surface temperature is 35 – 50 K for the haze model (Table 5.12, column #4), and 35 – 43 K for the no-haze model (Table 5.12, column #2).

If the frost temperature is 40 ± 2 K (Tryka *et al.* 1994), we can again consider the hazy and clear cases separately. In the haze case (Table 5.12, column #5), the largest allowable radius is 1149 km, where curve *c* in Fig. 5.4 crosses 38 K, and the smallest allowable radius is 1005 km, where curve *d* crosses 42 K. In the no-haze case (Table 5.12, column #3), the largest allowable radius is 1183 km, where curve *a* in Fig. 5.4 crosses 38 K, and the smallest allowable radius can be taken to be either 1100 km, where curve *b* crosses 42 K, or 1133 km, the lower limit on the mutual-event radius. Since limits on the radius had already restricted the range of allowed surface temperatures to 35.5 –43 K in the no-haze case, narrowing the temperature range by a few degrees adds little new information about the radius. However, narrowing the range by just a few degrees greatly decreases our uncertainty in the surface pressure, since the pressure is a steep function of temperature. Given the temperatures derived from thermal emission, the pressures can range over 2 or 3 orders of magnitude; with the temperature range 40 ± 2, they are known within a factor of ten.

The "no haze, thermal gradient" radii and temperatures are consistent with near-surface thermal gradients from –0.11 K km^{-1} to 0.35 K km^{-1}. This allows, but does not require, a troposphere along the lines suggested by Stansberry *et al.* (1994). Such a troposphere would have a minimum temperature of 35 K and a maximum temperature of 44 K.

The Pluto radii that are calculated from a frost temperature of 40 ± 2 K are converted to densities, and compared with Charon's density in Table 5.13. If one uses the maximum radius consistent with Pluto's stellar occultation, the system density is 1.79 g cm^{-3} and the silicate mass fraction is ~0.6. If one uses radii of 1140 ± 7 km, the system density is 2.03 ± 0.03 g cm^{-3} and the silicate mass fraction is ~0.7. Triton and Pluto-Charon were probably both formed in the outer solar nebula, about 30-50 AU from the sun, and therefore probably had the same silicate mass fraction at formation. Triton has a density of 2.07 ± 0.02 g cm^{-3} (Smith *et al.* 1989), for a silicate mass fraction near 0.7. Predictions for the mass fraction at the time of formation range from 0.7 (Anders and Ebihara, 1982) down to 0.5-0.6 (Anders and Grevesse 1989; Grevesse *et al.* 1991). Subsequent to formation, Triton and the Pluto-Charon system had very different dynamical and thermal histories; Triton was captured by Neptune and Pluto-Charon probably experienced a cataclysmic event associated with the formation of Charon. Scenarios for the histories of Triton and the Pluto-Charon system thus appear to fall into one of three broad categories: (i) both were formed with a density near 2.0 g cm^{-3} and neither lost much ice, (ii) both were formed with a density near 1.7 g cm^{-3} and both lost a large fraction of their ice, and (iii) both were formed with a density near 1.7 g cm^{-3} and only Triton lost a large fraction of its ice.

Table 5.13: Bulk properties for Pluto and Charon

	Stellar-occultation radii (T_S = 40 ± 2 for Pluto)		Mutual-event radii	
	clear	haze	TB90	E. Young & Binzel 1994
Pluto density, ρ_p (g cm^{-3})	1.79 – 2.03*	1.95 – 2.91	1.99 ± 0.03	1.80 ± 0.02
Charon density, ρ_c (g cm^{-3})	<2.22		2.28 ± 0.17	1.79 ± 0.05

Note· The lower limit, independent of the mutual event data, is 2.22 g cm^{-3}.

CHAPTER 6
CONCLUSIONS

Since Pluto's surface is likely to be in vapor-pressure equilibrium with its N_2 atmosphere, the atmospheric structure and bulk properties of Pluto depend largely on the temperature of the surface frost.

Warm Pluto. For warm frost temperatures (T_s = 45 K), the surface pressure would be 608 μbar. Since the transition radius is at 2.5 μbar, the surface would be 100 – 200 km below the transition radius. Regardless of what causes the transition, the surface is at a radius less than 1100 km, for a density greater than 2.2 g cm^{-2}. This puts the surface well below the mutual-event radii (Fig. 6.1). In this case, the mutual-events must detect a visible-limb radius, rather than a surface.

If the transition radius marks the onset of a haze (right-hand profile), the atmosphere would have a gentle thermal gradient of 0.3 K km^{-1} between the transition radius and the surface. The haze model implies a haze that reaches a vertical optical depth of 0.145 by a radius of 1180 km. This haze could not extend the remaining 150 km to the surface, or else it would obscure the albedo variation seen on Pluto's surface. The radii are less than 1050 km and the densities are greater than 2.5 g cm^{-3}.

If the transition marks a steep thermal gradient (left-hand profile), then the surface would lie below the mutual-event radius, and a low-altitude haze layer would be needed to explain the mutual event radius.

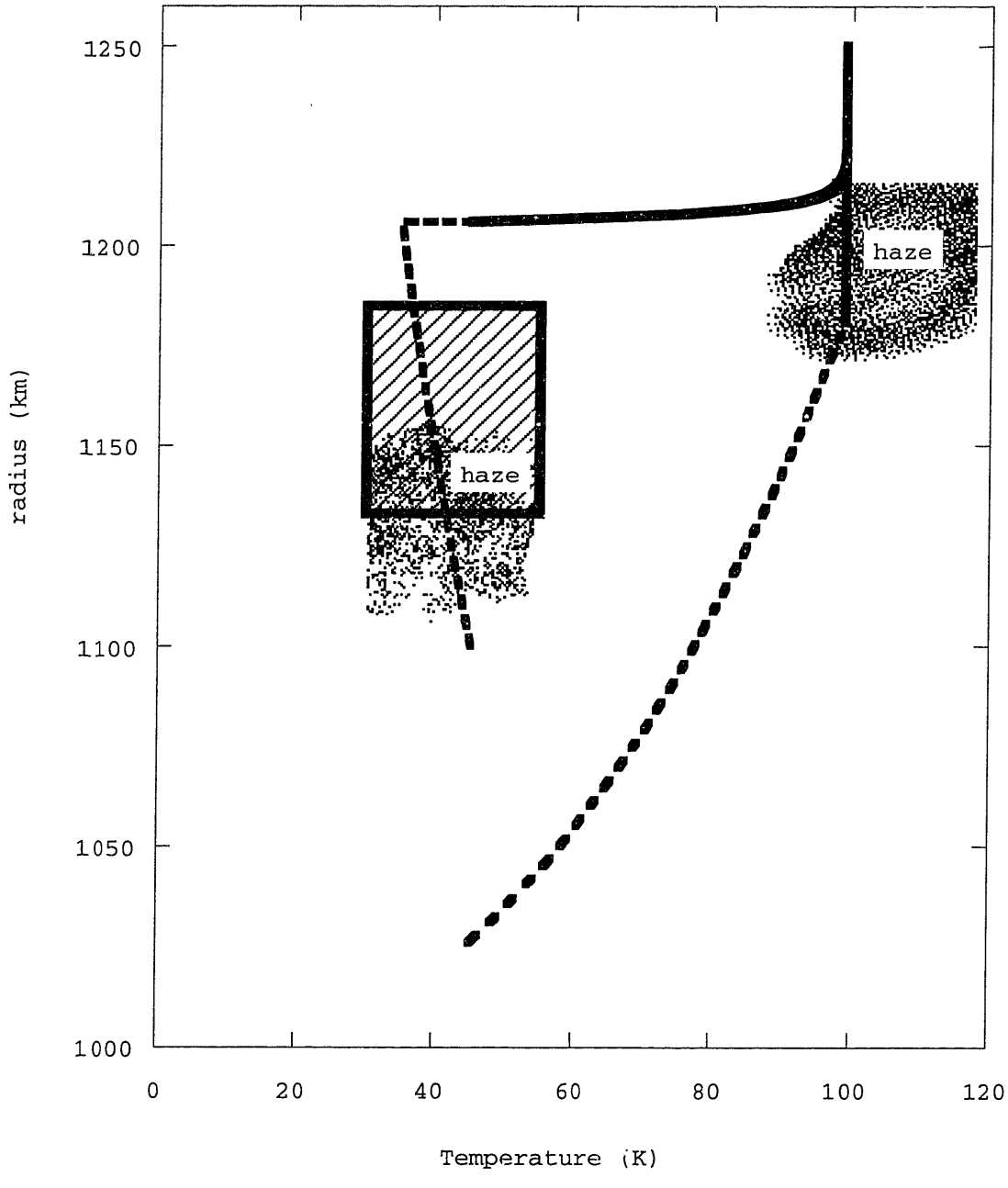

Figure 6.1. Possible profiles for a frost temperature of 45 K. The solid line represents radii probed by the stellar occultation. The box represents the range of reported values for the radius of visible limb (Buie *et al.* 1992; E. Young and Binzel 1994) and temperature of the surface (see Jewitt 1993, for a review). The dotted lines show possible thermal profiles for a surface temperature of 45 K. Note that the surface lies below the mutual-event radii, implying that the mutual events did not detect the surface.

Cold Pluto. For cold frost temperatures (T= 35 K), the surface pressure would be 2.7 μbar. This is near the surface pressure at the transition radius, so the surface would lie immediately below the transition, at a radius near 1200 km (Fig. 6.2). A steep thermal gradient below the transition radius would end at the surface, with no intervening troposphere. A cold Pluto thus implies a large radius, and a density near 1.7 g cm^{-3}. The radius that the star was last observed in the "haze, no steep thermal gradient" solution to Pluto's occultation light curve is at a pressure greater than 2.7 μbar, so the haze model is incompatible with frost temperatures of 35 K. If the temperature is 36 K, the haze model would have to overlie a steep inversion layer that begins near 1180 km.

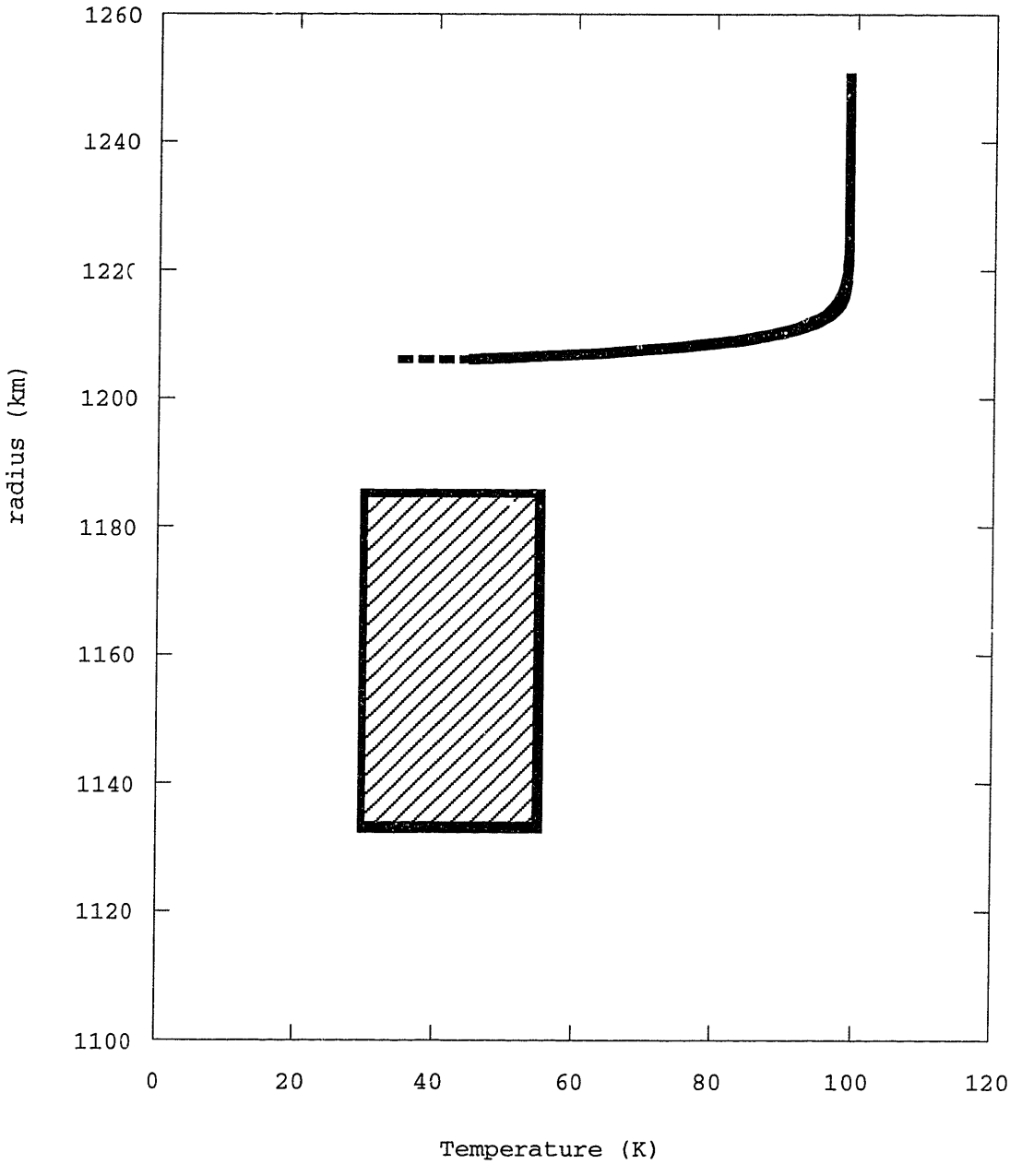

Fig. 6.2. Possible profiles for a frost temperature of 35 K. The solid line and the box have the same meaning as in Fig. 6.1. Note that the haze interpretation of the occultation is inconsistent with a surface at 35 K.

Just-Right Pluto. For intermediate frost temperatures (T = 40 K), the surface pressure would be 58 μbar. Under the haze model, the surface would lie about 100 km below the transition radius, and the thermal gradient in the lower atmosphere would be about 0.5 K km^{-1}. The depth of the lower atmosphere can range from 77 – 125 km, depending on the average temperature of the atmosphere between the transition radius and the surface. In either the haze or the refractive case, the densities would have values of 2.1 –2.6 g cm^{-3}.

For the purely refractive solution, the depth of the lower atmosphere is 55 to 70 km, depending on the mean temperature of the lower atmosphere. For the shallowest lower atmosphere (and the largest radius), a troposphere is required. This troposphere would have a minimum temperature near 35 K, immediately below the transition radius. The atmosphere would be at saturation at this point, and remain in saturation down to the surface, for a negative thermal gradient of –0.12 K cm^{-1}. In this troposphere case, the surface lies above or on the mutual-event radii, for densities near 1.8 – 2.0 g cm^{-3}. Alternatively, the atmosphere can have a steep thermal gradient until about 40 – 50 K, and then proceed isothermally to the surface. The lower atmosphere is deeper in this case than in the troposphere case. If there is no atmospheric extinction, the mutual-event radius of 1140 ± 7 km is a lower limit to the surface. Otherwise, the surface lies just below a near-surface haze, at about 1110 km.

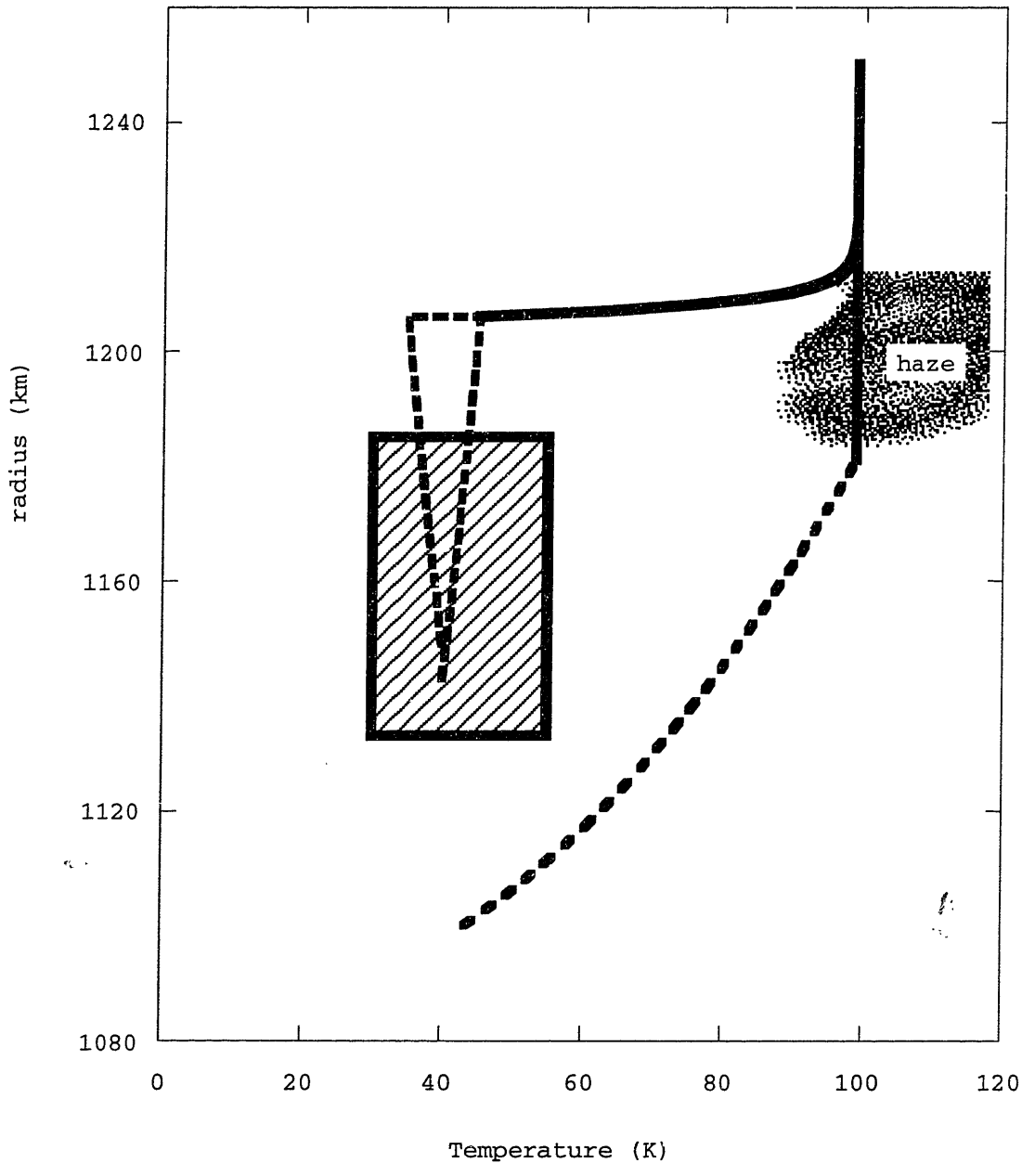

Fig. 6.3. Possible profiles for a frost temperature of 40 K. The solid line and the box have the same meaning as in Fig. 6.1. The dotted line shows a possible thermal profile for a surface temperature of 40 K. Note that a surface of 40 K is consistent with a deep, hazy atmosphere, a troposphere, and a cold lower atmosphere with a positive thermal gradient.

The above structures predict different surface temperatures, atmospheric temperatures, surface radii, and optical depths. Additional constraints on any of these would help differentiate between the various atmospheric structures. Measuring the temperature-dependent shape of spectral lines has the advantage that we know we are measuring the frost temperature, not some global mean temperature. However, it does not provide information on the frost-free regions of Pluto and Charon. This information can be measured in the thermal IR. ISO and SOFIA will allow access to thermal-IR wavelengths unavailable from the ground. Atmospheric temperatures can be measured from the relative strengths of vibration-rotation lines similar to those described in Chapter 4. A major source of uncertainty in the mutual-event radii arises from the uncertainty in Charon's contribution to the total signal during the mutual events (E. Young and Binzel 1994). Individual light curves of the two bodies will help decrease the error these radii. This may be a difficult observation, since the rotational phase at which the mutual events occur is the phase of least separation. Stellar occultations observed simultaneously in the visible and IR will probe the optical depth of Pluto's atmosphere.

REFERENCES

Acton, C. H., Jr. 1990. *The SPICE concept: An approach to providing geometric and other ancillary information needed for interpretation of data returned from space science instruments*. AIAA/NASA Second International Symposium on Space Information Systems, JPL (Pasadena, CA), pp 1029-1052.

Anders, E., and M. Ebihara 1982. Solar-system abundances of the elements. *Geochim. Cosmochim. Acta* **46**, 2363-2380.

Anders, E., and N. Grevesse 1989. Abundances of the elements: meteoritic and solar. *Geochim. Cosmochim. Acta* **53**, 197-214.

Altenhoff, W. J., R. Chini, H. Hein, E. Kreysa, P. G. Mezger, C. Salter, and J. B. Schraml 1988. First radio astronomical estimate of the temperature of Pluto. *Astron. Astrophys.* **190**, L15-L17.

Apt, J., N. P. Carleton, and C. D. Mackay 1983. Methane on Triton and Pluto: New CCD spectra. *Astrophys. J.* **270**, 342-350.

Aumann, H. H., and R. G. Walker 1987. IRAS observations of the Pluto-Charon system. *Astron. J.* **94**, 1088-1091.

Bates, D. R. 1959. Some problems concerning the terrestrial atmosphere above about 100 km. *Proc. Roy. Soc. London Ser. A* **253**, 451-462.

Barker, E. S., W. D. Cochran, and A. L. Cochran 1980. Spectrosphotometry of Pluto from 3500 to 7350 Å. *Icarus* **44**, 43-52.

Baum, W. A., and A. D. Code 1953. A photometric observation of the occultation of σ Arietis by Jupiter. *Astron. J.* **58**, 108-112.

Beletic, J. W., R. M. Goody, and D. J. Tholen 1989. Orbital elements of Charon from speckle interferometry. *Icarus* **79**, 38-46.

Benner, D. C., U. Fink, and R. H. Cromwell 1978. Image tube spectra of Pluto and Triton from 6800 to 9800 Å. *Icarus* **36**, 82-91.

Binzel, R. P., D. J. Tholen, E. F. Tedesco, B. J. Buratti, and R. M. Nelson 1985. The detection of eclipses in the Pluto-Charon system. *Science* **228**, 1193-1195.

Buie, M. W., and D. J. Tholen 1989. The surface albedo distribution of Pluto. *Icarus* **79**, 23-37.

Buie, M. W., D. P. Cruikshank, L. A. Lebofsky, and E. F. Tedesco 1987. Water frost on Charon. *Nature* **329**, 522-523.

Buie, M. W., D. J. Tholen, and K. Horne 1992. Albedo maps of Pluto and Charon: Initial mutual event results. *Icarus* **97**, 221-227.

Campins, H., G. H. Rieke, and M. J. Lebofsky 1985. Absolute calibration of photometry at 1 through 5 μm. *Astron. J.* **90**, 896 - 899.

Cruikshank, D. P., and P. M. Silvaggio 1980. The surface and atmosphere of Pluto. *Icarus* **41**, 96-102.

Cruikshank, D. P., C. B. Pilcher, and D. Morrison 1976. Pluto: Evidence for methane frost. *Science* **194**, 835-837.

Dunham, E. W., S. W. McDonald, and J. L. Elliot 1991. Pluto-Charon stellar occultation candidates: 1990-1995. *Astron. J.* **102**, 1464-1484.

Eichhorn, H. 1974. *Astrometry of star positions*. Frederick Ungar Publishing Co., N. Y.

Elliot, J. L., and L. A. Young 1991. Limits on the radius and a possible atmosphere of Charon from its 1980 stellar occultation. *Icarus* **89**, 244-254.

Elliot, J. L., and L. A. Young 1992. Analysis of stellar occultation data for planetary atmospheres. I. Model fitting, with application to Pluto. *Astron. J.* **103**, 991-1015.

Elliot, J. L., E. W. Dunham, A. S. Bosh, S. M. Slivan, L. A. Young, L. H. Wasserman, and R. L. Millis 1989. Pluto's atmosphere. *Icarus* **77**, 148-170.

Eshleman, V. R. 1989. Pluto's atmosphere: Models based on refraction, inversion, and vapor-pressure equilibrium. *Icarus* **80**, 439-443.

Fink, U., and M. A. DiSanti 1988. The separate spectra of Pluto and its satellite Charon. *Astron. J.* **95**, 229-236.

Fink, U., B. A. Smith, D. C. Benner, J. R. Johnson, H. J. Reitsema, and J. A. Westphal 1980. Detection of a CH_4 atmosphere on Pluto. *Icarus* **44**, 62-71.

Goldsmith, D. W. 1963. Differential refraction in planetary atmospheres with linear scale height gradients. *Icarus* **2**, 341-349.

Grevesse, N., D. L. Lambert, and A. J. Sauval 1991. Vibration-rotation bands of CH_4 in the solar infrared spectrum and the solar carbon abundance. *Astron. Astrophys.* **242**, 488-495.

Green, R. M. 1985. *Spherical Astronomy*. Cambridge University Press, Cambridge.

Grundy, W. M., B. Scmitt, and E. Quirico 1993. The temperature dependent spectra of α and β nitrogen ice with application to Triton. *Icarus* (submitted).

Hardorp, J. 1978. The sun among the stars. I. A search for solar spectral analogs. *Astron. Astrophys.* **63**, 383-390.

Høg, E., and J. von der Heide 1976. Perth 70 catalog. *Abh. Hamburg. Sternw.* **9**.

Holman, M. J. 1991. *Infrared emission from Pluto's atmosphere*, General Examination Paper. Massachusetts Institute of Technology.

Hubbard, W. B., R. V. Yelle, and J. I. Lunine 1990. Nonisothermal Pluto atmosphere models. *Icarus* **84**, 1-11.

Ingersoll, A. P. 1990. Dynamics of Triton's atmosphere. *Nature* **344**, 315-317.

Jewitt, D. C. 1993. Heat from Pluto. *Astron. J.* **107**, 372-378.

Jones, J. H., C. A. Christian, and P. Waddell 1988. Resolved CCD photometry of Pluto and Charon. *Publ. Astron. Soc. Pacific* **100**, 489-495.

Khalil, M. A. K., R. A. Rasmussen, and F. Moraes 1993. Atmospheric methane at Cape Meares: Analysis of a high-resolution data base and its environmental implications. *Journal of Geophysical Research* **98**, 14753-14770.

King, I. R. 1983. Accuracy of measurement of star images on a pixel array. *Publ. Astron. Soc. Pacific* **95**, 163-168.

Lebofsky, L. A., and J. R. Spencer 1989. Radiometry and thermal modeling of asteroids. In *Asteroids II* (R. P. Binzel, T. Gehrels and M. S. Matthews, Ed.), pp. 128-147. The University of Arizona Press, Tucson.

Lewis, J. S. 1972. Low temperature condensation from the solar nebula. *Icarus* **16**, 241-252.

Livingston, W., and L. Wallace 1991. *An atlas of the solar spectrum in the infrared from 1850 to 9000 cm^{-1} (1.1 to 5.4 microns)*, NSO Technical Report #91-001. National Solar Observatory, NOAO, Tucson.

Lord, S. D. 1992. *A new software tool for computing Earth's atmospheric transmission of near- and far-infrared radiation*, NASA TM-103957. Ames Research Center.

Marcialis, R. L., and L. A. Lebofsky 1990. CVF spectrophotometry of Pluto: Correlation of composition with albedo. *Icarus* **89**, 255-263.

Marcialis, R. L., G. H. Rieke, and L. A. Lebofsky 1987. The surface composition of Charon: Tentative identification of water ice. *Science* **237**, 1349-1351.

Marsden, B. G. 1989. *Minor Planet Circular*, 14768.

McKinnon, W. B. 1989. On the origin of the Pluto-Charon binary. *Astrophys. J. (Letters)* **344**, L41-L44.

McKinnon, W. B., and S. Mueller 1988. Pluto's structure and composition suggest origin in the solar, not a planetary, nebula. *Nature* **335**, 240-243.

Millis, R. L., L. H. Wasserman, O. G. Franz, R. A. Nye, J. L. Elliot, E. W. Dunham, A. S. Bosh, L. A. Young, S. M. Slivan, A. C. Gilmore, P. M. Kilmartin, W. H. Allan, R. D. Watson, S. W. Dieters, K. M. Hill, A. B. Giles, G. Blow, J. Priestly, W. M. Kissling, W. S. G. Walker, B. F. Marino, D. G. Dix, A. A. Page, J. E. Ross, H. P. Avey, D. Hickey, H. D. Kennedy, K. A. Mottram, G. Moyland, T. Murphy, C. C. Dahn, and A. R. Klemola 1993. Pluto's radius and atmosphere: Results from the entire 9 June 1988 occultation data set. *Icarus* **105**, 282-297.

Mink, D. J., A. R. Klemola, and M. W. Buie 1991. Occultations by Pluto and Charon: 1990-1999. *Astron. J.* **101**, 2255-2261.

Null, G. W., W. M. Owen, and S. P. Synnott 1993. Masses and densities of Pluto and Charon. *Astron. J.* **105**, 2319-2335.

Olkin, C. B., L. A. Young, J. L. Elliot, D. T. Tholen, and M. W. Buie 1993. Individual light curves of Pluto and Charon. *Bull. Amer. Astron. Soc.* **25**, 1132-1133.

Owen, T. S., T. L. Roush, D. P. Cruikshank, J. L. Elliot, L. A. Young, C. de Bergh, B. Schmitt, T. R. Geballe, R. H. Brown, and Bartholomew 1993. Surface ices and the atmospheric composition of Pluto. *Science* **261**, 745-748.

Smith, B. A., L. A. Soderblom, D. Banfield, C. Barnet, A. T. Basilevksy, R. F. Beebe, K. Bollinger, J. M. Boyce, A. Brahic, G. A. Briggs, R. H. Brown, C. Chyba, S. A. Collins, T. Colvin, A. F. Cook II, D. Crisp, S. K. Croft, D. Cruikshank, J. N. Cuzzi, G. E. Danielson, M. E. Davies, E. De Jong, L. Dones, D. Godfrey, J. Goguen, I. Grenier, V. R. Haemmerle, H. Hammel, C. J. Hansen, C. P. Helfenstein, C. Howell, G. E. Hunt, A. P. Ingersoll, T. V. Johnson, J. Kargel, R. Kirk, D. I. Kuehn, S. Limaye, H. Masursky, A. McEwen, D. Morrison, T. Owen, W. Owen, J. B. Pollack, C. C. Porco, K. Rages, P. Rogers, D. Rudy, C. Sagan, J. Schwartz, E. M. Shoemaker, M. Showalter, B. Sicardy, D. Simonelli, J. Spencer, L. A. Sromovsky, C. Stoker, R. G. Strom, V. E. Suomi, S. P. Synott, R. J. Terrile, P. Thomas, W. R. Thompson, A. Verbiscer, and J. Veverka 1989. Voyager 2 at Neptune: Imaging science results. *Science* **246**, 1422-1449.

Spencer, J. R., and J. M. Moore 1992. The influence of thermal inertia on temperatures and frost stability on Triton. *Icarus* **99**, 261-272.

Spencer, J. R., M. W. Buie, and G. L. Bjoraker 1990. Solid methane on Triton and Pluto: 3- to 4-μm spectrophotometry. *Icarus* **88**, 491-496.

Standish, E. M. 1987. Jet Propulsion Laboratory Interoffice Memorandum IOM 314.6-891.

Stansberry, J. A., J. I. Lunine, W. B. Hubbard, R. V. Yelle, and D. M. Hunten 1994. Mirages and the nature of Pluto's atmosphere. *Icarus* (submitted).

Stern, S. A., D. A. Weintraub, and M. C. Festou 1993. Evidence for a low surface temperature on Pluto from millimeter-wave thermal emission measurements. *Science* **261**, 1713-1716.

Stetson, P. B. 1987. DAOPHOT: A computer program for crowded-field stellar photometry. *Publ. Astron. Soc. Pacific* **99**, 191 - 222.

Sykes, M. V., R. M. Cutri, L. A. Lebofsky, and R. P. Binzel 1987. IRAS serendipitous survey observations of Pluto and Charon. *Science* **237**, 1336-1340.

Tedesco, E. F., G. J. Veeder Jr., R. S. Dunbar, and L. A. Lebofsky 1987. IRAS constraints on the sizes of Pluto and Charon. *Nature* **327**, 127-129.

Tholen, D. J., and M. W. Buie 1990. Further analysis of the Pluto-Charon mutual event observations—1990. *Bull. Amer. Astron. Soc.* **22**, 1129.

Tokunaga, A. T., D. W. Toomey, J. Carr, D. N. B. Hall, and H. W. Epps 1990. Design for a 1-5 μm cryogenic echelle spectrograph for the NASA IRTF. *Proc. SPIE* **1235**, 131-143.

Trafton, L. 1990. A two-component volatile atmosphere for Pluto. I. The bulk hydrodynamic escape regime. *Astropys. J.* **359**, 512-523.

Trafton, L., and S. A. Stern 1983. On the global distribution of Pluto's atmosphere. *Astrophys. J.* **267**, 872-881.

Tryka, K. A. 1993. Spectroscopic determination of the phase composition and temperature of nitrogen ice on Triton. *Science* **261**, 751-754.

Tryka, K. A., R. H. Brown, D. P. Cruikshank, T. C. Owen, C. de Bergh, and T. R. Geballe 1994. Determination of the temperature of Nitrogen on Pluto from spectral measurements. *Bull. Amer. Astron. Soc.* **25**, 1129.

Walker, A. R. 1980. An occultation by Charon. *Mon. Not. Roy. Astron. Soc.* **192**, 47p-50p.

Yelle, R. V., and J. I. Lunine 1989. Evidence for a molecule heavier than methane in the atmosphere of Pluto. *Nature* **339**, 288-290.

Young, E. F. 1992. *An albedo map and frost model of Pluto*. Ph. D. Thesis, Massachusetts Institute of Technology.

Young, E. F., and R. P. Binzel 1993. Comparative mapping models of Pluto's sub-Charon hemisphere: three least models based on mutual event lightcurves. *Icarus* , 134-149.

Young, E. F., and R. P. Binzel 1994. A new determination of radii and limb parameters for Pluto and Charon from mutual event lightcurves. *Icarus* (submitted).

APPENDIX I
OCCULTATION POWER SERIES

A.1 OVERVIEW OF INTEGRATION APPROACH

To perform the integration for Chapter 3, we perform the following steps; first, factor the large planet solution out of the integral, so that the integrand = 1 to first order in the expansion parameter (e. g. δ); second, change variables so that the lead term in the exponential will be a Gaussian, and factor out of the integral any remaining terms that do not depend on the variable of integration; third, expand the integral as a power series in the expansion parameter; fourth, perform the integration.

The definite integrals to be performed are of the following forms:

$$\int_{-\infty}^{\infty} y^n \exp\left[-y^2\right] dy = \begin{cases} \Gamma\left(\frac{n+1}{2}\right), & n \text{ even} \\ 0, & n \text{ odd} \end{cases} \tag{A.1a}$$

$$\int_{-x}^{x} y^n \exp\left[-y^2\right] dy = \begin{cases} \Gamma\left(\frac{n+1}{2}\right) \operatorname{erf}(x), & n \text{ even} \\ 0, & n \text{ odd} \end{cases} \tag{A.1b}$$

A.2 INTEGRATING THE BENDING ANGLE

Using the general equation for the bending angle (3.6) and the equation for the refractivity (3.22), we take the derivative of the refractivity and express the result in terms of the energy ratios $\lambda(r)$ and $\lambda(r')$:

$$\theta(r) = -\nu(r) \int_{-\infty}^{\infty} \left(\frac{r}{r'}\right)^{b+2} \exp\left(\frac{\lambda(r') - \lambda(r)}{1+a+b}\right) \frac{\lambda(r') + b}{r} dx \tag{A.2}$$

We define a new variable of integration,

$$y = (x/r)\sqrt{1/(2\delta)} \tag{A.3}$$

with which the bending angle is

$$\theta(r) = -\nu(r)\sqrt{2\lambda(r)}\int_{-\infty}^{\infty}(1+2\delta y^2)^{-(2+b)/2}\exp\left(\frac{(1+2\delta y^2)^{-(1+a+b)/2}-1}{(1+a+b)\delta}\right) \times\left[(1+2\delta y^2)^{-(1+a+b)/2}+\delta b\right]dy \tag{A.4}$$

Expanding the integrand as a power series in δ, we obtain

$$\theta(r) = -\nu(r)\sqrt{2\lambda(r)} \times\int_{-\infty}^{\infty}e^{-y^2}\left\{1+\left[b-(3+a+2b)y^2+\left(\frac{3+a+b}{2}\right)y^4\right]\delta+O(\delta^4)\right\}dy \tag{A.5}$$

Integration is now simply a matter of collecting terms of y^{2n}, and replacing y^0 with $\Gamma(1/2)$, y^2 with $\Gamma(3/2)$, and so on. The resulting series, to fourth order, is

$$\theta(r) = -\sqrt{2\pi\lambda(r)}\nu(r)A(\delta,a,b)$$

$$\begin{aligned}A(\delta,a,b) = 1 &+\left(-\frac{3+a}{8}+\frac{3}{8}b\right)\delta+\left(-\frac{15+26a+7a^2}{128}+\frac{7+5a}{64}b+\frac{b^2}{128}\right)\delta^2\\ &+\left(-\frac{105+425a+355a^2+75a^3}{1024}+\frac{27+50a+35a^2}{1024}b+\frac{69+55a}{1024}b^2+\frac{9}{1024}b^3\right)\delta^3\\ &+\left(-\frac{4725+35196a+57134a^2+31836a^3+5509a^4}{32768}\right.\\ &\quad-\frac{1059+4907a+3857a^2+609a^3}{8192}b+\frac{2353+4326a+2233a^2}{16384}b^2\\ &\quad\left.+\frac{3764+3164a}{8192}b^3+\frac{491}{32768}b^4\right)\delta^4+\ldots\end{aligned} \tag{A.6}$$

A.3 THE DERIVATIVE OF THE BENDING ANGLE

Applying the chain rule to Eq. (3.25), the derivative of $\theta(r)$ with respect to r is

$$\frac{d\theta(r)}{dr} = -\sqrt{2\pi\lambda(r)}\nu(r)\left[\left(\frac{1}{\sqrt{\lambda(r)}}\frac{d\sqrt{\lambda(r)}}{dr} + \frac{1}{\nu(r)}\frac{d\nu(r)}{dr}\right)A(\delta,a,b) + \frac{dA(\delta,a,b)}{dr}\right] \tag{A.6}$$

We evaluate the derivatives, and factor $\lambda(r)/r$ out of the brackets. Substituting $d\lambda(r)/dr = -\lambda(r)(1+a+b)/r$, $(1/\nu)(d\nu/dr) = -(\lambda+b)/r$, and $d\delta/dr = -\delta(1+a+b)/r$, the derivative becomes

$$\frac{d\theta(r)}{dr} = \sqrt{2\pi\lambda^3(r)}\frac{\nu(r)}{r}\left[\left(\frac{(1+a+b)\delta}{2} + 1 + b\delta\right)A(\delta,a,b) - \frac{1+a+b}{2}\delta^2\frac{dA(\delta,a,b)}{dr}\right]. \tag{A.7}$$

The terms in the brackets make the series for $\theta(r)$:

$$B(\delta,a,b) = \left(1 + \frac{1+a+3b}{2}\delta\right)A(\delta,a,b) = \frac{1+a+b}{2}\delta^2\frac{dA(\delta,a,b)}{d\delta} \tag{A.8}$$

which, upon substitution of $A(\delta, \alpha, b)$ becomes

$$\begin{aligned} B(\delta,a,b) = 1 &+ \left(\frac{1+3a}{8} + \frac{15}{8}b\right)\delta + \left(\frac{9+6a+a^2}{128} + \frac{17+11a}{64}b + \frac{25b^2}{128}\right)\delta^2 \\ &+ \left(\frac{75+67a+41a^2+9a^3}{1024} - \frac{81+134a+57a^2}{1024}b + \frac{1+3a}{1024}b^2 + \frac{5}{1024}b^3\right)\delta^3 \\ &+ \left(\frac{3675+7204a+5266a^2+2564a^3+491a^4}{32768}\right. \\ &\quad - \frac{339+1347a+1297a^2409a^3}{8192}b - \frac{10555+1834a+807a^2}{16384}b^2 \\ &\quad \left. - \frac{67+49a}{8192}b^3 + \frac{59}{32768}b^4\right)\delta^4 + \ldots \end{aligned} \tag{A.7}$$

A.4 INTEGRATING THE OPTICAL DEPTH

The integral for the slant path optical depth is obtained by substituting our specification for the linear absorption coefficient, $\kappa(r)$, into the general equation for $\tau_{obs}(r)$:

$$\tau_{obs}(r) = \int_{-x_1}^{x_1} \kappa_1 \exp\left[-\frac{r' - r_1}{H_{\tau 1}(r'/r)}\right] dr' \tag{A.8}$$

Factoring out terms, this becomes

$$\tau_{obs}(r) = \kappa(r) \int_{-x_1}^{x_1} \exp\left[\frac{r_1^2}{H_{\tau 1} r}\left(\frac{r}{r'} - 1\right)\right] dx \tag{A.9}$$

The parameter for expansion is $\delta_\tau \equiv H_{\tau 1} r / r_1^2$, and the new variable of integration is $y = (x/r)\sqrt{1/(2\delta_\tau)}$ so that the integral becomes

$$\tau_{obs}(r) = \kappa(r) \frac{r}{r_1} \sqrt{2 H_{\tau 1} r} \int_{-y_1}^{y_1} \exp\left[\frac{1}{\delta_\tau}\left(\frac{1}{\sqrt{1 + 2\delta_\tau y^2}} - 1\right)\right] dy \tag{A.11}$$

We expand the integrand into the product of a Gaussian and a series in δ_τ:

$$\tau_{obs}(r) = \kappa(r) \frac{r}{r_1} \sqrt{2 H_{\tau 1} r} \int_{-y_1}^{y_1} e^{-y^2} \left[1 + \frac{3y^4}{2}\delta_\tau + \left(-\frac{5y^6}{2} + \frac{9y^8}{8}\right)\delta_\tau^2 + \ldots\right] dy \tag{A.12}$$

Performing the integration, we find

$$\tau_{obs}(r) = \kappa_1 \frac{r}{r_1} \sqrt{2\pi H_{\tau 1} r}\, \mathrm{erf}\left[\frac{r_1}{r}\left(\frac{r_1^2 - r^2}{2 H_{\tau 1} r}\right)^{1/2}\right] \exp\left[-\frac{r - r_1}{H_{\tau 1}(r/r_1)}\right] C(\delta_\tau) \tag{A.13}$$

$$C(\delta_\tau) = 1 + \frac{9}{8}\delta_\tau + \frac{345}{128}\delta_\tau^2 + \frac{9555}{1024}\delta_\tau^3 + \frac{1371195}{32768}\delta_\tau^4 + \ldots \tag{A.14}$$

APPENDIX II

REDUCTION SOFTWARE

AII.1. Languages used

language	
Mma	Mathematica, Wolfram Research Inc.
IRAF	Image Reduction and Analysis Facility, National Optical Astronomical Observatories
csh	UNIX "C shell" command language interpreter
C	C programming language
F77	Fortran 77 programming language

AII.2. Reduction Steps and Software

task or goal	function or program	lang-uage	location
chapter 2			
preprocess	imarith, imsurfit	IRAF	$iraf/pkg/images/
list of approximate centers	phot	IRAF	$iraf/noao/digiphot/daophot
add Charon to list of centers	adjmag	csh	$imaging/decmipsbin/adjmag
make the PSF from field stars	psf	IRAF	$iraf/noao/digiphot/daophot
fit PSFs to find centers	group, nstar	IRAF	$iraf/noao/digiphot/daophot
put the centers into FITS tables	nstToSl	Mma	$imaging/macros/mk_xylist.m
register the exposures	reg	C	$software/src/reg
generate the Pluto ephemeris	simple_eph	C	$software/src/simple_eph
turn α, δ into ξ, η	prRDtoXE	Mma	$imaging/macros/plateReduction1.5.m
model ξ and η from parameters	func	Mma	$mass ratio:Pluto Fits:pluto.astrom8.1.m
chapter 3			
model occultation lightcurve	lightCurve7	Mma	$math_packages/leastSquares2.0.18.m
least-squares fitting engine	iterate	Mma	$math_packages/leastSquares2.0.18.m
convert parameter sets	calcRelatedPandE	Mma	$occl:Pluto ms4.m P2.9.2y 90-12

AII.2. Reduction Steps and Software, continued.

task or goal	function or program	lang-uage	location
chapter 4			
preprocess	imarith, imedit	IRAF	$iraf/pkg/images/
extract the spectra	apall	IRAF	$iraf/noao/twodspec/apextract
modify Pluto's traces	mkap25,mkap26	csh	$cshell/bin
find the dispersion correction	reidentify	IRAF	$iraf/noao/onedspec
dispersion-correct the spectra	refspec, dispcor	IRAF	$iraf/noao/onedspec
write the spectra	wspec	IRAF	$cshell/iraf/scripts/wspec.cl
a nicer format for the spectra	wspec2txt	csh	$cshell/bin/wspec2txt
normalize and find S/N	specNorm	Mma	$cshell/mma_macros/macros3.m
weighted mean of spectra	specWmean	Mma	$cshell/mma_macros/macros3.m
telluric absorption	atran	f77	$software/src/atran (from Steve Lord)
Pluto's methane absorption	methspec	C	$cshell/bin/src
model spectrum	plufunc	Mma	$cshell/mma_macros/notebook5b.m

AII.3. Location Prefixes

prefix	computer	location
$math_packages	astron.mit.edu (DEC MIPS)	/pscf/jle-grp/software/lib/math_packages/
$software	astron.mit.edu (DEC MIPS)	/pscf/jle-grp/software/
$mass ratio	lowell.mit.edu (Mac. Quadra 950)	Projects HD #1:Pluto Charon:mass ratio 92-02:
$imaging	astron.mit.edu (DEC MIPS)	/pscf/jle-grp/projects/pc_imaging_92/
$cshell	astron.mit.edu (DEC MIPS)	/pscf/jle-grp/projects/pluto_cshell_92-06/
$iraf	astron.mit.edu (DEC MIPS)	/pscf/tools/iraf/iraf2.10/
$occl	lowell.mit.edu (Mac. Quadra 950)	Projects HD #1:Pluto Charon:Pluto 90-2 lay jle: